POLITECNICO
MILANO 1863

SCUOLA DI INGEGNERIA INDUSTRIALE
E DELL'INFORMAZIONE

Parametric design for Earth to Sun-Earth L2 halo transfers in the circular restricted three body problem

Tesi di Laurea Magistrale in

Space Engineering - Ingegneria Industriale

Author: **Marco Lo Iacono**

Student ID: 970229

Advisor: Prof. Camilla Colombo

Co-advisors: Elisa Maria Alessi

Academic Year: 2021-22

Marco Lo Iacono, “Parametric design for Earth to Sun-Earth L2 halo transfers in the circular restricted three body problem”. 2023, Politecnico di Milano, Master Thesis in Space Engineering, Supervisor: Camilla Colombo, Co-advisor: Elisa Maria Alessi.

Abstract

In the Sun-Earth system, by exploiting the hyperbolic invariant manifolds associated with periodic orbits stemming from L2 (SEL2 in the following), halo orbits are reachable at low cost from LEO and GTO orbits.To identify the most favorable SEL2 orbits for scientific missions, this work maps SEL2 halo orbits considering different perspectives. On the transfer side: which halos can be reached; in what time; at what cost; along what path and where insertions take place; with what performances and risks. On the operational halo side: how stable; what space environment and Earth visibility; what disposal requirements. Each analysis is conducted parametrically, giving an overall view on the available options and trade-offs between performances. Simultaneously, the investigation is applied to a specific mission, current under study, the Radiation Environment Monitor for Energetic Cosmic rays (REMEC) mission.

Keywords: Mission Design, CR3BP, hyperbolic manifolds, SEL2 halo, REMEC mission.

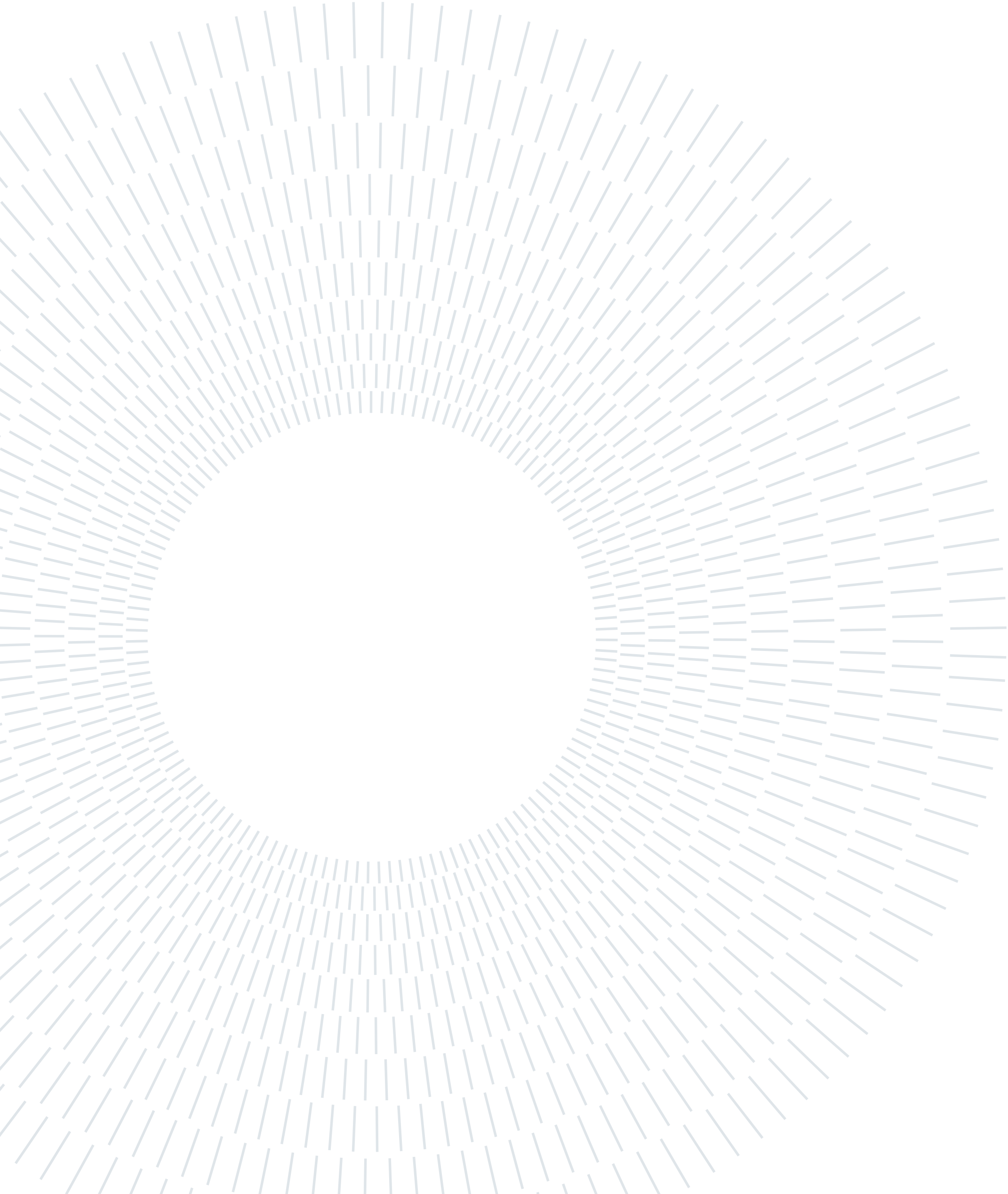

Abstract in lingua italiana

Nel sistema Sole-Terra, sfruttando i collettori iperbolici invarianti associati alle orbite periodiche derivanti da L2 (SEL2 nel seguito), le orbite halo sono raggiungibili a basso costo dalle orbite LEO e GTO. Per identificare le orbite SEL2 più favorevoli per le missioni scientifiche, questo lavoro mappa le orbite halo SEL2 considerando diverse prospettive. Dal punto di vista del trasferimento: quali orbite halo possono essere raggiunte; in quale tempo; a quale costo; lungo quale percorso e dove avvengono gli inserimenti; con quali prestazioni e rischi. Per quanto riguarda le halo operative: la stabilità dell'orbita; il suo ambiente spaziale e la visibilità della Terra; come condiziona la manovra di fine vita. Ogni analisi è condotta in modo parametrico, fornendo una visione complessiva delle opzioni disponibili e dei trade-offs tra le prestazioni. Contemporaneamente, l'indagine viene applicata a una specifica missione, attualmente in fase di studio, la missione Radiation Environment Monitor for Energetic Cosmic rays (REMEC).

Parole chiave: Mission Design, CR3BP, manifolds iperbolici, halo SEL2, missione REMEC.

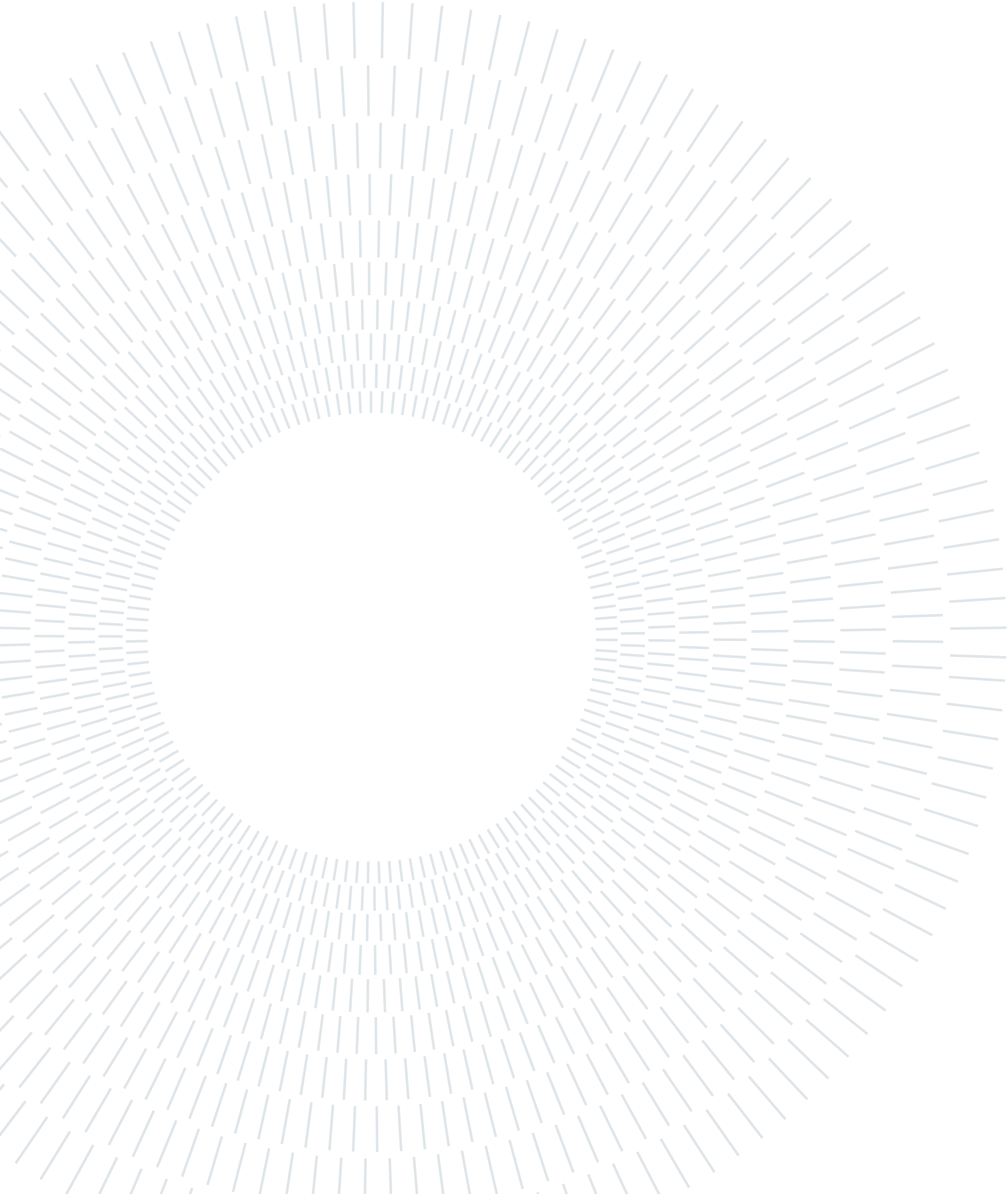

Contents

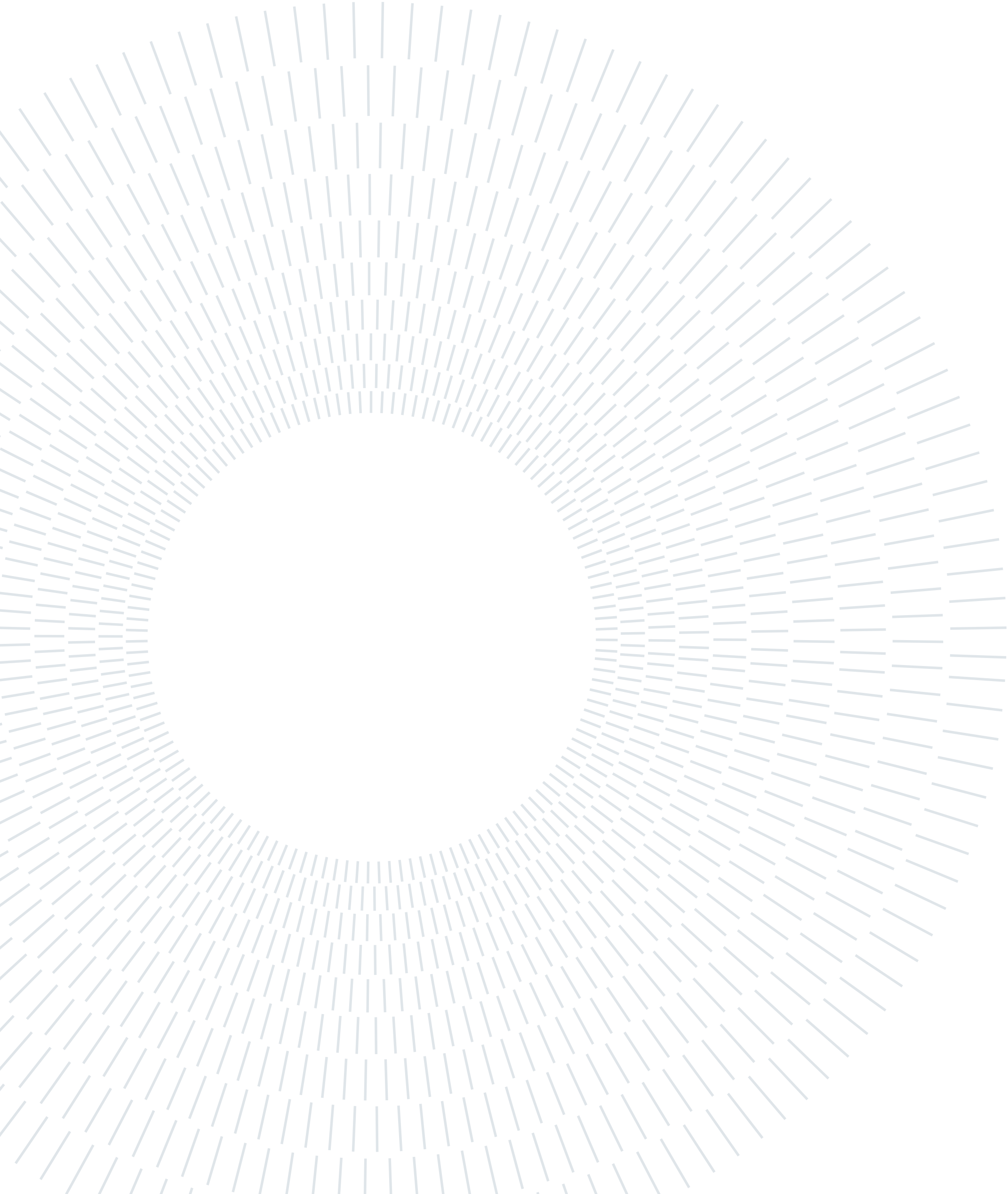

1 | Introduction

This thesis belongs to the field of Astrodynamics, and is aimed at Trajectory Design. It operates within the Circular Restricted Three Body Problem. Like many works of this kind, the main intent is to exploit the Space Tube Dynamics. Likewise, the numerical methods described, implemented and used are already present and validated in literature e.g., continuous differential method, targeting and multi shooting transcription. Within this framework, each chapter offers a brief introduction to the research question that drives it and to the instruments put in place to investigate it, as well as a brief conceptual summary and a list of the main references.

1.1. Background

Astrodynamics deals with the design and control of spacecraft trajectories. In principle, the satellite is affected by many gravitational and non-gravitational effects. The simplest approach is to consider the spacecraft under the influence of one main attractor alone: the well-known Kepler model or Restricted 2-Body Problem (R2BP). Each R2BP ends and begins at the boundaries of the main attractor sphere of influence. In mission design practice, the R2BP finds application through the patched-conic method. Examples of well-known missions that have made use of it are Voyager and Apollo.

By including a second attractor in the model in addition to the main one, it is possible to design missions that target the neglected region of R2BP approach: the boundary of the sphere of influence of the secondary, where the action of two attractors is comparable. Szebehely [1967] is a milestone work, the paper explores the limits of the patch conic method and demonstrates the existence of lower cost trajectories in the Restricted 3-Body Problem (R3BP).

In the Sun Earth Circular Restricted 3-Body Problem (CR3BP), stable manifolds allows low-demanding trajectory from Earth to L2 halo orbits. Halos are periodic orbits characterized by a good and stable visibility of Earth, as well as a stable and uninterrupted observation of deep space.

Richardson [1979] provided an semi-analytical approach of halo orbits. However, due to the high sensitivity of the CR3BP the initial state obtained might be not accurate enough to get a periodic solution.

The semi-analytical solution is a good reference first guess to start a numerical approach. Koon et al. [2011] provides a practical guide to mission design algorithms: the differential correction method, targeting and multishooting. For further clarification, reference is also made to Betts [1998], Pavlak [2010], Mingotti et al. [2011] and Topputo [2013].

1.2. Δv Literature review

Table **[3.6]** summarises a literature review on the transfer from a parking orbit at the Earth and a libration point orbit at L2 in the Sun-Earth system.

- Barden [1994] assumes a dedicated launch to inject into the manifold of the given halo orbit, so the works compute only the cost at the halo Orbit Injection if any. The Δv_{HOI} is zero when the s/c is already in the manifold. He highlights the relationship between the closest approach of a manifold to the Earth and the amplitude of the corresponding halo orbit. The case of multiple passages is also considered, as well as the trade-off between transfer time and cost.

- Rausch [2005] adds to Barden [1994] the computation of Δv_{TTI} assuming a LEO parking orbit of 200 km altitude. He also gives evidence that using the ephemeris model the cost is about the same as the one estimated by CR3BP.
- Bernelli et al. [2004] assume that the s/c is in a circular parking orbit and halo's amplitude is between 100,000 and 330,000 km. In the estimates in Tab.**[3.6]** the cost to reach the circular orbit is not accounted. In the paper the Δv_{HOI} is computed also if the transfer trajectory is a stable manifold to correct approximations at the halo insertion point.

1.3. Missions using manifolds

In this section, it is intended to highlight the opportunities of the CR3BP i.e., the missions that might be designed within the model's assumptions. For this reason a description of present and future missions is given.

Space mission to Lagrangian points started in 1978 with ISEE-3 (NASA) at SEL1-halo. The International Sun-Earth Explorer was dedicated to solar wind and cosmic rays and it was operational until 1997. In 2001 the Genesis (NASA) exploited the manifold dynamics to return the collected solar-wind samples back to Earth. The same year the MAP (NASA) was the first mission in SEL2. Its objective was to study the background cosmic radiation.

ESA-NASA have placed SOHO solar observatory at SEL1 in 1996. The SOHO introduced a innovation for the station-keeping control method: instead to target a predetermined analytical path, the stable perturbed direction was exploited to meet the operation constraints within a quasi-periodic orbit. The SOHO mission has been extended until the

Table 1.1: from LEO to SEL2-Halo

A_z [km]	Δv_{TTI} [km/s]	h [km]	i [deg]	ΔT [days]	Δv_{HOI} [m/s]	source
100,000	2.696	4991	6.7	126.6	3.4	Bernelli et al. [2004]
130,000	2.598	4970	8.2	126.7	3.5	Bernelli et al. [2004]
150,000	2.549	4938	9.4	126.8	3.5	Bernelli et al. [2004]
170,000	2.517	4880	10.5	127.0	3.6	Bernelli et al. [2004]
190,000	2.492	4838	11.6	127.2	3.6	Bernelli et al. [2004]
210,000	2.474	4866	12.7	127.4	3.7	Bernelli et al. [2004]
230,000	2.474	4983	13.6	127.7	3.7	Bernelli et al. [2004]
250,000	2.521	4881	14.5	128.0	3.7	Bernelli et al. [2004]
270,000	2.596	4825	15.4	128.3	3.8	Bernelli et al. [2004]
290,000	3.997	4825	16.3	128.6	3.8	Bernelli et al. [2004]
310,000	2.883	4901	17.1	129.0	3.9	Bernelli et al. [2004]
330,000	1.334	GEO	2.3	123.3	3.4	Bernelli et al. [2004]
120,000	-	185	-	208.06	20.34	Barden [1994]
120,000[1]	-	185	-	347.96	0	Barden [1994]
440,000	-	185	-	117.44	8.62	Barden [1994]
120,000	-	4960	-	-	0	Barden [1994]
240,000	-	2100	-	-	0	Barden [1994]
440,000	-	232	-	219.8	0	Barden [1994]
440,000	-	210	-	219.8	0	Barden [1994]
120,000	3.1925	200	-	209.3	20.66	Rausch [2005]
440,000	3.1930	200	-	215.5	0	Rausch [2005]
440,000	3.1934	200	-	213.8	0	Rausch [2005]
120,000[2]	3.1924	200	-	209.3	18.66	Rausch [2005]
440,000[2]	3.1944	200	-	215.5	0	Rausch [2005]
440,000[2]	3.1944	200	-	213.8	0	Rausch [2005]

[1] Multiple passages

[2] ER3BP

end of 2025.

Between the 2001 and the 2015 NASA and ESA have planned fifteen mission in SEL1 or SEL2. Actually there are four active probes in SEL1 (SOHO, ACE, WIND, DSCVR) and three in SEL2 (Gaia, Spektr-RG, JWST). Description of their mission design is provided by Canalias et al. [2004].

Table **[1.2]** shows some of the planned future missions over the five-year period 2023-2028. Details are provided in `https://nssdc.gsfc.nasa.gov/nmc/SpacecraftQuery.jsp`, `https://www.eoportal.org/` and `https://www.nanosats.eu/`.

The following focuses only on missions in SEL2:

WFIRST (Farres et al. [2018]): L-class mission designed to answer questions about dark energy and infrared astrophysics. It is planning to fly on a high unstable SEL2-halo orbit, where station-keeping maneuvers are required to maintain the nominal orbit. These maneuvers are done every 21 days in the direction that cancels out the drift along the unstable manifold (Floquet Mode). Additionally, WFIRST will need to perform routine manoeuvres to unload stored momentum in the reaction wheels. The paper carry out a simulation around a halo A_z 120,000 km taking account a SRP $q_{srp} = 10^{-5}$. The total Δv for 2 year simulation is of 10.42 cm/s when no attitude manoeuvres are considered and of 11.57 cm/s otherwise.

PLATO: M-class science mission within ESA's Cosmic Vision Program, its primary aim is to investigate terrestrial exoplanets orbiting in the habitable zone around solar-type stars. The second scientific goal is the probing of stellar structure and evolution by asteroseismology. The s/c has launch mass of 2165 kg and size 3.4 m × 3.3 m × 3.8 m. A monopropellant propulsion system is used to reach and maintain the operative halo orbit around Sun-Earth L2. The s/c will spend two days

Table 1.2: Future Planned Missions

Mission	**Year**	**Agency**	**Launcher/Contractor**	**Mass**	**Propulsion**	**Target**	**System**
Chandrayann-3	2023	ISRO/JAXA	H3	-	-	Landing	Moon
Euclid	2023	ESA	Ariane62	2160	cold gas	L2	SE
PRIME-1	2023	NASA CLPS	Falcon9/Intuitive	2000	-	Landing	Moon
SLIM	2023	JAXA	H-IIA 202	590	hydrazine + MON-3	Landing	Moon
TO 19C	2023	NASA CLPS	Master	2675	-	Landing	Moon
TO 19D	2024	NASA CLPS	Falcon9/Firefly	155 (P/L)	-	Landing	Moon
VIPER	2024	NASA CLPS	Falcon Heavy/SpaceX	430 (dry)	-	Rovering	Moon
TO CP-11	2024	NASA CLPS	Falcon9/Intuitive	130 (P/L)	-	Landing	Moon
Chang'e 6	2024	CNSA	Chang Zeng 5	8200	hypergolic pr.	Sample Return	Moon
Chang'e 7	2024	CNSA	Chang Zeng 5	8200	hypergolic pr.	Rovering	Moon
HERA	2024	ESA	Ariane6	1128	MMH/MON Helium	Asteroid	Deep Space
M-ARGO	2024	ESA	-	-	-	Asteroid	Deep Space
DESTINY+	2024	JAXA/ISAS	EpsilonS	480	hydrazine, xenon	Asteroid	Deep Space
Artemis II	2024	NASA	SLC Block1	$>$ 33 ton.	hypergolic pr.	Orbiting	Moon
Lunar Trailblazer	2025	NASA	Falcon9/SpaceX	200	hydrazine	Orbiting	Moon
Artemis III	2024	NASA	SLC Block1	$>$ 33 ton.	hypergolic pr.	Landing	Moon
WFIRST	2025	NASA	Falcon Heavy/SpaceX	4166	-	L2	SE
PLATO	2026	ESA	Soyuz ST	2100	monopropelant	L2	SE
Chang'e 8	2026	CNSA	-	-	-	-	Moon
Artemis IV	2027	NASA	SLC Block1	$>$ 33 ton.	hypergolic pr.	Gateway	Moon
Artemis V	2028	NASA	SLC Block1	$>$ 33 ton.	hypergolic pr.	Gateway	Moon
LiteBIRD	2028	JAXA/NASA	H3	450 (dry)	-	L2	SE
ARIEL	2029	ESA	Ariane6	1300	hydrazine	L2	SE

in LEO parking orbit for early operation phase until 2^{nd} Fregat burn. The transfer time to approach SEL2 is 30 days, with three planned Transfer Corrective Manoeuvres (TCM). Finally, another 30 days are needed to reach operational conditions (commissioning).

LiteBIRD (Hazumi et al. [2020]): L-class mission to carry out a three years full-sky surveys. JAXA's H3 rocket is used to launch and insert an orbit around the Sun-Earth Lagrangian point L2. A Lissajous orbit is chosen for the better thermal conditions compared to halo orbits.

ARIEL (Puig et al. [2018]): M-class mission, the launch is anticipated to 2028 together with the Comet Interceptor mission on ESA's Ariane 6. Ariel will operate from SEL2 for an initial four year mission. Eclipse-free (Earth and Moon) orbit, Sun-s/c-Earth angle at most 45 [deg], the halo is designed to allow a stable thermal and mechanical environment, such that ARIEL s/c will be able to carry out long term observations of exoplanets. The mission design must be compatible with an Ariane 6 launch from Kourou in 2026. The Δv_{TTI} is provided by launcher 2^{nd} burn service, the total requirement for the on-board propulsion system is 125.95 m/s thus detailed: 47.32 m/s TTC; station-keeping 22.18 m/s; decommissioning 10 m/s; Soyuz and A5 compatibility 23.44 m/s; margin 10 m/s; contingency 15 m/s.

Also missions targeting the Moon can exploit the manifold dynamics e.g., Artemis program and Lunar Gateway project are L-class NASA missions operating in the Earth-Moon system performing halo or DRO.

Similarly, deep-space missions to asteroids make use of manifolds for both their transfer and subsequent observation (Sanchez and Yárnoz [2016]). In fact, asteroids offer too small or irregular a gravitational field to guarantee a stable orbit in R2BP (Herrera-Sucarrat et al. [2014]).

Recently, the scientific community has been showing increasing interest in placing a space observatory at Lagrangian point L1 of Sun-Jupiter system (Hsu et al. [2021]).

1.4. Aim and contribution of the thesis

This study offers a parametric analysis to support the preliminary design of a SEL2-halo space mission. The investigation is conducted in the CR3BP, which offers a conservative approach and timeline independence.

Although in the literature are already planned missions to SEL2 in the Sun-Earth system, there lack a parametric analysis based on multiple Libration orbit amplitude which would offer a tool for fast mission analysis considerations.

The thesis produces a parametric study to design both the operational orbit and the transfer trajectory in a large family of possible orbits considering delta-v cost, coverage, visibility constraints.

1.5. Thesis structure

The first chapter introduces a reader already accustomed to the Keplerian model to the CR3BP. Between the two models there is not a qualitative leap but a paradigm shift. One has to adapt one's gaze, as it were, to new and unexpected forms. Together with the description of the theoretical model, the concepts supporting the actual research activity are introduced. Many references are provided so that the reader can find his or her way through the vast literature, so depending on the particular subject discussed, both sources and insights are suggested. In addition to theory, results from the literature are collected and reproduced. The examples come from the Earth-Moon CR3BP, of which the literature is rich. The algorithms are tested on Earth-Moon because the mass parameter is higher.

In concrete terms, firstly there is a historical slice and a glance at advantages and disadvantages between R2BP and Multibody Dynamics in Mission Design. Then, the physical model, the reference frame and the equations of motion are introduced (Newtonian, Lagrangian, Hamiltonian). Then, by a symplectic coordinate change the invariant structures of the CR3BP in equilibrium neighboured are obtained e.g., Space Tubes and halo orbits. Finally, the CR3BP invariant structures are derived numerically by means of a differential method.

The research activity is undertaken in the second part of this thesis. The goal is to provide a handbook for profiling a mission to SEL2 halo. Two ways are possible:

- The idea is that given a commercial, hence non-dedicated launch, the pericentre of the parking orbit in ecliptic coordinates is constrained. Starting from this data, it is intended to already have all the information needed to determine which halos are reachable, along which trajectories, with which performances. The driver of a baseline budget is the manifold insertion cost. Several transferring strategy to SEL2 halo are proposed. A parametric approach based on the use of the Poincaré section is explored. The description plays with different parking orbits (LEO, GTO) and insertion design to obtain a budget baseline versus altitude.
- Having a launch that leads to a dedicated GTO, selected according to the nominal halo orbit, that satisfies well-defined payload requirements. In such a case, the analysis begins with a trade-off analysis between halo performance in terms of reliability and operability. Once a number of profiles have been defined and their trade-offs established, one has a good guess for the optimisation algorithms.

The research activity is mainly dedicated to the transfer from Earth, but an end-of-life phase strategy is also profiled, which is the second contribution in terms of budget.

2 | Methods for mission design in the CRTBP and design of libration point orbits

2.1. Introduction

To interpret a phenomenon, it is necessary to model it. With a selected set of simplifications, the model translates the phenomenon into an accessible analytical form. However, if the simplifications made are excessive, then the solutions proposed by the model are either trivial or far away from reality. On the other hand, if a model lacks the appropriate simplifications, it adheres more closely to the phenomenon but leads to non-analytical mathematical formulations. In general, a compromise between the model's adherence to the phenomenon and its interpretive capacity is necessary.

This thesis belongs to the field of Astrodynamics, and is aimed at Trajectory Design. It is the responsibility of the designer to select the model he intends to use. To do so, he must be aware of the model's assumptions and ensures that it is used within its boundaries. Usually, the different phases of design involve increasingly refined models. The choice of the model used in each design phase has a cascading effect on all the next phases.

In this chapter, the theoretical model of the CR3BP is summarised and the software for the model's applications are developed in parallel. In fact, the author does not have any pre-existing platforms and implements them himself. The tools obtained are validated by reproducing results found in the literature. The algorithms are tested on Earth-Moon because the mass parameter is higher. All MATLAB illustrations in the chapter are outputs of the validated softwares.

Main References: Introduction texts to Astrodynamics are Curtis [2005] and Bate et al. [2020]. Reference work for Restricted 3-Body Problem (R3BP) is Szebehely [1967]. Musielak and Quarles [2014] for a historical sketch of 3BP from its origins up to date. Koon et al. [2011] provides very helpful guideline to kick-start the implementation, while for in-depth study the 4-volume work Gómez [2001] is a milestone. Doedel et al. [2007] offers a comprehensive review of the CR3BP orbit families. Further references are given inside.

Chapter Outline: This chapter does not offer contributions to the existing literature, but can provide clarification for those wishing to approach the CR3BP. This model is the framework within which the present work operates and for this reason is explained in detail. First of all, opportunities and limitations of the CR3BP and the Keplerian model are presented in **[2.2]**. In addition, the vocabulary and notions underlying the model are quickly introduced. This is followed by the derivation of the natural dynamics: appropriate reference systems are selected **[2.3.1]**, with respect to which the Equations of Motion (EoM) in Euler-Lagrange form **[2.3.3]** and Hamilton form **[2.3.6]** are obtained. The analysis of the EoMs provide Lagrangian equilibrium points **[2.3.4]**, Jacobi integral and Hill's regions **[2.3.5]**. Then, the analysis is detailed in the neighbourhoods of the equilibrium points: the EoMs are linearised **[2.4.2]** to obtain a topology of orbits **[2.4.3]**, **[2.4.4]**, **[2.4.5]**. The last sections cast the basis for the mission design in the CR3BP: the State Transition Matrix **[2.5]** and the Poincaré map **[2.6]** are presented; an implementation of the differential correction method is proposed for the design of Lyapunov and halo orbits **[2.7]**; a numerical approach to compute hyperbolic manifolds is described **[2.8]**.

2.2. Restricted Three Body Problem

Astrodynamics deals with the design and control of spacecraft trajectories. In principle, the satellite is affected by many gravitational and non-gravitational effects. The simplest approach is to consider the spacecraft under the influence of one main attractor alone: the well-known Kepler model or Restricted 2-Body Problem (R2BP). In mission design practice, the R2BP finds application through the patched-conic method. Examples of well-known missions that have made use of it are Voyager and Apollo. A trajectory that move from Earth to Mars can be broken down into three R2BPs: Earth-spacecraft; Sun-spacecraft; Mars-spacecraft. Each R2BP ends and begins at the boundaries of his own sphere of influence.

The limits of the patched-conic method follows from the assumption that the action of all attractors other than the main one can be considered a perturbation. This is acceptable when the spacecraft is moving at great speed and therefore the time span for which the assumption is not fulfilled is short. In conclusion, the application of the patched-conic method limits our choices to only high-speed trajectories.

What has just been said does not imply that designing a mission with the patched-conic method is unsuitable. In certain contexts it is a good first approximation for drawing a trajectory that will later be 'refined' using more complex models.

By including a second attractor in the model in addition to the main one (R3BP), it is possible to design missions that target the neglected region of R2BP approach: the boundary of the sphere of influence of the secondary, where the action of two attractors is comparable. Furthermore, Conley [1968] demonstrates the existence of low demanding transfer trajectories targeting those regions.

The first formulation of the 3BP is due to Newton [1687]. It was applied in restricted form (R3BP) to describe the motion of comets under the influence of two attractors (the Sun and a giant planet). The R3BP can approximate the planet orbit in circular (CR3BP) or elliptical (ER3BP). With reference to CR3BP: Euler [1767] proposed the adoption of a synodic reference system; Lagrange [1772] calculated the equilibrium libration points completing Euler's work; Jacobi [1843] proved integrability; Hill [1877] determined the zero velocity curve; ending the XIX century, Poincaré [1892, 1893, 1899] proposed a method to search periodic solutions. All these achievements paved the way to modern Multibody Dynamics.

It ought to be pointed out that in the CR3BP the Keplerian elements do not exist, and the Jacobi's constant is the only first integral. However, the loss of orbital elements is compensated by the existence of Space Manifolds (SMs), invariant structures of CR3BP associated with periodic orbits around the libration points. SMs can be exploited in the CR3BP framework to design trajectories for space missions.

SMs are directed to or originate from orbits around libration points[1]. They are stable if they go towards the libration orbits, otherwise unstable. The SMs are low demanding trajectories. Speed decrease drives down the propellant budget, resulting in a larger number of feasible missions and in an increase of design flexibility. However, the velocity decrease might bring a significant higher time of flight.

Summarising, here are the main applications for which SMs are exploitable:

- They lead to orbits around libration points, which can be used as sites for space

---

[1] This applies to the unstable libration points L1, L2 and L3, not to the stable equilibrium points L4 and L5.

research, telecommunications and colonisation. The same dynamics can be exploited for station-keeping.

- They also offer an interesting perspective for decommissioning operations. Indeed, they allow space graveyards orbits to be reached at limited cost.
- First reference is clearly the non-human interplanetary missions. But even in the absence of a crew, the approach demands to balance mission cost and time. Indeed, engineering constraints such as fuel and energy storage limit mission duration.

The implementation requires prior knowledge of the CR3BP theory, which is the topic covered by the next sections of this chapter.

2.3. CR3BP Natural Dynamics

2.3.1. Reference Systems

Based on the CR3BP model, the system is composed by two massive bodies and one body with negligible mass (the spacecraft in our case). From here on, the massive bodies are referred as primaries e.g., in a Sun and Earth+Moon system, the Sun is the main primary, Earth+Moon the minor primary. Both primaries are considered to orbit in circular motion around the common barycentre.

It is common to normalise the model by means of the length factor l_*, the mass factor m_*, and the time factor τ_*: l_* is the distance between the two massive bodies, m_* is the sum of their masses, τ_* is equal to the ratio $\sqrt{l_*^3/(Gm_*)}$. It is possible to move from the normalised to the dimensional model by means of relationships:

$$\begin{aligned} &\mathbf{r_d} = l_* \, \mathbf{r} \\ &\dot{\mathbf{r}}_\mathbf{d} = v_* \, \dot{\mathbf{r}} \qquad \text{where } v_* = \frac{l_*}{\tau_*} \\ &t_d = \tau_* \, t \end{aligned} \tag{2.1}$$

Let G, ω and T be the Newton's gravitational constant, the mean motion and the period of the primaries, respectively, then their normalised counterparts G_*, n and T_* are:

$$\begin{aligned} &G_* = 1 \, \frac{[ndL]^3}{[ndT]^2 \, [ndM]} \\ &n = 1 \, [ndT]^{-1} \\ &T_* = 2\pi \, [ndT] \end{aligned}$$

Note further that:

$$\begin{aligned} \tau_* &= \frac{T}{2\pi} = \frac{1}{\omega} \\ t &= \frac{t_d}{\tau_*} = \omega \, t_d \end{aligned}$$

It is also convenient to introduce two gravitational parameters[2] μ and μ_1:

$$\mu = G_* \, \frac{m_2}{m_*} \qquad m_2 : \text{small primary mass} \tag{2.2}$$

$$\mu_1 = G_* \, \frac{m_1}{m_*} = 1 - \mu \qquad m_1 : \text{main primary mass} \tag{2.3}$$

The sidereal reference system is an inertial reference system centred at the barycenter of the system, with the X-axis directed towards the vernal point, the Z-axis perpendicular to the orbital plane of the primaries, and the Y-axis established according to the right hand rule.

The synodic reference system is a non-inertial reference system, centred at the

---

[2] Known also as mass parameters since G_* is unitary.

barycenter of the primaries, with the x-axis directed towards the minor primary, the z-axis perpendicular to the orbital plane of the primaries and rotating with a constant angular velocity equal to the mean motion of the primaries[3] n. The y-axis is determined according to the right hand rule.

Let's be $\mathbf{x} = (x, y, z)^T$ the coordinates of the spacecraft in the synodic reference system and $\mathbf{X} = (X, Y, Z)^T$ the same coordinates in the normalized sidereal reference system. Assume the corresponding velocities $\dot{\mathbf{x}} = (\dot{x}, \dot{y}, \dot{z})^T$ and $\dot{\mathbf{X}} = (\dot{X}, \dot{Y}, \dot{Z})^T$. To move from the synodic to the sidereal reference system is used the rotation matrix $\mathbf{A_3}$, namely:

$$\begin{aligned} &\mathbf{X} = \mathbf{A_3}\mathbf{x} \qquad \text{where } \mathbf{A_3} = \begin{bmatrix} \cos t & -\sin t & 0 \\ \sin t & \cos t & 0 \\ 0 & 0 & 1 \end{bmatrix} \\ &\dot{\mathbf{X}} = \dot{\mathbf{A}}_\mathbf{3}\mathbf{x} + \mathbf{A_3}\dot{\mathbf{x}} = \mathbf{A_3} \begin{bmatrix} -n\,y + \dot{x} \\ n\,x + \dot{y} \\ \dot{z} \end{bmatrix} \end{aligned} \tag{2.4}$$

and vice-versa:

$$\begin{aligned} &\mathbf{x} = \mathbf{A_3}^{-1}\mathbf{X} \qquad \text{where } \mathbf{A_3}^{-1} = \begin{bmatrix} \cos t & \sin t & 0 \\ -\sin t & \cos t & 0 \\ 0 & 0 & 1 \end{bmatrix} \\ &\dot{\mathbf{x}} = \mathbf{A_3}^{-1} \begin{bmatrix} n\,Y + \dot{X} \\ -n\,X + \dot{Y} \\ \dot{Z} \end{bmatrix} \end{aligned} \tag{2.5}$$

Once in the synodic reference system it is possible with a rigid translation to move the origin of our reference system so to observe the motion of the spacecraft from the main

---

[3] In normalised units, n and G_* are equal to 1, so they are omitted.

primary, the minor primary, or the Lagrangian points.

2.3.2. Newtonian EoM

Given that the two primaries move on circular orbit their positions $\mathbf{R_1}, \mathbf{R_2}$ and velocities $\dot{\mathbf{R}}_\mathbf{1}, \dot{\mathbf{R}}_\mathbf{2}$ respect to the normalized sidereal reference system are:

$$\begin{aligned}
\mathbf{R_1} &= (-\mu \cos t, -\mu \sin t, 0) \\
\mathbf{R_2} &= (\mu_1 \cos t, \mu_1 \sin t, 0) \\
\dot{\mathbf{R}}_\mathbf{1} &= (\mu \sin t, -\mu \cos t, 0) \\
\dot{\mathbf{R}}_\mathbf{2} &= (-\mu_1 \sin t, \mu_1 \cos t, 0)
\end{aligned} \tag{2.6}$$

The sidereal reference system is inertial, so a Newtonian approach is applicable. The normalised gravitational forces acting on the spacecraft give the relationship:

$$\ddot{\mathbf{X}} = -\frac{1-\mu}{R_{13}^3}\mathbf{R_{13}} - \frac{\mu}{R_{23}^3}\mathbf{R_{23}} \tag{2.7}$$

where:

$$\mathbf{R_{13}} = (X + \mu \cos t; Y + \mu \sin t; Z)$$

$$\mathbf{R_{23}} = (X - \mu_1 \cos t; Y - \mu_1 \sin t; Z)$$

The same equations can be written also as a function of the gravitational potential, in this way:

$$\begin{cases} \ddot{X} = -U_{/X} \\ \ddot{Y} = -U_{/Y} \\ \ddot{Z} = -U_{/Z} \end{cases} \qquad U = -\frac{1-\mu}{R_{13}} - \frac{\mu}{R_{23}} \tag{2.8}$$

These equations are explicitly time dependent since the coordinates of the primaries change with time, $R_{i3} = f_{i3}(\mathbf{X}, t)$.

2.3.3. Euler-Lagrange EoM

The explicit time dependency vanishes switching to the synodic reference system: now the primaries appears fixed as the z-axis rotates with main motion n. The positions of the primaries respect to the synodic reference system are:

$$\begin{aligned} \mathbf{r_1} &= (-\mu, 0, 0) \\ \mathbf{r_2} &= (1-\mu, 0, 0) \end{aligned} \tag{2.9}$$

However, since the reference system is rotating for the satellite's motion the following applies:

$$\begin{aligned} \mathbf{r_3} &= (x, y, z) \\ \dot{\mathbf{r}}_\mathbf{3} &= \frac{d\mathbf{r_3}}{d\tau} + n\hat{k} \times \mathbf{r_3} = (\dot{x} - y, \dot{y} + x, \dot{z}) \\ \ddot{\mathbf{r}}_\mathbf{3} &= \frac{d\dot{\mathbf{r}}_\mathbf{3}}{d\tau} + n\hat{k} \times \dot{\mathbf{r}}_\mathbf{3} = (\ddot{x} - 2\dot{y} - x, \ddot{y} + 2\dot{x} - y, \ddot{z}) \end{aligned} \tag{2.10}$$

In $\ddot{\mathbf{r}}_\mathbf{3}$ they are recognisable the normalized contributions of a Coriolis force $(-2\dot{y}, 2\dot{x}, 0)$ and a centrifugal pseudo-potential. Let's define the augmented normalized potential U^*:

$$U^* = -\frac{1-\mu}{r_{13}} - \frac{\mu}{r_{23}} - \frac{1}{2}(x^2 + y^2) \tag{2.11}$$

where:

$$r_{13} = \sqrt{(x+\mu)^2 + y^2 + z^2}$$

$$r_{23} = \sqrt{(x-1+\mu)^2 + y^2 + z^2}$$

It is first necessary compute the Lagrangian $\mathcal{L}$ into synodic reference system from the inertial normalized one:

$$\begin{aligned}
\mathcal{L} &= K - U \\
&= \frac{1}{2}(\dot{X}^2 + \dot{Y}^2 + \dot{Z}^2) + \frac{1-\mu}{R_{13}} + \frac{\mu}{R_{23}} \\
&= \frac{1}{2}\left[(\dot{x} - y)^2 + (\dot{y} + x)^2 + \dot{z}^2\right] + \frac{1-\mu}{r_{13}} + \frac{\mu}{r_{23}} \\
&= \frac{1}{2}\left(\dot{x}^2 + \dot{y}^2 + \dot{z}^2\right) - y\,\dot{x} + x\,\dot{y} - U^*
\end{aligned} \tag{2.12}$$

Recalling:

$$\frac{\partial}{\partial t}\left(\frac{\partial L}{\partial \dot{x}_i}\right) - \frac{\partial L}{\partial x_i} = 0 \tag{2.13}$$

Finally, the Euler-Lagrange equations of motion (EoMs) are obtained:

$$\begin{cases}
\ddot{x} - 2\dot{y} = -U^*_{/x} \\
\ddot{y} + 2\dot{x} = -U^*_{/y} \\
\ddot{z} = -U^*_{/z}
\end{cases}
\rightarrow
\begin{cases}
\dot{x} = v_x \\
\dot{y} = v_y \\
\dot{z} = v_z \\
\dot{v_x} = 2\dot{y} + x - \frac{1-\mu}{r_{13}^3}(x+\mu) - \frac{\mu}{r_{23}^3}(x-1+\mu) \\
\dot{v_y} = -2\dot{x} + y - \frac{1-\mu}{r_{13}^3}y - \frac{\mu}{r_{23}^3}y \\
\dot{v_z} = -\frac{1-\mu}{r_{13}^3}z - \frac{\mu}{r_{23}^3}z
\end{cases} \tag{2.14}$$

Euler-Lagrange EoMs are numerically integrable given an initial condition $(x_0, y_0, z_0, \dot{x}_0, \dot{y}_0, \dot{z}_0)$. See Fig. [2.1] for an illustrative example.

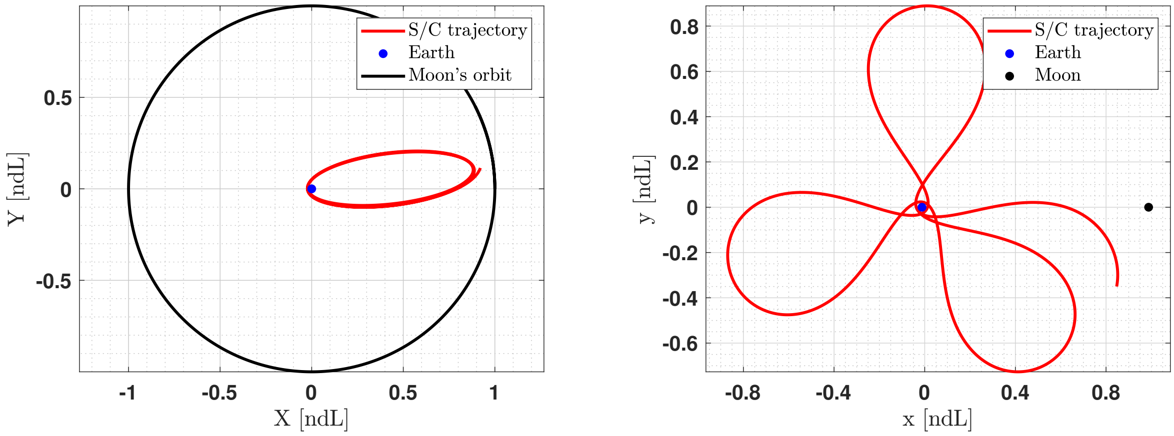

(a) (b)

Figure 2.1: Numerical Euler-Lagrange EoM integration in the Earth-Moon system, implemented according to Pavlak [2010], using for the Earth-Moon system $\mu = 0.0121505856$ non-dimensional gravitational parameter. [**2.1a**] refers to an Earth-centred normalised sidereal frame: the Earth appears fix; the Moon and s/c in orbit around the Earth. Note that due to the presence of the minor primary, the s/c orbit does not appear perfectly elliptical: the Moon perturbs the Keplerian solution. [**2.1b**] The same trajectories in the synodic normalised frame: Earth and Moon appear motionless; the elliptical orbit of the s/c is converted into the characteristic rosette orbit. It shows clearly that the orbit is not closed: in the R3BP it happens only if the ratio between the period of the s/c orbit over the period of the minor primary is finite (resonance condition, see Dichmann et al. [2013] for reference).

2.3.4. Lagrangian Points

Lagrangian points, also called libration points, are the equilibrium points in the synodic reference system. They can be obtained from the EoMs by setting all derivatives to zero.

$$\begin{cases} -U^*_{/x} = 0 \\ -U^*_{/y} = 0 \\ -U^*_{/z} = 0 \end{cases} \rightarrow \begin{cases} x - \frac{1-\mu}{r_{13}^3}(x+\mu) - \frac{\mu}{r_{23}^3}(x-1+\mu) = 0 \\ y - \frac{1-\mu}{r_{13}^3}y - \frac{\mu}{r_{23}^3}y = 0 \\ -\frac{1-\mu}{r_{13}^3}z - \frac{\mu}{r_{23}^3}z = 0 \end{cases} \tag{2.15}$$

It is immediate to consider that the second and third equations of the system can be satisfied for $y = z = 0$ and to look for a solution of the first equation, that reads:

$$x - \frac{1-\mu}{|x+\mu|^3}(x+\mu) - \frac{\mu}{|x-1+\mu|^3}(x-1+\mu) = 0 \tag{2.16}$$

The equation does not admit an analytical solution. A graphical investigation (Fig. 2.2a) proves the existence of three stationary points. These points on the x-axis are called collinear: $L1$ between the two primaries, immediately followed by the gateway $L2$ of the smaller primary. Last is the gateway $L3$ of the major primary. To solve the equation numerically, one defines $\gamma_i \geq 0$ as the distance of Li from the nearest primary, obtaining:

$$
\begin{aligned}
&x_1 = 1 - \mu - \gamma_1 \\
&\quad \rightarrow\ \gamma_1^5 - (3-\mu)\gamma_1^4 + (3-2\mu)\gamma_1^3 - \mu\gamma_1^2 + 2\mu\gamma_1 - \mu = 0 && (2.17)\\
&x_2 = 1 - \mu + \gamma_2 \\
&\quad \rightarrow\ \gamma_2^5 + (3-\mu)\gamma_2^4 + (3-2\mu)\gamma_2^3 - \mu\gamma_2^2 - 2\mu\gamma_2 - \mu = 0 && (2.18)\\
&x_3 = -\mu - \gamma_3 \\
&\quad \rightarrow\ \gamma_3^5 + (7+\mu)\gamma_3^4 + (19+6\mu)\gamma_3^3 + (24+13\mu)\gamma_3^2 + (12+14\mu)\gamma_3 + 7\mu = 0 && (2.19)
\end{aligned}
$$

As initial guess for the Newton-Raphson method to solve the given equation we consider:

$$\gamma_i = \begin{cases} \left(\frac{\mu}{3}\right)^{\frac{1}{3}} & \text{, for } i = 1, 2 \\ \left(\frac{1+\mu}{3}\right)^{\frac{1}{3}} & \text{, for } i = 3 \end{cases} \tag{2.20}$$

After finding the collinear points, let's now drop the assumption $y = 0$. By manipulating the second equation of the system 2.15 we obtain:

$$y\left(1 - \frac{1-\mu}{r_{13}^3} - \frac{\mu}{r_{23}^3}\right) = 0 \tag{2.21}$$

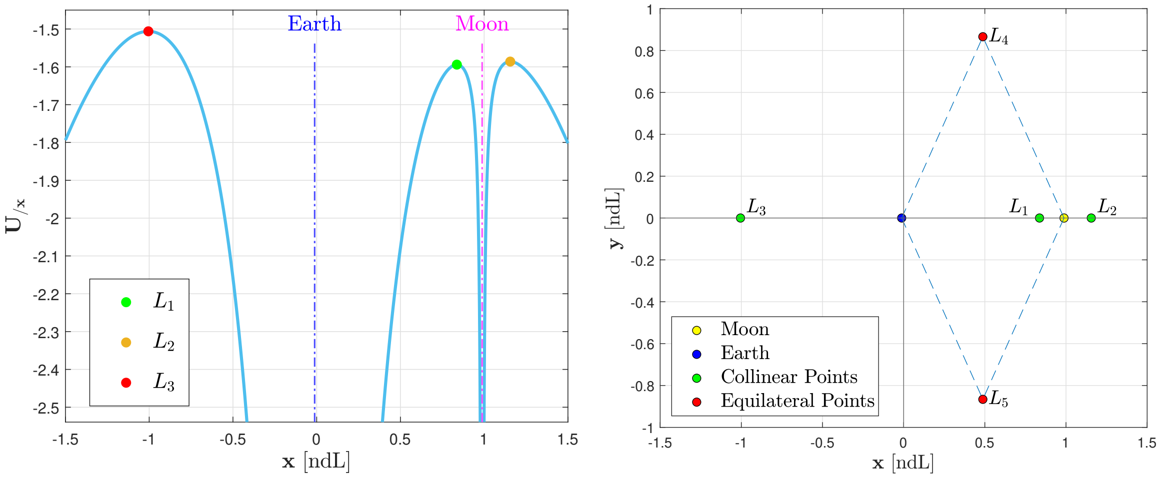

(a) (b)

Figure 2.2: Lagrangian points in the Earth-Moon system. On the left, collinear points are sought by graphical investigation of the $U^*_{/x}$ curve. Three potential wells are evident: the two massive bodies with their gravitational potential, plus the centrifugal potential of the non-inertial reference system. The collinear points are identified as points of maximum. On the right, [**2.2b**] shows the five Lagrangian points on the x-y plane.

This equation is satisfied if $r_{13} = r_{23} = 1$. Since by construction r_{12} is also equal to 1, then the existence of two equilateral Lagrangian points is proven:

$$L4 = \left(\frac{1}{2} - \mu, \frac{\sqrt{3}}{2}, 0\right) \tag{2.22}$$

$$L5 = \left(\frac{1}{2} - \mu, -\frac{\sqrt{3}}{2}, 0\right) \tag{2.23}$$

Finally, solving the third equation of the system for $z \neq 0$ requires $\mu > 1$. Since by definition of the gravitational parameter this is impossible, there do not exist out of plane equilibrium points.

In conclusion, the existence of five Lagrangian points is demonstrated. Of these, three are collinear and two equilateral. In Fig.2.2b a representation of the Lagrangian points in the Earth-Moon system.

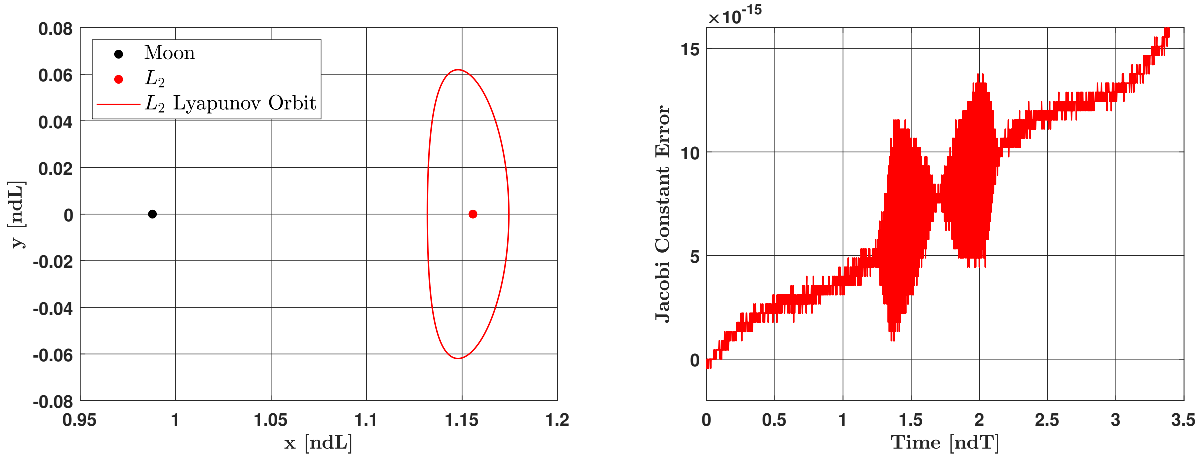

(a)

(b)

Figure 2.3: On the left, it is verified that Jacobi's constant is maintained along the orbit. The verification is carried out on the orbit showed on the right.

2.3.5. Jacobi Integral and Energy

Let's manipulate the Euler-Lagrange EoM as follows:

$$\dot{x}\left(\ddot{x}-2\dot{y}\right)+\dot{y}\left(\ddot{y}+2\dot{x}\right)+\dot{z}\ddot{z}=-\dot{x}U^*_{/x}-\dot{y}U^*_{/y}-\dot{z}U^*_{/z}$$

so that:

$$\frac{1}{2}\frac{d}{dt}(\dot{x}^2+\dot{y}^2+\dot{z}^2)=-\frac{d}{dt}U^*\rightarrow\frac{d}{dt}(-v^2-2U^*)=0$$

A constant in time is therefore found, called Jacobi integral or Jacobi constant:

$$JC=-v^2-2U^* \tag{2.24}$$

Along a trajectory that develops according to its natural dynamics, the Jacobi integral remains constant in time. In Fig. [2.3] computational evidence is provided.

The relationship between the Jacobi constant JC and the mechanical energy of the satellite in the synodic reference system E is immediate:

$$JC = -2\left(\frac{1}{2}v^2 + U^*\right) = -2E \tag{2.25}$$

Thus, the only integral of CR3BP follows from the conservation of mechanical energy E. Using JC to characterise a trajectory also defines its energy level. It should be remarked that by definition the lower JC is, the more energy demanding the trajectory is.

Hill first proposed to represent U^* for $v = 0$ and fixed JC_i, obtaining the Zero Velocity Curve (ZVC). This boundary demarcates a zone not accessible with the current energy level of the trajectory:

$$-JC_i - 2U^* = v^2 \rightarrow -JC_i - 2U^* \geq 0 \rightarrow \begin{cases} -2U^* > JC_i \text{ (Allowed zone)} \\ -2U^* = JC_i \text{ (ZVC)} \\ -2U^* < JC_i \text{ (Forbidden zone)} \end{cases} \tag{2.26}$$

In order to enlarge the accessible zone, the JC_i value must clearly be decreased. Any point beyond the ZVC cannot be reached without additional energy, while all points within the permitted zone can be reached by an accurate design exploiting natural dynamics. The representation provides an immediate picture of the missions that can be designed for a given energy level (Fig.2.4). Graphical investigation also allows sorting the Lagrangian points Li by the corresponding value of JC_i. The order from lowest to highest energy level is $L1, L2$, $L3$. Then follows $L4$ and $L5$ as equal.

Having determined the value of JC_i at the corresponding Li points, Hill allows to distinguish five peculiar situations :

1. for $JC > JC_1$ three separate domains are recognised: the inner domain of the major primary; the inner domain of the minor primary; the outer domain. Starting from

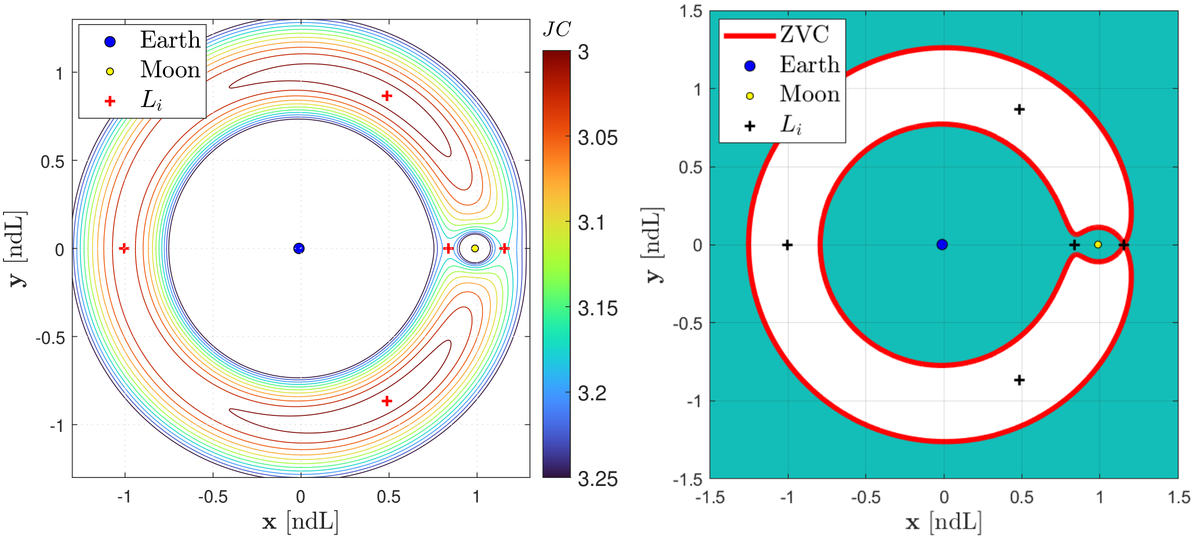

(a)

(b)

Figure 2.4: A representation of the Hill region for the Earth-Moon system. On the left [**2.4a**] shows the variation of JC for zero velocities. Note that trajectories with high JC are confined either in the inner domain of the major primary, or in the inner domain of the minor primary, or in the outer domain. By decreasing JC the sphere around the primaries widens to the point that it opens up the neck region in $L1$ with JC around 3.19. This makes transfers between the two primaries possible. At JC approximately 3.17, the neck region of $L2$ has also gained access, making interplanetary missions possible. For higher energy-demanding trajectory values, $L3$ and lastly the equilateral points can also be reached. On the right [**2.4b**] focuses on the special case of $JC = 3.17$: in red the Zero Velocity Curve, in white the forbidden zone and in cyan the allowed zone.

one of the two primaries, only missions in the corresponding domain are possible; starting from outer space, reentry to the primaries is not possible.

2. $JC_2 < JC < JC_1$: the inner domains overlap in the neck region of $L1$. Transfers between primaries become feasible.

3. $JC_3 < JC < JC_2$: the minor inner domain and the interplanetary domain overlap in the neck region around $L2$. Exploration missions.

4. $JC_4 < JC < JC_3$: the inner domains of the two primaries are no longer distinguishable; the neck region around $L2$ is very large; a third neck region opens around $L3$ allowing different access to interplanetary missions.

5. $JC > JC_4$: it is no longer possible to distinguish any separation between domains. All space is accessible and missions to equilateral points are available.

2.3.6. Hamiltonian EoM

This section derives from the Lagrangian phase space $(x, y, z, \dot{x}, \dot{y}, \dot{z})$ the Hamiltonian phase space (x, y, z, p_x, p_y, p_x). To do so, with the Legendre transformation the momentum p is obtained:

$$p_x = \frac{\partial \mathcal{L}}{\partial \dot{x}} = \dot{x} - y \tag{2.27}$$

$$p_y = \frac{\partial \mathcal{L}}{\partial \dot{y}} = \dot{y} + x \tag{2.28}$$

$$p_z = \frac{\partial \mathcal{L}}{\partial \dot{z}} = \dot{z} \tag{2.29}$$

So, the Hamiltonian is:

$$\begin{aligned} H &= p_x\dot{x} + p_y\dot{y} + p_z\dot{z} - \mathcal{L} \\ &= p_x^2 + p_x y + p_y^2 - p_y x + p_z^2 - \frac{1}{2}(p_x^2 + p_y^2 + p_z^2) - \frac{1-\mu}{r_{13}} - \frac{\mu}{r_{23}} \\ &= \frac{1}{2}\left[(p_x + y)^2 + (p_y - x)^2 + p_z^2\right] - \frac{1}{2}(x^2 + y^2) - \frac{1-\mu}{r_{13}} - \frac{\mu}{r_{23}} \\ &= \frac{1}{2}\left[(p_x + y)^2 + (p_y - x)^2 + p_z^2\right] + U^* \end{aligned} \tag{2.30}$$

Note that the Hamiltonian H is the mechanical energy E as position and momentum function:

$$H = \frac{1}{2}\left[(p_x + y)^2 + (p_y - x)^2 + p_z^2\right] + U^* = \frac{1}{2}(\dot{x}^2 + \dot{y}^2 + \dot{z}^2) + U^* = E$$

The Hamiltonian EoMs are:

$$\begin{cases} \dot{x} = \frac{\partial H}{\partial p_x} \\ \dot{y} = \frac{\partial H}{\partial p_y} \\ \dot{z} = \frac{\partial H}{\partial p_z} \\ \dot{p_x} = -\frac{\partial H}{\partial x} \\ \dot{p_y} = -\frac{\partial H}{\partial y} \\ \dot{p_z} = -\frac{\partial H}{\partial z} \end{cases} \rightarrow \begin{cases} \dot{x} = p_x + y \\ \dot{y} = p_y - x \\ \dot{z} = p_z \\ \dot{p_x} = p_y - x - U^*_{/x} \\ \dot{p_y} = p_x + y - U^*_{/y} \\ \dot{p_z} = -U^*_{/z} \end{cases} \tag{2.31}$$

2.4. Trajectories in the Neck Regions

2.4.1. Literature review

In R2BP, the six integrals of motion define orbits that are conic sections. These invariant structures are the building blocks of a R2BP trajectory design. In the R3BP, the conic sections are no longer constant, but change in time in the inertial reference system. In the synodic reference system, other invariant structures do exist. The investigation, definition, manipulation and connection of these structures is the basis of the multi-body dynamics.

Poincaré [1892, 1893, 1899] considered three different approaches to R3BP: the CR3BP, the ER3BP, and the non-coplanar CR3BP. His work revealed that in the CR3BP there are periodic trajectories given by homocyclic connections. The Space Manifolds are the first structure discovered of CR3BP.

Strömgren [1935] demonstrated the existence of bounded orbits around the Lagrangian points. Stromgren's study inaugurated a fruitful and successful research that continues to produce results up to our day. The increasing number of contributions has required successive comprehensive studies to classify the newly discovered orbits. The numerous families of orbits known today can be grouped into symmetrical, non-symmetrical and quasi-periodic. Their variety and connection provide extreme flexibility to the mission design in the CR3BP.

One of the first comprehensive studies for the classification of symmetrical orbits was carried out by Hénon [1965]. However, just a year later Farquhar [1966] named as ’halo’ the family of 3D orbits symmetrical with respect to the x-z plane that bifurcate from the Lyapunov plane family. The new orbits offer unexpected opportunities for space mission design, nevertheless they are analytically complex to treat. The same year Deprit and Henrard [1966] proposed a numerical procedure of continuation for systematic search of periodic solutions. By Farquhar and Kamel [1973] halo orbits was derived from Lissajous. Hénon [1974] gathers these contributions within the classified orbits.

Richardson [1979] proposed a semi-analytical approach to halo orbits based on the series expansion of EoMs around the given libration point up to third order. Thanks to Richardson, it has become possible to design halo orbits analytically with a good accuracy. The accuracy is not adequate for a real missions, but sufficient to provide educated guess for a numerical approach, as done by Connor Howell [1984].

The search for bounded orbits also concern the equilateral Lagrangian points. Important works in this regard are due to Perdios et al. [1991], Hénon [1997], Henon and Lutze [2002] and Henon [2003]. These contributions composed a structure connecting all Lagrangian points.

2.4.2. Equation of motion about $L1$ and $L2$

Let us consider the second order Taylor expansion of the Hamiltonian of the CR3BP around the equilibrium point Li with $i = 1,\ 2$.

$$\begin{aligned}H_2(\mathbf{x_1}, p) =& H - H|_{eq}\\ &= \sum_i^6 \sum_j^6 \frac{1}{2} H_{/ij}|_{eq} x_{l,i} x_{l,j}\\ &= \frac{1}{2}\left[(p_x + y)^2 + (p_y - x)^2 + p_z^2 - (2c_2 + 1)x^2 + (c_2 - 1)y^2 + c_2 z^2\right] \qquad (2.32)\end{aligned}$$

where:

$$\begin{aligned}&\mathbf{x_1} = \mathbf{x} - \mathbf{x}|_{\mathbf{eq}}\\ &c_2 = \frac{1-\mu}{(1 \mp \gamma_i)^3} + \frac{\mu}{\gamma_i^3} \qquad (2.33)\end{aligned}$$

The sign - in c_2 refers to $L1$, while the sign $+$ to $L2$. Hence, the linearized equation of motion about $L1$ and $L2$ in Hamiltonian form are:

$$\begin{cases}\dot{x} = H_{2/p_x}\\ \dot{y} = H_{2/p_y}\\ \dot{z} = H_{2/p_z}\\ \dot{p_x} = -H_{2/x}\\ \dot{p_y} = -H_{2/y}\\ \dot{p_z} = -H_{2/z}\end{cases} \rightarrow \begin{cases}\dot{x} = p_x + y\\ \dot{y} = p_y - x\\ \dot{z} = p_z\\ \dot{p_x} = p_y - x + (2c_2 + 1)x\\ \dot{p_y} = p_x + y - (c_2 - 1)y\\ \dot{p_z} = -2z\end{cases} \qquad (2.34)$$

While the linearized EoM about $L1$ and $L2$ in Lagrangian form are:

$$\begin{cases} \dot{x} = v_x \\ \dot{y} = v_y \\ \dot{z} = v_z \\ \dot{v_x} = 2\dot{y} + (2c_2 + 1)x \\ \dot{v_y} = -2\dot{x} - (c_2 - 1)y \\ \dot{v_z} = -2c_2 z \end{cases} \tag{2.35}$$

The associated linearized energy E_2 is:

$$E_2 = \frac{1}{2}\left[v_x^2 + v_y^2 + v_z^2 - (2c_2 + 1)x^2 + (c_2 - 1)y^2 + c_2 z^2\right] \tag{2.36}$$

Similarly, the n-order Taylor expansion is:

$$H_n(\mathbf{x_1}, \mathbf{p}) = \frac{1}{2}\left(p_x^2 + p_y^2 + p_z^2\right) + yp_x - xp_y - \sum_{n\geq 2} c_n T_n \tag{2.37}$$

where:

$$c_n = (-1)^n \frac{(1-\mu)\gamma_k^{n-2}}{(1 \mp \gamma_k)^{n+1}} + (\pm 1)^n \frac{\mu}{\gamma_k^3} \tag{2.38}$$

The term T_n is computed with the Legendre polynomial recursive relationship:

$$\begin{cases} T_0 = 1 \\ T_1 = x \\ T_n = \frac{2n-1}{n} x T_{n-1} - \frac{n-1}{n}(x^2 + y^2 + z^2) T_{n-2} \end{cases} \tag{2.39}$$

The linearized EoM up to n order in Lagrangian form about $L1$ and $L2$ are:

$$\begin{cases} \dot{x} = v_x \\ \dot{y} = v_y \\ \dot{z} = v_z \\ \dot{v_x} - 2\dot{y} - (2c_2 + 1)x = \frac{\partial}{\partial x} \sum_{n \geq 3} c_n T_n \\ \dot{v_y} - -2\dot{x} + (c_2 - 1)y = \frac{\partial}{\partial y} \sum_{n \geq 3} c_n T_n \\ \dot{v_z} + 2z = \frac{\partial}{\partial z} \sum_{n \geq 3} c_n T_n \end{cases} \tag{2.40}$$

Expansion up to the 15th order is used in the practice of Mission Design to maintain a proper accuracy (Koon et al. [2011]). However, as a first approximation the second-order expansion is a good assumption.

2.4.3. Phase Space about $L1$ and $L2$

The linearised EoM form $\dot{\mathbf{u}} = \mathbf{A}\mathbf{u}$ allows to derive the eigenvalue problem:

$$\mathbf{A}\mathbf{u} = \beta\mathbf{u} \rightarrow (\mathbf{A} - \beta\mathbf{I})\mathbf{u} = 0 \rightarrow |\mathbf{A} - \beta\mathbf{I}| = 0 \tag{2.41}$$

where the characteristic polynomial $p(\beta^2)$:

$$p(\beta^2) : \beta^6 + 2\beta^4 + (1 + 3c_2 - 3c_2^2)\beta^2 + c_2 + c_2^2 - 2c_2^3 = 0 \tag{2.42}$$

The corresponding eigenvalues and eigenvectors are:

$$\begin{aligned}
&\boldsymbol{\beta} = (\pm\lambda, \pm j\omega_p, \pm j\omega_\nu) \\
&\mathbf{u}_{\pm\lambda} = (1, \mp\sigma, 0, \pm\lambda, -\lambda\sigma, 0)^T \\
&\mathbf{u}_{\pm\omega_\mathbf{p}} = (1, \mp j\tau, 0, \pm j\omega_p, \omega_p\tau, 0)^T \\
&\mathbf{u}_{\pm\omega_\nu} = (0, 0, 1, 0, 0, \pm j\omega_\nu)^T \\
&\text{where:} \\
&\lambda^2 = \frac{\sqrt{9c_2^2 - 8c_2} + c_2 - 2}{2} \\
&\omega_p^2 = \frac{\sqrt{9c_2^2 - 8c_2} - c_2 + 2}{2} \\
&\omega_\nu^2 = c_2 \\
&\sigma = \frac{2\lambda}{\lambda^2 + c_2 - 1} \\
&\tau = -\frac{\omega_p^2 + 2c_2 + 1}{2\omega_p}
\end{aligned} \tag{2.43}$$

Let us consider a symplectic change of coordinates, such that:

$$\begin{aligned}
&\mathbf{x} = \mathbf{C}\boldsymbol{\xi} \\
&\text{where:} \\
&\mathbf{x} = (x, y, z, p_x, p_y, p_z) \\
&\boldsymbol{\xi} = (\xi_1, \eta_1, \zeta_1, \xi_2, \eta_2, \zeta_2)
\end{aligned} \tag{2.44}$$

The symplectic matrix **C** is given by the eigenvectors appropriately rescaled:

$$\mathbf{C} = \left[\frac{\mathbf{u}_\lambda}{||\mathbf{u}_\lambda||} s_1, \frac{\mathbf{u}_{\omega_p}}{||\mathbf{u}_{\omega_p}||} s_2, \frac{\mathbf{u}_{\omega_\nu}}{||\mathbf{u}_{\omega_\nu}||} s_3, \frac{\mathbf{u}_{-\lambda}}{||\mathbf{u}_{-\lambda}||} s_1, \frac{\mathbf{u}_{-\omega_p}}{||\mathbf{u}_{-\omega_p}||} s_2, \frac{\mathbf{u}_{-\omega_\nu}}{||\mathbf{u}_{-\omega_\nu}||} s_3 \right] \tag{2.45}$$

with scaling factors:

$$s_1 = \frac{1}{\sqrt{2\lambda[(4+3c_2)\lambda^2 + 4 + 5c_2 - 6c_2^2]}}$$

$$s_2 = \frac{1}{\sqrt{2\lambda[(4+3c_2)\lambda^2 - 4 - 5c_2 + 6c_2^2]}}$$

$$s_3 = \frac{1}{\sqrt{\omega_\nu}}$$

Referring to the coordinate system $\boldsymbol{\xi}$, the Hamiltonian assumes the normal form $H(\boldsymbol{\xi})$:

$$H(\boldsymbol{\xi}) = \lambda \xi_1 \xi_2 + \frac{1}{2}\omega_p(\eta_1^2 + \eta_2^2) + \frac{1}{2}\omega_\nu(\zeta_1^2 + \zeta_2^2) \tag{2.46}$$

Then, the linearized EoM in the eigenvector phase space is:

$$\begin{cases} \dot{\xi}_1 = H(\boldsymbol{\xi})_{/\xi_2} \\ \dot{\eta}_1 = H(\boldsymbol{\xi})_{/\eta_2} \\ \dot{\zeta}_1 = H(\boldsymbol{\xi})_{/\zeta_2} \\ \dot{\xi}_2 = -H(\boldsymbol{\xi})_{/\xi_2} \\ \dot{\eta}_2 = -H(\boldsymbol{\xi})_{/\eta_2} \\ \dot{\zeta}_2 = -H(\boldsymbol{\xi})_{/\zeta_2} \end{cases} \rightarrow \begin{cases} \dot{\xi}_1 = \lambda \xi_1 \\ \dot{\eta}_1 = \omega_p \eta_2 \\ \dot{\zeta}_1 = \omega_\nu \zeta_2 \\ \dot{\xi}_2 = -\lambda \xi_2 \\ \dot{\eta}_2 = -\omega_p \eta_1 \\ \dot{\zeta}_2 = -\omega_\nu \eta_1 \end{cases} \tag{2.47}$$

Finally, the linearized EoM solutions in the eigenvector phase space is:

$$\begin{cases} \xi_1(t) = \xi_1(t_0)e^{\lambda t} \\ \xi_2(t) = \xi_2(t_0)e^{-\lambda t} \\ \eta(t) = \eta(t_0)e^{-j\omega_p t} \quad \text{with: } \eta(t) = \eta_1(t) + j\eta_2(t) \\ \zeta(t) = \zeta(t_0)e^{-j\omega_\nu t} \quad \text{with: } \zeta(t) = \zeta_1(t) + j\zeta_2(t) \end{cases} \tag{2.48}$$

Further, set an energy level ε it is obtained the equation:

$$\frac{\lambda}{4}(\xi_2 + \xi_1)^2 + \frac{1}{2}\omega_p(\eta_1^2 + \eta_2^2) + \frac{1}{2}\omega_\nu(\zeta_1^2 + \zeta_2^2) = \varepsilon + \frac{\lambda}{4}(\xi_2 - \xi_1)^2 \tag{2.49}$$

Note that:

- the product $\xi_1(t)\xi_2(t)$ is constant.
- $|\eta(t)|$ and $|\zeta(t)|$ are constants.
- $|\xi_2(t) - \xi_1(t)|$ denote an upper and lower bound.
- $\xi_1(t)\xi_2(t) = \frac{\varepsilon}{\lambda}$ is a hyperbole bound.

According to Koon et al. [2011], overall the flow allows to discern (9) orbit classes into the following four categories:

$$\text{(1) Central Manifold s.t.} \begin{cases} \xi_1 = \xi_2 = 0 \\ \frac{\omega_p}{2}(\eta_1^2 + \eta_2^2) + \frac{\omega_\nu}{2}(\zeta_1^2 + \zeta_2^2) = \varepsilon \end{cases}$$

$$\text{(2) Stable Manifolds s.t.} \begin{cases} \xi_1 = 0 \\ \xi_2 \lessgtr 0 \\ \frac{\omega_p}{2}(\eta_1^2 + \eta_2^2) + \frac{\omega_\nu}{2}(\zeta_1^2 + \zeta_2^2) = \varepsilon \end{cases}$$

$$\text{(2) Unstable Manifolds s.t.} \begin{cases} \xi_1 \lessgtr 0 \\ \xi_2 = 0 \\ \frac{\omega_p}{2}(\eta_1^2 + \eta_2^2) + \frac{\omega_\nu}{2}(\zeta_1^2 + \zeta_2^2) = \varepsilon \end{cases}$$

(2) Transit Orbits s.t. $\xi_1(t)\xi_2(t) > 0$

(2) Rejecting Orbits s.t. $\xi_1(t)\xi_2(t) < 0$

Let U be $(\boldsymbol{u_\lambda}, \boldsymbol{u_{-\lambda}}, \boldsymbol{u_{\omega_p}}, \boldsymbol{u_{-\omega_p}}, \boldsymbol{u_{\omega_\nu}}, \boldsymbol{u_{-\omega_\nu}})$, the solution of linearized EoM is given by:

$$\mathbf{x_i}(t) = \sum_{j=1}^{6} A_j e^{\beta_j t} \mathbf{U_{i,j}} \tag{2.50}$$

So that:

$$\begin{cases} x(t) = A_1 e^{\lambda t} + A_2 e^{-\lambda t} + 2Re\{(A_3 + jA_4)e^{j\omega_p t}\} \\ y(t) = -\sigma A_1 e^{\lambda t} + \sigma A_2 e^{-\lambda t} + 2Re\{(A_3 + jA_4)e^{j\omega_p t}(-j\tau)\} \\ z(t) = 2Re\{(A_5 + jA_6)e^{j\omega_\nu t} j\nu\} \end{cases} \tag{2.51}$$

Finally:

$$\begin{cases} x(t) = A_1 e^{\lambda t} + A_2 e^{-\lambda t} + A_x \cos(\omega_p t + \phi) \\ y(t) = -\sigma A_1 e^{\lambda t} + \sigma A_2 e^{-\lambda t} + \tau A_x \sin(\omega_p t + \phi) \\ z(t) = A_z \cos(\omega_\nu t + \psi) \end{cases} \tag{2.52}$$

It's remarkable that the in-plane motion and the out-of-plane motion are decoupled. The arbitrary constants $(A_1, A_2, A_x, A_z, \phi, \psi)$ define the orbit.

2.4.4. Central manifold

Let us consider Eq. 2.52. If $A_1 = A_2 = 0$, then the spacecraft moves on the central manifold. The exponential terms vanish with the corresponding modes and the motion is determined by the remaining pure imaginary eigenvalues. In this case the linear EoMs

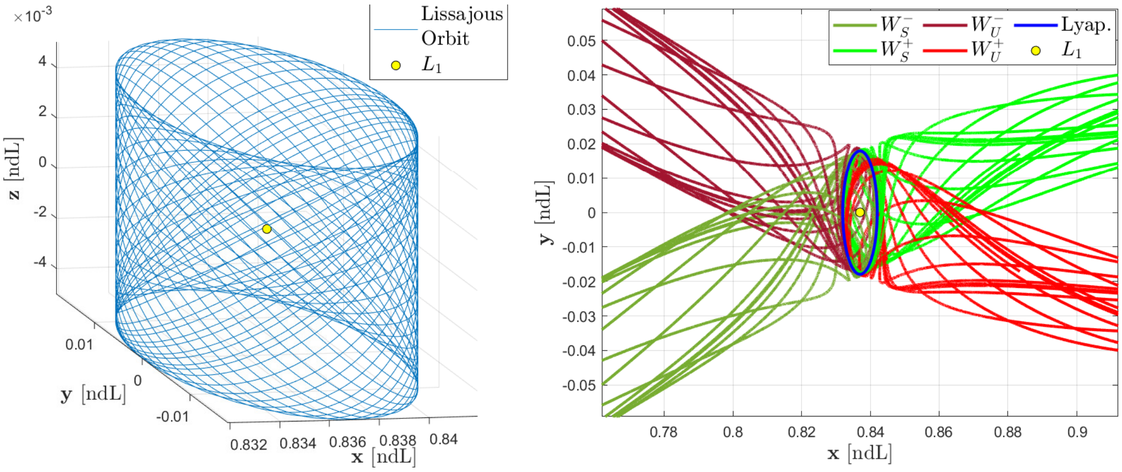

(a) (b)

Figure 2.5: Examples of trajectories belonging to the central and the hyperbolic manifolds in the neighborhood of L1 in the Earth-Moon system in non-dimensional units. Left: Lissajous orbit. Right: stable (green) and unstable (red) manifolds associated with a planar Lyapunov orbit (blue).

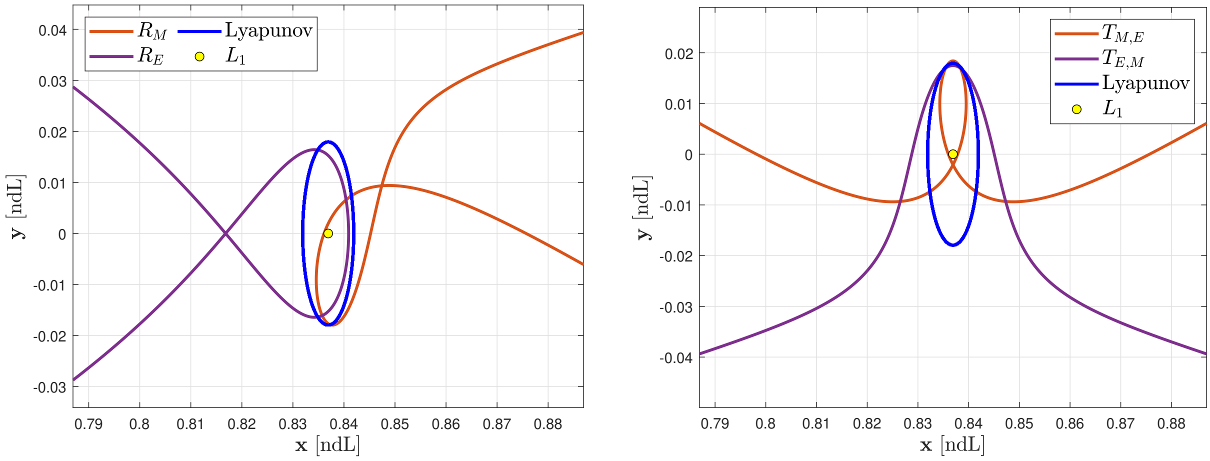

(a) (b)

Figure 2.6: Some examples of T transiting and R rejecting trajectories in the $L1$ region in the Earth-Moon system. Note that these trajectories are dominated by the asymptotic manifolds around $L1$. All of them can only come from an unstable manifold and go throw a stable one.

describe a bounded motion:

$$\begin{cases} x(t) = A_x \cos(\omega_p t + \phi) \\ y(t) = \tau A_x \sin(\omega_p t + \phi) \\ z(t) = A_z \cos(\omega_\nu t + \psi) \end{cases} \tag{2.53}$$

That is, a Lissajous orbit. This is a quasi-periodic orbit, with the two frequencies given by ω_p and ω_v.

Lyapunov orbits

Two families of periodic orbits stem from the given collinear equilibrium point. They are the planar Lyapunov orbits and the vertical Lyapunov orbits. In the former case, the motion is planar with frequency associated with ω_p. In the latter case, the motion is three-dimensional and associated with ω_v.

Halo orbits $(A_1 = A_2 = 0, \omega = \nu)$

Halo orbits bifurcate from the planar Lyapunov orbits. They are a family of three-dimensional, periodic orbits that occur when the in-plane frequency and the out-of-plane frequency are equal. Since the frequencies ω_p and ω_ν are determined by the gravitational parameter μ, halo orbits do not result in linear analysis. In other words, a halo orbit requires higher order terms in the series expansion. Namely, going up in order the frequencies are redefined as:

$$\omega = \omega_p + \sum_{i,j} \omega_{i,j} A_x^i A_z^j \qquad \text{(in plane frequency)} \tag{2.54}$$

$$\nu = \omega_\nu + \sum_{i,j} \nu_{i,j} A_x^i A_z^j \qquad \text{(out-of-plane frequency)} \tag{2.55}$$

Assuming $\omega = \nu$, the halo orbit general solution is:

$$\begin{cases} x(t) = \sum_{i,j=1}^{\infty} \left[a_{ijk} \cos(k\theta) \right] A_x^i A_z^j \\ y(t) = \sum_{i,j=1}^{\infty} \left[b_{ijk} \cos(k\theta) \right] A_x^i A_z^j \\ z(t) = \sum_{i,j=1}^{\infty} \left[c_{ijk} \cos(k\theta) \right] A_x^i A_z^j \end{cases} \tag{2.56}$$

with:

$$\theta = \omega t + \phi$$

As an example, referring to third order EoMs expansion a correction $\Delta = \omega_p^2 - c_2$ (remind: $\omega_\nu^2 = c_2$) must be added to impose equality of frequencies:

$$\begin{cases} \ddot{x} - 2\dot{y} - (2c_2 + 1)x = \frac{3}{2}c_3(2x^2 - y^2 - z^2) + 2c_4 x(2x^2 - 3y^2 - 3z^2) \\ \ddot{y} + 2\dot{x} + (c_2 - 1)y = -3c_3 xy - \frac{3}{2}c_4 y(4x^2 - y^2 - z^2) \\ \ddot{z} + \omega_p^2 z = -3c_3 xz - \frac{3}{2}c_4 z(4x^2 - y^2 - z^2) + \Delta z \end{cases} \tag{2.57}$$

Now, on the left-hand side the unknown general solution up to third order is replaced, while on the right-hand side is replaced the known solution of second order. Equalising member to member, two constraints result on amplitudes and phase:

$$\begin{aligned} & l_1 A_x^2 + l_2 A_z^2 + \Delta = 0 \\ & \psi - \phi = m\frac{\pi}{2} \qquad\qquad \text{where: } m = 1, 3 \end{aligned} \tag{2.58}$$

With $m = 1$ then $A_z > 0$ and the halo orbit is northern, while with $m = 3$ follows $A_z < 0$ and the halo orbit is southern. Note that halo orbits can be identify by a single parameters, usually A_z. For a complete description, see Richardson [1979].

2.4.5. Hyperbolic manifolds

The linear analysis proposed previously shows that the collinear equilibrium points are unstable. This means that apart from the bounded orbits corresponding to the pure imaginary eigenvalues, there exist trajectories that depart from the given equilibrium point (unstable manifold) and trajectories that approach it forward in time (stable manifold). More in detail if A_1 and A_2 of Eq. 2.52 are different from 0, then we have:

Stable Manifolds $W^s_\pm$ when $A_1 = 0, A_2 = \pm\epsilon$ s.t.:

$$\begin{cases} x(t) = \pm\epsilon e^{-\lambda t} + A_x \cos(\omega_p t + \phi) \\ y(t) = \pm\sigma\epsilon e^{-\lambda t} + \tau A_x \sin(\omega_p t + \phi) \\ x(t) = A_z \cos(\omega_\nu t + \psi) \end{cases} \tag{2.59}$$

Unstable Manifolds $W^u_\pm$ when $A_1 = \pm\epsilon, A_2 = 0$ s.t.:

$$\begin{cases} x(t) = \pm\epsilon e^{\lambda t} + A_x \cos(\omega_p t + \phi) \\ y(t) = \mp\sigma\epsilon e^{\lambda t} + \tau A_x \sin(\omega_p t + \phi) \\ x(t) = A_z \cos(\omega_\nu t + \psi) \end{cases} \tag{2.60}$$

Transit Orbits when $A_1 A_2 < 0$

Rejecting Orbits when $A_1 A_2 > 0$

where ϵ is a small displacement.

2.5. State Transition Matrix

Given a natural dynamics $\dot{\mathbf{x}}(t) = \mathbf{f}(\mathbf{x}(t))$ and a reference solution $\bar{\mathbf{x}}(t)$, define a perturbed trajectory $\tilde{\mathbf{x}}(t)$ with displacement $\delta\mathbf{x}(t) = \tilde{\mathbf{x}}(t) - \bar{\mathbf{x}}(t)$. Then:

$$\delta\dot{\mathbf{x}}(t) = \mathbf{f}(\tilde{\mathbf{x}}(t)) - \mathbf{f}(\bar{\mathbf{x}}(t)) \tag{2.61}$$

Assume the displacement $\delta\mathbf{x}(t)$ small enough that a linear approximation can be applied:

$$\delta\dot{\mathbf{x}}(t) = \mathbf{A}(t)\delta\mathbf{x}(t) \qquad \text{with:} \quad \mathbf{A}(t) = \mathbf{J}_{\mathbf{f}}(\bar{\mathbf{x}}(t)) \tag{2.62}$$

Referring to Euler-Lagrange EoMs with state vector (x, y, z, v_x, v_y, v_z), the Jacobian matrix associated with $\mathbf{f}(\mathbf{x})$ is:

$$\mathbf{A}(t) = \begin{bmatrix} \mathbf{0_3} & \mathbf{I_3} \\ -\mathbf{U}^*_{/\mathbf{xx}} & \mathbf{2\Omega} \end{bmatrix}_{\bar{\mathbf{x}}(t)} \tag{2.63}$$

where:

$$\begin{aligned}
&\mathbf{\Omega} = \begin{bmatrix} 0 & 1 & 0 \\ -1 & 0 & 0 \\ 0 & 0 & 0 \end{bmatrix} \quad , \quad \mathbf{U}^*_{/\mathbf{xx}} = \begin{bmatrix} U^*_{/xx} & U^*_{/xy} & U^*_{/xz} \\ U^*_{/yx} & U^*_{/yy} & U^*_{/yz} \\ U^*_{/zx} & U^*_{/zy} & U^*_{/zz} \end{bmatrix} \\
&U^*_{/xx} = -1 + \frac{r_1^2 - 3(x+\mu)^2}{r_1^5}(1-\mu) + \frac{r_2^2 - 3(x-1+\mu)^2}{r_2^5}\mu \\
&U^*_{/yy} = -1 + \frac{r_1^2 - 3y^2}{r_1^5}(1-\mu) + \frac{r_2^2 - 3y^2}{r_2^5}\mu \\
&U^*_{/zz} = \frac{r_1^2 - 3z^2}{r_1^5}(1-\mu) + \frac{r_2^2 - 3z^2}{r_2^5}\mu \\
&U^*_{/xy} = U^*_{/yx} = -\frac{2y(x+\mu)}{r_1^5}(1-\mu) - \frac{3y(x-1+\mu)}{r_2^5}\mu \\
&U^*_{/xz} = U^*_{/zx} = -\frac{3z(x+\mu)}{r_1^5} - \frac{3z(x-1+\mu)}{r_2^5}\mu \\
&U^*_{/yz} = U^*_{/zy} = -\frac{3yz}{r_1^5}(1-\mu) - \frac{3yz}{r_2^5}\mu
\end{aligned} \tag{2.64}$$

Similarly, define $\phi(t, \mathbf{x_0})$ the flow mapping the initial state $\mathbf{x}(t_0) = \mathbf{x_0}$ to the final state $\mathbf{x}(t)$ s.t.

$$\mathbf{x}(t) = \phi(t, \mathbf{x_0}) \tag{2.65}$$

Then, applying the definition of the displacement:

$$\delta\mathbf{x}(t) = \phi(t, \tilde{\mathbf{x}}_\mathbf{0}) - \phi(t, \bar{\mathbf{x}}_\mathbf{0}) \tag{2.66}$$

By applying a first-order Taylor expansion:

$$\delta\mathbf{x}(t) = \mathbf{\Phi}(t, \bar{\mathbf{x}}(t))\delta\mathbf{x_0} \qquad \text{with:} \quad \mathbf{\Phi}(t, \bar{\mathbf{x}}(t)) = \mathbf{J}_\Phi(t, \bar{\mathbf{x}}_\mathbf{0}) \tag{2.67}$$

Where $\mathbf{\Phi}(t, \mathbf{x_0})$ is the State Transition Matrix (STM), that can be evaluated numerically, by solving:

$$\dot{\mathbf{\Phi}}(t, \mathbf{x_0}) = \mathbf{A}(t)\mathbf{\Phi}(t, \bar{\mathbf{x}}(t)) \tag{2.68}$$

Finally, the STM is numerically obtained integrating a system of 42 ODES. Take care that since the matrix $\mathbf{A}(t)$ must be estimated along the reference trajectory $\bar{\mathbf{x}}(t)$, then the STM and the reference trajectory are integrated together.

$$\begin{cases} \dot{\mathbf{x}}(t) = \mathbf{f}(\mathbf{x}(t)) \\ \dot{\mathbf{\Phi}}(t, \mathbf{x_0}) = \mathbf{A}(t)\mathbf{\Phi}(t, \bar{\mathbf{x}}(t)) \\ \mathbf{x}(t_0) = \mathbf{x_0} \\ \mathbf{\Phi}(t_0, \mathbf{x_0}) = \mathbf{I_6} \end{cases} \tag{2.69}$$

Monodromy matrix

The monodromy matrix $\mathbf{M}$ is the STM after a time equal to the orbital period T, that is:

$$\mathbf{M} = \mathbf{\Phi}(T, \mathbf{x_0}) \tag{2.70}$$

The monodromy matrix allows to investigate the sensitivity of a state i.e., whether given a perturbation $\delta\mathbf{x_0}$ it grows or vanishes in time.

First of all it is observed that by definition:

$$\delta\mathbf{x}(T) = \mathbf{M}\delta\mathbf{x_0} \tag{2.71}$$

Such that, after a time span equal to k times the period T:

$$\delta\mathbf{x}(kT) = \mathbf{M}^k\delta\mathbf{x_0} \tag{2.72}$$

Considered the eigenpairs $(\lambda_n, \mathbf{e_n})$ of matrix $\mathbf{M}$, assume first that the perturbation belongs to eigenvetor direction $\mathbf{e_n}$. Thus:

$$\delta\mathbf{x}(kT) = \lambda_n^k \delta x_0 \mathbf{e_n} \tag{2.73}$$

Therefore in the specific case under consideration, the perturbation propagates along the same direction of the considered mode. It's damped when $|\lambda_n| < 1$, otherwise the state is unstable.

These observations are immediately extended to the general case. In fact, any perturbation is a combination of system modes and can be decomposed on the eigenvector axes. Accordingly, the eigenpairs of $\mathbf{M}$ provide the linear analysis of orbit local sensitivity to a small state perturbation. The dynamics is stable if $|\lambda_n| < 1 \ \forall n$, while it will become increasingly sensitive as $|\lambda_n| \gg 1$.

The CR3BP is highly sensitive. In the case of orbits associated with L1 and L2, the 6 eigenvalues of their monodromy matrix are:

$$\begin{aligned} &\lambda_1, \lambda_2, \lambda_3, \lambda_4 \in \mathbb{R} && \lambda_5, \lambda_6 \in \mathbb{I} \\ &\lambda_1 > 1 && |\lambda_5| = 1 \\ &\lambda_2 = \frac{1}{\lambda_1} && \lambda_6 = \bar{\lambda}_5 \\ &\lambda_3 = \lambda_4 = 1 && \end{aligned} \tag{2.74}$$

Remarks:

- λ_1 is the dominant eigenvalue associated with the unstable mode, so the eigenvector $\mathbf{e_1}$ points to the unstable direction of perturbation. For medium and large halo orbits $\boldsymbol{\lambda_1} >> 1$, thus it's related to a hyperbolic dynamics.

- $\mathbf{e_2}$ is tangent to the local stable manifolds. Any perturbation in this direction vanishes in time e.g., in a station-keeping strategy perturbations in this direction do not need to be compensated via correction manoeuvres.

- λ_3 is related to non-unstable mode i.e., neutral direction. $\mathbf{e_3}$ allows the generation of the orbit family. Each orbit in the family differs in energy i.e., amplitude and period.

- Perturbations in directions $\mathbf{e_5}, \mathbf{e_6}$ generate trajectories around the reference orbit bounded within a *Torus*, such us quasi-halo orbits.

2.6. Poincaré map

The integration of the state vector can generate an overwhelming wealth of information, a cumbersome amount to process that hides the information of interest. A way to obtain of a concise picture of the available opportunities is the implementation of a Poincaré map. In this way, the size of the dynamical system becomes $n-1$.

- the dynamical system changes to a discrete form from the continuous that it was. So instead of having to deal with continuous trajectories, just points are considered.
- A target state is set and design variables are selected. Therefore, the analysis proceeds further on these elements of interest.

The Poincaré map is for instance useful to compute heteroclinic and homoclinic connections and to design insertion maneuvers.

To generate a Poincaré map for a n-dimensional dynamical system, it is first necessary to choose a hypersurface transverse to its flow and $n-1$-dimensional. The transversality condition implies that no trajectory remains on the hyperplane and every trajectory intersects it in the same direction. The transversality condition leaves a margin of flexibility, filled by design evaluations e.g., distance from the primaries. Anyway, there is no unique criterion for the choice of Poincaré section and the resulting map.

Once the hyperplane is selected, an initial state of interest is set and integrated forward or backward until the section is intersected: the initial state is thus mapped onto the section. It continues in this way until the output of interest is found.

Note that the map of a periodic orbit must result in a point. Around this point, ordered structures associated with quasi-periodic orbits are visible (Fig. 2.7).

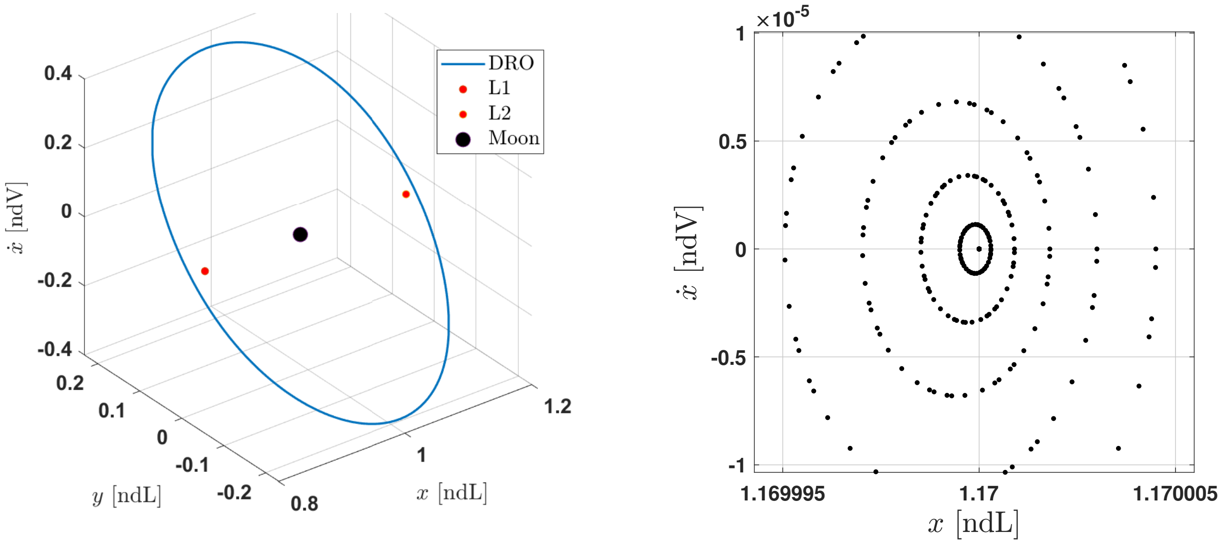

(a)

(b)

Figure 2.7: The baseline orbit of EM-1 mission is a Distant Retrograde Orbit (DRO) in cislunar space with non-dimensional initial conditions $\mathbf{s_0} = [1.17, 0, 0, 0, -0.489780292125578, 0]^T$ and an orbital period of approximately 13 days. [**2.7a**] shows the orbit of EM-1. [**2.7b**] is the Poincaré map obtained for $y = 0$ and $\dot{y} < 0$. Note the central point representing the DRO periodic orbit and the attractive mapping structure around

2.7. Differential correction method

Due to the high sensitivity of the CR3BP, the initial state obtained by means of the semi-analytical approximation might be not accurate enough to get a periodic solution. See Fig. 2.8 for an example.

However, the semi-analytical solution is a good reference first guess to start an iterative differential correction process.

Let's assume it is available an educated guess for the initial state $\mathbf{s_0}$. Planar Lyapunov orbits are symmetric about the y-axis and intersect the x-axis perpendicularly: a initial state for a Lyapunov orbit has the form $(x_0, 0, 0, 0, \dot{y}_0, 0)$. In order to retrieve the accurate initial state:

1. First of all a Poincaré section is selected. For a planar Lyapunov orbit, we choose

y=0.

2. Then, it is guessed the time span t_f required to s/c to reach the Poincaré section. Note that t_f should be about half of the orbital period.

3. The initial state $\mathbf{s_0}$ is integrated by means of EoMs coupled with its State Transition Matrix until the time t_f. In this way a final state $\mathbf{x_f}$ is computed, as well as the STM $\mathbf{\Phi}(t_f, \mathbf{s_0})$.

4. It is known that onto on the Poicaré section the target state $\mathbf{x_t}$ has form $(x_t, 0, 0, 0, \dot{y}_t, 0)$. Note that:

   - $z(t), \dot{z}(t)$ are zero $\forall t$ since we are considering planar Lyapunov orbits.
   - x_t and $\dot{y}_t$ are free and unknown variables.
   - there are two target: zero y_t (symmetry) and $\dot{x}_t$ (perpendicularity).

5. So there are three available variables $(x_0, \dot{y}_0, t_f)$, while only two variables are targeted. In arbitrary way, let x_0 be a fixed value and $\dot{y}_0, t_f$ design variables. Of course, a different choice may be made.

6. By difference between the target vector $\mathbf{x_t}$ and the final vector $\mathbf{x_f}$, it is computed the target error $[\delta y_f, \delta \dot{x}_f]^T$ at time t_f.

7. Determine the design error:

$$\begin{bmatrix} \delta \dot{y}_0 \\ \delta t_f \end{bmatrix} = \begin{bmatrix} \frac{\delta y_f}{\delta \dot{y}_0} & \frac{\delta y_f}{\delta t_f} \\ \frac{\delta \dot{x}_f}{\delta \dot{y}_0} & \frac{\delta \dot{x}_f}{\delta t_f} \end{bmatrix}^{-1} \begin{bmatrix} \delta y_f \\ \delta \dot{x}_f \end{bmatrix} \tag{2.75}$$

   By definition, the matrix terms are known from the STM and EoMs.

$$\begin{bmatrix} \frac{\delta y_f}{\delta \dot{y}_0} & \frac{\delta y_f}{\delta t_f} \\ \frac{\delta \dot{x}_f}{\delta \dot{y}_0} & \frac{\delta \dot{x}_f}{\delta t_f} \end{bmatrix} = \begin{bmatrix} \mathbf{\Phi_{2,5}} & \dot{y}(t_f) \\ \mathbf{\Phi_{4,5}} & \ddot{x}(t_f) \end{bmatrix} \tag{2.76}$$

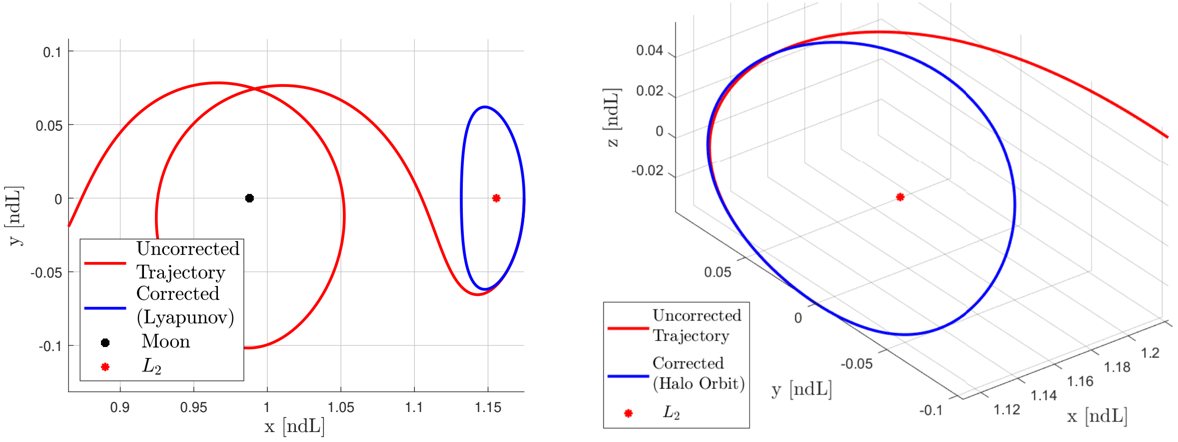

(a) (b)

Figure 2.8: Examples of the application of the differential correction method for the construction of Lyapunov [**2.8a**] and halo [**2.8b**] orbits, the guesses on the initial state $\mathbf{s_{0,g}}$ are respectively $[1.1745, 0, 0, 0, -0.1231, 0]^T$ and $[1.110, 0, -0.037, 0, 0.210, 0]^T$. These are educated choices taken from the literature (Grebow [2006]). After about 5 iterations the algorithm finds for Lyapunov the initial condition $[1.1745, 0, 0, 0, -0.1115, 0]^T$, while for southern halo $[1.1100, 0, -0.0370, 0, 0.2057, 0]^T$. In red is drawn the trajectory generated by the guess, in blue the trajectory obtained by the algorithm. Note how, due to the high sensitivity of the dynamics of CR3BP, even a good guess quickly diverges towards the inner or outer domain.

8. By computing the design error, $\mathbf{s_0}$ and t_f are updated.
9. Steps 3, 6, 7 and 8 are reiterated until the target error falls below an admissible tolerance.
10. Finally, the refined $\mathbf{s_0}$ is integrated for a time span 2tf and the orbit is drawn.

Halo orbits are obtained following the same strategy. Just few considerations are necessary to make it fit. First of all, halo orbits are symmetrical respect to the x-z plane and intersect this plan perpendicularly: a initial state vector for a halo orbit takes the form $(x_0, 0, z_0, 0, \dot{y}_0, 0)$. The target error is $[\delta y_f, \delta \dot{x}_f, \delta \dot{z}_f]^T$ and the design error is $[\delta \dot{y}_0, \delta t_f, \delta z_0]^T$. They are linked by the relationship:

$$\begin{bmatrix} \delta \dot{y}_0 \\ \delta t_f \\ \delta z_0 \end{bmatrix} = \begin{bmatrix} \mathbf{\Phi_{2,5}} & \dot{y}(t_f) & \mathbf{\Phi_{2,3}} \\ \mathbf{\Phi_{4,5}} & \ddot{x}(t_f) & \mathbf{\Phi_{4,3}} \\ \mathbf{\Phi_{6,5}} & \ddot{z}(t_f) & \mathbf{\Phi_{6,3}} \end{bmatrix}^{-1} \begin{bmatrix} \delta y_f \\ \delta \dot{x}_f \\ \delta \dot{z}_f \end{bmatrix} \tag{2.77}$$

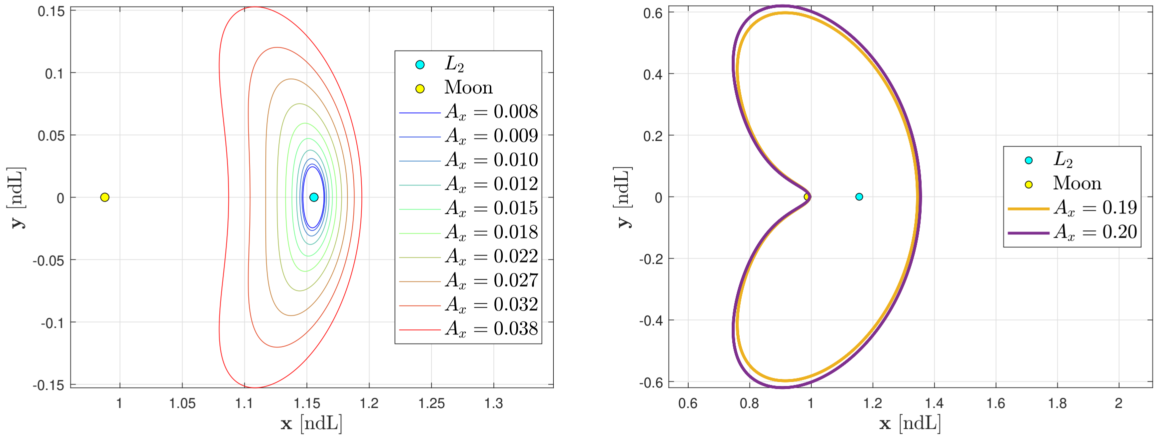

(a) (b)

Figure 2.9: Examples of planar Lyapunov orbit generation by continuous method. The value of A_x given refers to the distance between $L2$ and the intersection on the x-axis with $x > L2$.

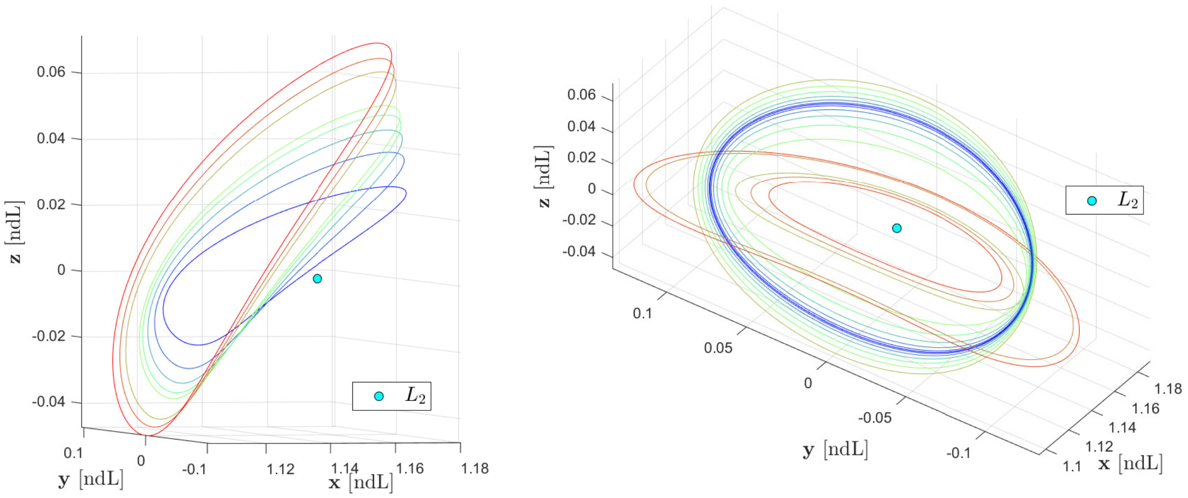

(a) (b)

Figure 2.10: Examples of halo orbit generation by continuation method. On the left, the method was applied as already described in Fig. [2.9], but to halo orbits. On the right, it can be seen how the method allows to detect bifurcations between families.

2.8. Stable/Unstable manifolds computation

CR3BP's phase-space analysis demonstrates the existence of invariant structures that bring order to chaos and enable design activity. These structures stand in place of the R2BP's conical orbits, they are of complex analytical treatment and require a numerical approach: These structures are the Space Manifolds, classified into stable, unstable and central.

Figure **[2.11]** shows an example of how the stable and the unstable manifolds associated with a given periodic orbit can intersect in the Earth-Moon system. The figure allows some considerations:

- The trajectories are obtained after a ϵ perturbation of just 38.4 km in position. Yet this slight deviation from periodic orbit results in an escape from the equilibrium region towards Earth domain or the Interplanetary Space. This is an example of hyperbolic varieties.
- The hyperbolic varieties associated with Earth-Moon L1, L2 do not reach the most massive primary.

A general way to compute an initial condition on a given hyperbolic manifold associated with a given periodic orbit is to apply a displacement from a given point on the periodic orbit, say $\mathbf{x_{p.o.}}$, along the stable/unstable eigendirection. To this end, we need to compute the monodromy matrix associated with the given point and the corresponding eigenvalues and eigenvectors. Let $\lambda_1 > 1$ the eigenvalue associated with the unstable direction $\mathbf{e_1}$, and $\lambda_2 = 1/\lambda_1$ the one associated with the stable direction $\mathbf{e_2}$. So, the initial conditions on the stable and unstable manifold are given, respectively, by:

$$\begin{aligned} \mathbf{x_0^u} &= \mathbf{x_{p.o.}} \pm \epsilon \mathbf{e_1} \\ \mathbf{x_0^s} &= \mathbf{x_{p.o.}} \pm \epsilon \mathbf{e_2} \end{aligned} \tag{2.78}$$

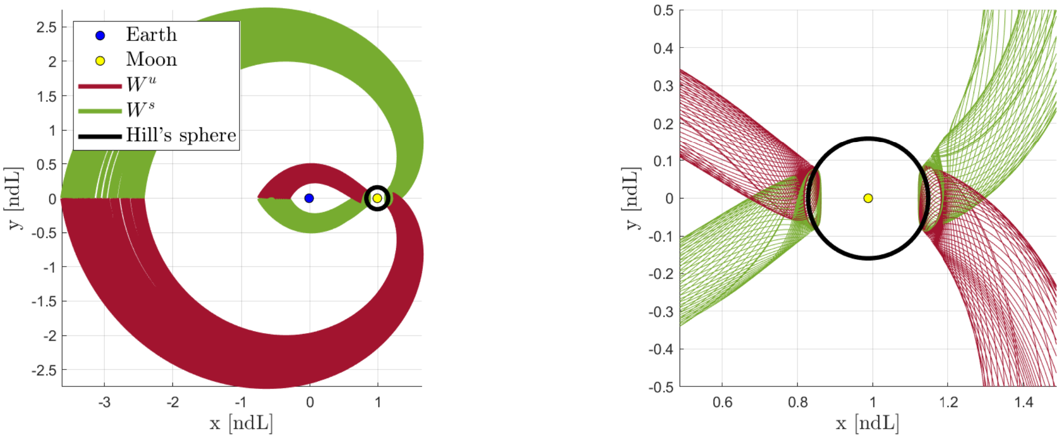

(a) (b)

Figure 2.11: Space Manifolds Structure Earth-Moon System. Overview on the left and detailed on the right. In green the Stable Manifolds $W^{s,\oplus}_{L1}$, $W^{s,\chi}_{L2}$ towards the EML$_{1,2}$ from Earth and interplanetary space. In red the Unstable Manifolds $W^{u,\oplus}_{L1}$, $W^{u,\chi}_{L2}$ from EML$_{1,2}$ to Earth and interplanetary space. In black the Moon Hill's sphere. The figure is obtained with $\mu_M = 0.0121505856$, Lyapunov's orbit initial state [0.8189; 0; 0; 0; 0.17454; 0] and [1.1809; 0; 0; 0; -0.15587; 0]. The Manifolds are obtained introducing a perturbation of $\epsilon = 38.4$ km along the local manifold of periodic orbit.

where ϵ is a small displacement, defined to ensure the accuracy of the linear approximation.

- Recall that the stable manifolds must be integrated backward in time while the unstable forward.
- The stable and the unstable manifolds are characterized by two branches.

A Manifold 'W' has subscript 'Li' for the Lagrangian point of periodic orbit from/to which it moves, apex 's' when stable or 'u' if unstable, followed by apex of domain of the celestial body to which it belongs. In this thesis $\oplus$ stands for Earth, $\bigcirc$ for Moon, $\odot$ for Sun, χ for Interplanetary Space. Overall, in the Sun-Earth+Moon system there are:

$$W^{s,\odot}_{L1} \text{ s.t. } \mathbf{x_0^s} = \mathbf{x_{p.o.}} - \epsilon \mathbf{e_2} \qquad \text{p.o. about L1}$$

$$W^{u,\odot}_{L1} \text{ s.t. } \mathbf{x_0^u} = \mathbf{x_{p.o.}} - \epsilon \mathbf{e_1} \qquad \text{p.o. about L1}$$

$$W^{s,\oplus}_{L1} \text{ s.t. } \mathbf{x_0^s} = \mathbf{x_{p.o.}} + \epsilon \mathbf{e_2} \qquad \text{p.o. about L1}$$

$$W^{u,\oplus}_{L1} \text{ s.t. } \mathbf{x_0^u} = \mathbf{x_{p.o.}} + \epsilon \mathbf{e_1} \qquad \text{p.o. about L1}$$

$$W_{L2}^{s,\oplus} \text{ s.t. } \mathbf{x_0^s} = \mathbf{x_{p.o.}} - \epsilon \mathbf{e_2} \qquad \text{p.o. about L2}$$

$$W_{L2}^{u,\oplus} \text{ s.t. } \mathbf{x_0^u} = \mathbf{x_{p.o.}} - \epsilon \mathbf{e_1} \qquad \text{p.o. about L2}$$

$$W_{L2}^{s,\chi} \text{ s.t. } \mathbf{x_0^s} = \mathbf{x_{p.o.}} + \epsilon \mathbf{e_2} \qquad \text{p.o. about L2}$$

$$W_{L2}^{u,\chi} \text{ s.t. } \mathbf{x_0^u} = \mathbf{x_{p.o.}} + \epsilon \mathbf{e_1} \qquad \text{p.o. about L2}$$

Take care that for each point on the orbit the eigenvectors $\mathbf{e_1}, \mathbf{e_2}$ are not the same, so they must be newly calculated.

3 | Parametric transfer design to LPOs

3.1. Introduction

In this chapter, we describe how a transfer trajectory from a given parking orbit at the Earth to a nominal halo orbit in the Sun-Earth system can be designed. It is adopted the acronym Transfer Trajectory Insertion (TTI) for the impulsive maneuver required to insert into the transfer trajectory, while the maneuver to move from the transfer trajectory to the halo orbit is called halo Orbit Insertion (HOI). In the general case, the latter is referred as Periodic Orbit Insertion (POI).

If the transfer trajectory is a stable invariant manifold, then the Δv_{HOI} is zero, or almost negligible, by definition.

The targeting is an Initial Value 2-points Boundary Value Problem. Which states on the initial and final orbits shall we consider to depart and arrive? In the same way, how define the transfer time?

In order to overcome these issues, in this chapter main attention is drawn on exploiting the hyperbolic manifolds associated with a given halo orbit. In this way, feasible solutions can be systematically uncovered and represented to get a picture of their behaviour and a region of interest. The result is the selection of a reference trajectory, with terminals TTI and HOI, based on feasibility and performance criteria. It's not a local optimum, but a very good guess.

Once the baseline is sketched and it's enforced a educated initial guess, it's can be further optimized by a pure numerical technique. Let's recall that optimization techniques guarantee high accuracy and they allow to deal with high-fidelity models, real constraints, low-propulsion, targeting and station-keeping. In the previous chapter, the differential correction algorithm was described and applied to compute planar Lyapunov and halo orbits. In this chapter the differential correction is enforced to simple shooting.

All the following results are based on the CR3BP model, assuming to exploit the hyperbolic manifolds and an impulsive propulsion. Unless otherwise indicated, this thesis operates in the Sun-Earth+Moon system (SE$^+$)[1] in the synodic reference system centered at the barycenter of the primaries.

$$
\begin{aligned}
m_*^+ &= m_S + m_E + m_M && \text{with } \; m_S: \text{ Sun mass [kg]} \\
\mu_1 &= G_* \, \frac{m_E + m_M}{m_*^+} && m_E: \text{ Earth mass [kg]} \\
\mu_2 &= G_* \, \frac{m_M}{m_*^+} && m_M: \text{ Moon mass [kg]} \\
\mu_E &= \mu_1 - \mu_2
\end{aligned}
$$

The Table [**3.1**] lists the system parameters computed by means of NASA JPL[2] and NSSDC[3] databases. In SE$^+$ CR3BP the Earth+Moon subsystem is modelled as a single celestial body of barycentric mass μ_1 and location (1-μ_1,0,0). The constant μ_E in the Table is used to model a parking orbit around the Earth in the R2BP. Last but not least, the chapter assumes impulsive thrust.

---

[1] Except to this paragraph, the '+' will be omitted to simplify the notation.

[2] `https://ssd.jpl.nasa.gov/astro_par.html`

[3] `https://nssdc.gsfc.nasa.gov/planetary/factsheet/moonfact.html`

Table 3.1: Sun-Earth+Moon system

μ_1	SE$^+$ mass parameter	$3.040423405293360 \times 10^{-6}$	ndL^3/ndT^2
μ_E	SE$^+$ Earth	$3.003480484111692 \times 10^{-6}$	ndL^3/ndT^2
μ_2	SE$^+$ Moon	$3.694292118166765 \times 10^{-8}$	ndL^3/ndT^2
l_*	length factor	$1.495978707000000 \times 10^{8}$	km
t_*	time factor	$5.022635255879730 \times 10^{6}$	s
v_*	velocity factor	29.784737110837138	km/s
m_*^+	mass factor	$1.988415916594034 \times 10^{30}$	kg
x_{L1}	SE$^+$L1	0.989985982341322	ndL
x_{L2}	SE$^+$L2	1.01007520002418	ndL
x_{L3}	SE$^+$L3	-1.00000126684309	ndL

Main References: The main references for this chapter are Koon et al. [2011], Canalias Vila [2007], Soldini [2016], Doedel et al. [2007], Canalias et al. [2004], Rausch [2005], Bernelli et al. [2004], Betts [2010]. Additional references are given inside.

Chapter Outline: This chapter intended to explore and describe the transfer trajectory design within the CR3BP model. A budget baseline from LEO and GTO orbits is estimated and extended to Ariane launcher. The baseline is also used to search for additional and more optimal solutions by means of sampling and targeting. Finally, it is estimated the additional cost required to orientate the parking orbit before launching.

3.2. Baseline

Recall the assumptions: the analysis is performed in the Sun-Earth+Moon rotating reference system; the Earth location is assumed the same of Earth+Moon barycentre $(1-\mu_1, 0, 0)$; only for the parking orbit it's used as mass parameter μ_E in Table **[3.1]**; last but not least, the propulsion is impulsive and the maneuver a simple shooting.

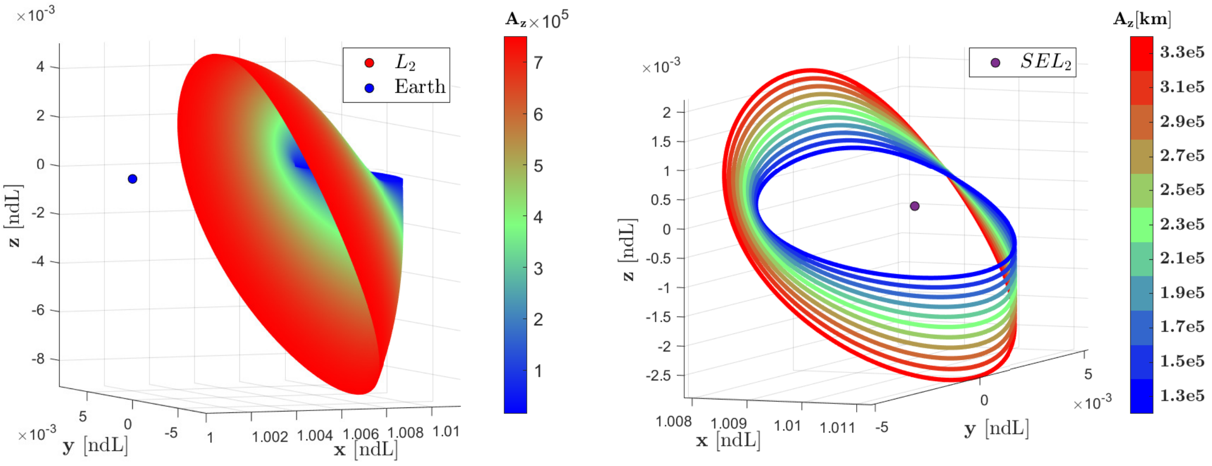

(a) (b)

Figure 3.1: Southern SEL2 Halo orbits. On the left the full family between 15,000 and 750,000 km A_z amplitude. At the right same sample.

This analysis is performed backward from the given halo to the given Earth parking orbit. The halo orbits are generated by Lyapunov bifurcation with a differential correction method (Fig. **[3.1]**). The transfer is established on the stable manifold of the given halo orbit.

The stable manifolds are integrated backward for about 4 months until the selected Poincaré section is reached. The semiplane $(y = 0) \wedge (x < 1 - \mu_1)$ shown in Fig. **[3.2]** is investigated. According to Barden [1994] it offers a good compromise between transfer time and cost, for Bernelli et al. [2004] on this section the manifolds are closer to Earth and almost normal to semiplane.

On the Poincaré section, the state $(\mathbf{s}, \mathbf{v}) = (x, y, z, v_x, v_y, v_z)$ of the outgoing manifold is known. We redefine this state in terms of spherical coordinates, namely, altitude h, longitude α, latitude $\Delta\iota_z$, assuming as reference plane the ecliptic plane.

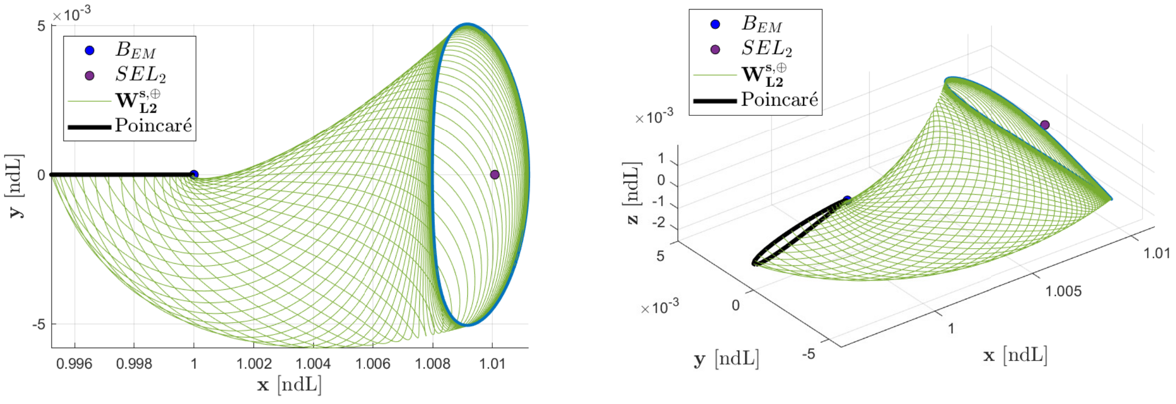

(a) (b)

Figure 3.2: Stable manifolds $W^{s,\oplus}_{L2}$ propagated backward from the SEL2-halo orbit A_z 290,000 km amplitude to semiplane $(y = 0) \wedge (x < 1 - \mu_1)$. B_{EM} is the barycentre of Earth-Moon system.

Given μ_1, with respect to Earth+Moon barycentre the TTI radius $\mathbf{r}$ location is:

$$\mathbf{r} = (x - 1 + \mu_1, y, z)^T \tag{3.1}$$

The altitude of TTI is obtained just subtracting the Earth radius (6371 km) to $||\mathbf{r}||$. The spherical angles latitude $\Delta\iota_z$ and longitude α are computed by geometrical relation:

$$\begin{aligned} \Delta\iota_z &= \arctan\left(\frac{r_z}{\sqrt{r_x^2 + r_y^2}}\right) \\ \alpha &= \arctan\left(\frac{r_y}{r_x}\right) \end{aligned} \tag{3.2}$$

Remarks:

- α is always π in the selected Poincaré section.
- The manifold latitude $\Delta\iota_z$ plays a role as launcher requirement.

In Fig. **[3.2]** is draft the manifolds trace in terms of latitude $\Delta\iota_z$ and altitude h. Looking at the trace on the Poincaré section, the manifold to A_z 20,000 km halo has minimum altitude at about 6,300 km. The manifold minimum altitude decrease as halo amplitude

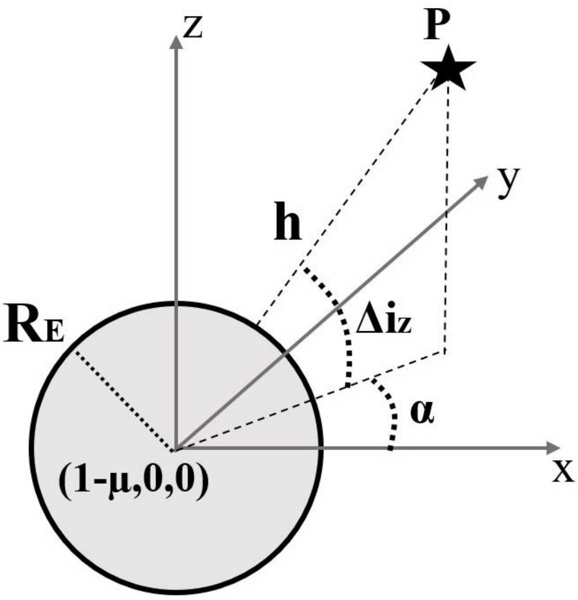

(a)

Figure 3.3: Sketch of the spherical coordinates respect to Earth. Altitude h, longitude α respect to x-axis of the synodic frame, ecliptic latitude $\Delta\iota_z$.

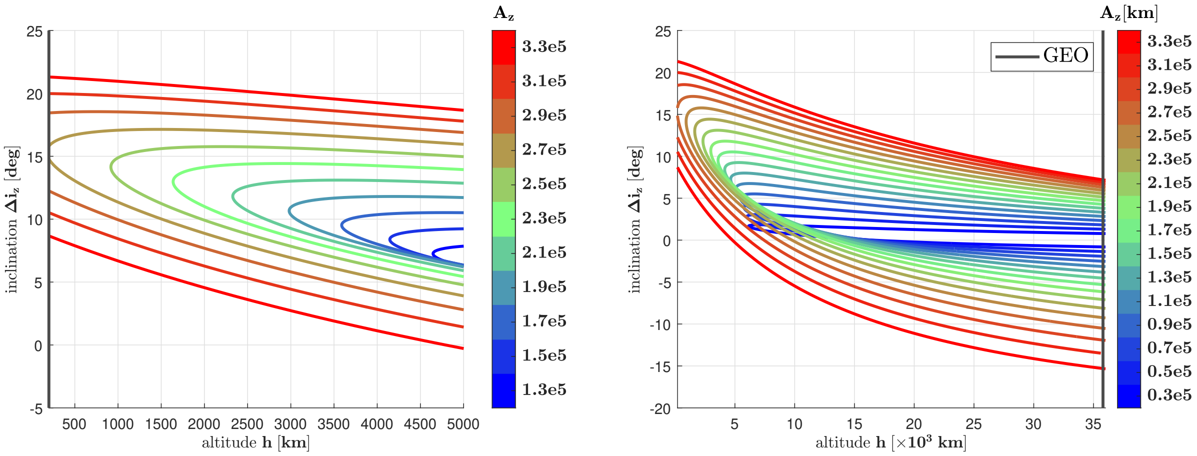

(a) (b)

Figure 3.4: $\Delta\iota_z$ latitude wrt ecliptic plane versus h altitude of the parameterized halo orbits in the semiplane $(y = 0) \wedge (x < 1 - \mu_1)$. On the left the lower altitude band $200 < h < 5,000$ km and halo A_z amplitude between 130,000 km and 330,000 km. On the right $200 < h < 36,000$ km and halo A_z amplitude between 30,000 and 330,000 km. The grey line indicates the GEO altitude.

increase, such that the manifold to A_z 270,000 km halo has around 200 km minimum altitude. Then, the manifolds collides onto the Earth.

According to these considerations, on the Poincaré section there exist two sets of interest in altitude. The first is between 200 and 5,000 km, the second is between 5,000 and 36,000 km altitude. In the lower band the halo family is parameterized between 130,000 and 330,000 km A_z. While in the upper band amplitudes between 30,000 and 330,000 km are used.

Once the manifolds trace on the Poincaré section is obtained, the TTI points must be patched to the parking orbit. In the lower altitude band a transfer from the LEO region and the GTO pericenter can be investigated. In the upper band the departure from apocenter of an elliptic orbit is considered.

The selection of the parking orbit leads to insertion budget Δv_{TTI} to the stable manifold. However, to compare all the trajectories an additional step must be included. As a simplified approach it is considered a reference orbit, a LEO at 200 km altitude coplanar to the parking orbit. Then, it is computed the Δv to reach the parking orbit from the reference orbit. The proposed simplified approach is not of course an optimal trajectory solution, but at least gives a conservative way to compare all the manifold trajectories with respect to the same reference orbit.

LEO

For altitude lower than 5,000 km let's assume that the parking orbit is circular. It is also supposed that the parking orbit belong to manifold plane i.e., they have the same inclination[4].

---

[4] Any costs for reorienting the parking orbit are estimated separately.

Table 3.2: Insertion from Circular Parking Orbit

A_z [km]	h [km]	Δv_{TTI} [km/s]	$\Delta\iota_z$ [deg]	Δt [days]
130,000	4956.6	2.53	7.83	125.96
150,000	4989.9	2.49	9.24	126.17
170,000	4948.6	2.48	10.52	126.43
190,000	4988.3	2.46	11.72	126.73
210,000	4981.7	2.46	12.86	127.07
230,000	4876.5	2.49	13.98	127.44
250,000	4974.1	2.50	14.98	127.86
270,000	4946.0	2.54	15.98	128.32
290,000	4954.3	2.59	16.91	128.82
310,000	4765.0	2.68	17.92	129.36
330,000	4831.8	2.74	18.76	129.96

The momentum versor $\hat{\mathbf{m}}$ defines the normal direction:

$$\hat{\mathbf{m}} = \frac{\mathbf{r} \times \mathbf{v}}{||\mathbf{r}||\ ||\mathbf{v}||} \tag{3.3}$$

Such that the velocity versor is:

$$\hat{\mathbf{v}}_{\mathbf{pk}} = \frac{\hat{\mathbf{m}} \times \mathbf{r}}{||\mathbf{r}||} \tag{3.4}$$

From the R2BP the parking orbit velocity magnitude is:

$$v_{pk} = \sqrt{\frac{\mu_E}{r}} \tag{3.5}$$

Finally, the transfer trajectory insertion cost is computed as:

$$\Delta v_{TTI} = ||\mathbf{v} - \mathbf{v}_{\mathbf{pk}}|| \tag{3.6}$$

In Tab. **[3.2]** we show some examples. For each amplitude of the halo orbit the table shows at the insertion altitude h the insertion cost Δv_{TTI}, the latitude $\Delta\iota_z$ and the transfer time Δt.

Figure **[3.5]** reports on the left the insertion cost. Note that the on-board propulsion system requirement decreases with altitude. However, a higher parking orbit is used. In order to make the solutions comparable, on the right the Hohmann transfer cost from a 200 km LEO to the insertion altitude is provided. As known, the Hohmann transfer is the sum of two contribution:

$$\Delta v_1 = \sqrt{\frac{\mu_E}{r_p}}\left(\sqrt{\frac{2r_a}{r_p + r_a}} - 1\right) \tag{3.7}$$

$$\Delta v_2 = \sqrt{\frac{\mu_E}{r_a}}\left(1 - \sqrt{\frac{2r_p}{r_p + r_a}}\right) \tag{3.8}$$

$$\Delta v_H = \Delta v_1 + \Delta v_2 \tag{3.9}$$

- Δv_1 could be provided by the launcher, so eventually only Δv_2 must be held on-board.
- The resulting on-board requirement $\Delta v_2 + \Delta v_{TTI}$ is about 3.2 km/s to 200 km altitude.
- The total cost $\Delta v_H + \Delta v_{TTI}$ is increasing with altitude since Δv_H is growing faster than Δv_{TTI} decreasing.

Finally, if the altitude is lower then 2,000 km the circular orbit is a LEO. In Fig. **[3.6]** we show some examples of transfers, while in Tab. **[3.3]** the corresponding cost.

GTO pericenter

At altitude lower than 500 km, the insertion can correspond to the pericenter of a GTO. The direction of the GTO velocity at the pericenter is the same as a LEO at the same altitude, as defined in Eq. [3.4]. Also, once fixed the apocenter to the GEO altitude the velocity magnitude in the pericenter is:

$$v_p = \sqrt{\frac{\mu_E}{r_p}}\sqrt{\frac{2r_a}{r_p + r_a}} \tag{3.10}$$

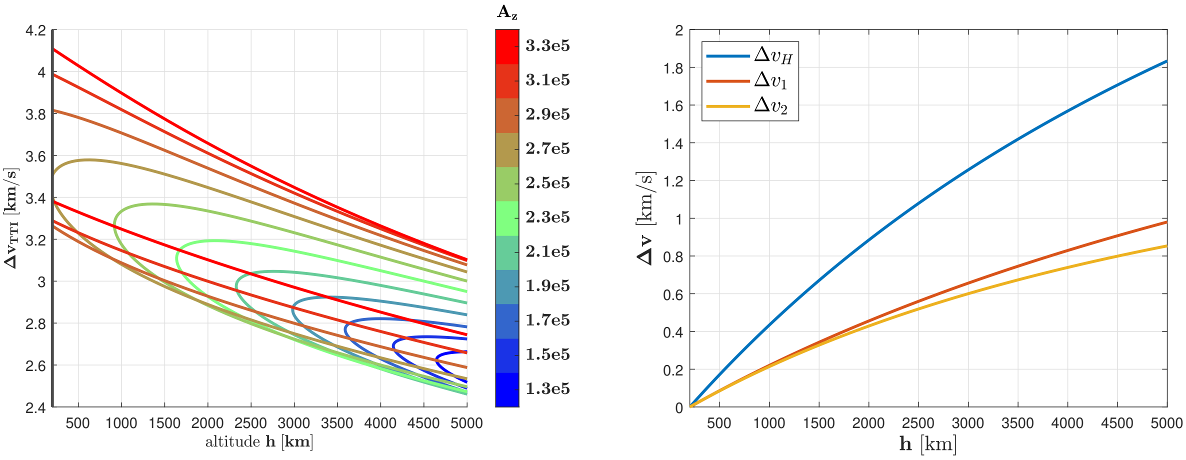

(a) (b)

Figure 3.5: Δv budget to transfer from a parking orbit at the Earth to a SEL2-halo. The parking orbit is circular, perfectly inclined. On the left the insertion cost, on the right the Hohmann transfer cost from a LEO of 200 km of altitude.

Table 3.3: Insertion from LEO

A_z [km]	h [km]	Δv_{TTI} [km/s]	$\Delta\iota_z$ [deg]	Δt [days]
230,000	1960.6	2.94	14.09	127.30
250,000	1941.9	2.90	15.75	127.71
270,000	1959.7	2.90	17.09	128.16
290,000	1900.8	2.94	18.31	128.66
310,000	1956.4	3.01	19.40	129.21
330,000	1941.9	3.11	20.46	129.80
270,000	476.6	3.24	16.67	128.09
280,000	460.5	3.21	17.69	128.33
290,000	495.7	3.19	18.53	128.58
300,000	417.0	3.22	19.27	128.84
310,000	498.8	3.23	19.94	129.13
320,000	377.4	3.30	20.61	129.41
330,000	419.4	3.34	21.22	129.71

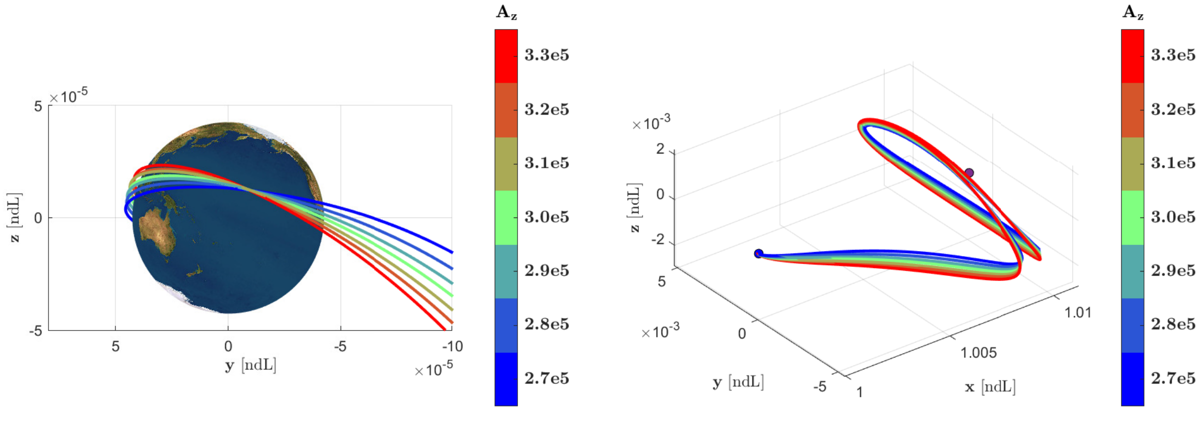

(a) (b)

Figure 3.6: Transfer trajectory from a LEO to a SEL2-halo. On the left the insertion onto the manifold, on the right the whole transfer.

In Tab. **[3.4]** and in Fig. **[3.7]** on the left the insertion cost is reported. On the right of the same figure the contribution Δv_L to inject into the GTO.

- The insertion cost Δv_{TTI} is 0.81 km/s. Clearly, the on-board requirement is much lower than 3.2 km/s from LEO.
- In this case the overall cost is obtained by adding three contributions: (1) the Hohmann manoeuvre Δv_H from LEO 200 km altitude to a circular orbit to insertion altitude h; (2) the budget Δv_L to move from the circular orbit to GTO; (3) finally the insertion cost Δv_{TTI} from the GTO to the manifold.

The overall cost from a GTO pericentre is approximately the same than from a LEO. However, if contributions $\Delta v_H + \Delta v_L$ are provided by the launch service, then the on-board requirement Δv_{TTI} is low demanding.

GTO apocenter

Transfers from LEO and GTO pericenter exploit only low altitude stable manifolds. Now the analysis assumes a transfer from the apocenter, in this way upper altitude manifolds can be investigated.

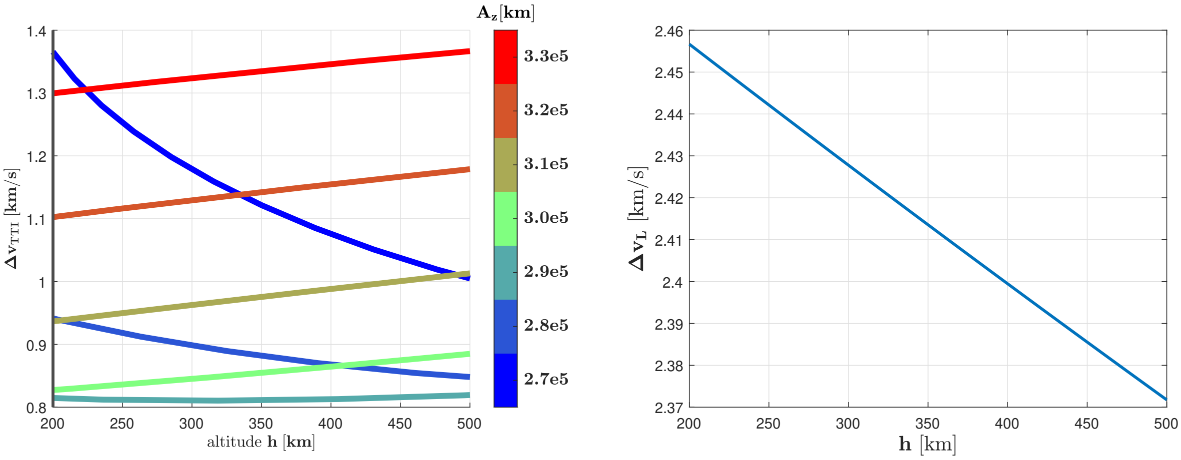

(a) (b)

Figure 3.7: Δv budget to transfer from a parking orbit at the Earth to a SEL2-halo. The parking orbit is a GTO perfectly oriented. On the left is the cost of injection into the manifold at altitude h, on the right the contribution for injection into the GTO from a LEO at the same altitude h. The altitude is between 200 and 500 km, the halo amplitude between 270,000 and 330,000 km.

Table 3.4: Insertion from GTO pericenter

A_z [km]	h [km]	Δv_{TTI} [km/s]	$\Delta \iota_z$ [deg]	Δt [days]
270,000	476.6	1.02	16.67	128.09
280,000	460.5	0.85	17.69	128.33
290,000	318.8	0.81	18.49	128.57
300,000	213.6	0.83	19.26	128.83
310,000	259.6	0.95	19.98	129.11
320,000	245.8	1.12	20.65	129.40
330,000	273.3	1.32	21.28	129.71

It's considered an elliptic trajectory, with pericenter at 200 km altitude and the apocenter at TTI altitude. The total cost is the sum of launcher contribution and the insertion cost. Clearly, the launcher service cost increase with the TTI altitude. The insertion cost is again obtained by vectorial difference betweeen the incoming elliptic parking orbit and the outgoing manifold. Since the TTI is at apocenter, the parking orbit velocity direction is always given by Eq. [3.4]. The magnitude of the velocity at apocenter is computed as:

$$v_a = \sqrt{\frac{\mu_E}{r_a}} \sqrt{\frac{2r_p}{r_p + r_a}} \tag{3.11}$$

In Fig. **[3.8]** on the left the insertion cost, on the right the launcher contribution Δv_L. As expected, at 200 km altitude the insertion cost is the same as from LEO. Above the 5,000 km altitude the on-board requirement begins to drop. Note that when the apocenter is at GEO altitude, the elliptic orbit is a GTO. In such a case, the Δv_{TTI} is about 2.7 km/s. However, at the same altitude the launcher contribution Δv_L is bit less than 2.5 km/s. So the total cost $\Delta v_L + \Delta v_{TTI}$ is 5.2 km/s. Once again, using GTO the on-board requirement decreases, but it is not the case for the total cost.

Summarizing, although the Δv_{TTI} decreases with altitude, the overall effect results in a loss. Barring additional costs related to orientation, the best performing insertion point to a manifolds is presumably not far from his minimum altitude from Earth, hence the poor performance of an insertion from an apocenter.

3.2.1. Ariane GTO pericenter

The aim of this section is to provide an estimation of Δv-budget from the GTO pericenter that Ariane can provide to get to a SEL2-halo. The Ariane Launcher User manual provides the data relatives to GTO in Tab. **[3.5]** where: i is the GTO inclination; Ω_k the longitude of Right Ascension of Ascending Node (RAAN) respect to the Kourou Meridian;

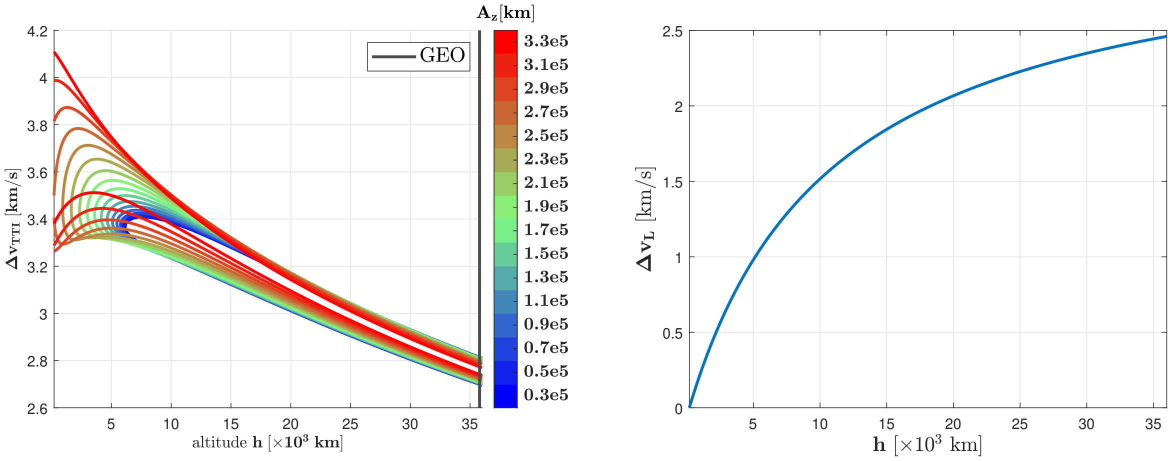

(a) (b)

Figure 3.8: Δv budget to transfer from a parking orbit at the Earth to a SEL2-Halo. The parking orbit is an elliptic orbit with apocenter at manifold insertion altitude h, perfectly inclined. On the left the insertion cost, on the opposite side the launcher contribution for the injection in the elliptic orbit from LEO 200 km altitude orbit. The grey line indicates the GEO altitude. Altitude h is between 200 and 36,000 km, the halos have amplitude A_z between 30,000 and 330,000 km.

Table 3.5: GTO Ariane

i	6	[deg]
Ω_k	-120	[deg]
z_p	250	[km]
z_a	35,943	[km]
ω	178	[deg]
λ_k	-52.761	[deg]
φ_k	5.238	[deg]
d_{sid}	23.934	[h]
y_{sid}	366.2564	[d_{sid}]

z_p, z_a the GTO altitude of pericenter and apocenter. In the same table they are reported: λ_k, φ_k longitude and latitude of Kourou Spaceport; d_{sid}, y_{sid} sidereal day and year.

The launch windows for GTO are daily, they last 45 minutes, and they start at the beginning of the s/c injection window. In Tab. **[3.6]** the standard time window at the first perigee passage in the User Manual. By interpolation is obtained the daily time window.

In this analysis it is assumed that the GTO pericenter occurs in the middle of the daily time window ($t_{day,LW}$). In addiction, it's assumed known the vernal equinox. For instance,

Table 3.6: GTO Ariane Standard Launch Window at first perigee passage

Day	LW opening [UT]	LW closure [UT]
1	22:29	23:14
10	22:33	23:18
20	22:37	23:22
30	22:39	23:24
40	22:40	23:25
50	22:39	23:24
60	22:37	23:22
70	22:33	23:18
80	22:28	23:13
90	22:23	23:08
100	22:17	23:02
110	22:12	22:57
120	22:08	22:53
130	22:04	22:49
140	22:01	22:46
150	22:00	22:45
160	22:01	22:46
170	22:02	22:47
180	22:05	22:50
190	22:08	22:53
200	22:11	22:56
210	22:14	22:59
220	22:16	23:01
230	22:17	23:02
240	22:17	23:02
250	22:17	23:02
260	22:15	23:00
270	22:14	22:59
280	22:12	22:57
290	22:10	22:55
300	22:09	22:54
310	22:09	22:54
320	22:11	22:56
330	22:13	22:58
340	22:17	23:02
350	22:21	23:06
360	22:26	23:11

2023 isn't a leap year and the vernal equinox is at 3:06 of 20 March ($GMT_{ver,year}$).

Then, the GTO RAAN at vernal equinox day $\Omega_{0,year}$ for the year is computed:

$$\begin{aligned}
&\Delta t_{ver,year} = t_{ver,LW} - GMT_{ver,year}\\
&GHA_{ver,year} = GMT_{ver,year} - 12\\
&\lambda_k = \lambda_k \frac{d_{sid}}{360}\\
&LHA_{ver,year} = GHA_{ver,year} + \lambda_k\\
&LHA_{0,year} = LHA_{ver,year} + \Delta t_{ver,year}\\
&\Omega_{0,year} = \Omega_k \frac{\pi}{180} \frac{d_{sid}}{2\pi} + LHA_{0,year}
\end{aligned} \tag{3.12}$$

where:

- $t_{ver,LW}$ is $t_{day,LW}$ the vernal day;
- $GHA_{ver,year}$ is the Greenwich hour time at vernal equinox;
- $LHA_{ver,year}$ is the Local Hour Angle at vernal equinox at the Kourou Spaceport;
- $LHA_{0,year}$ is the Local Hour Angle at the Kourou Spaceport when the s/c is at the first GTO pericenter;

Once the RAAN corresponding to the vernal day is known, it's immediate to obtain the RAAN for each day of the solar year simply considering the difference between $t_{day,LW}$ and $t_{ver,LW}$ in sidereal days.

Given the Keplerian elements, the pericenter state vector can be computed in the Earth Centred Equatorial Inertial reference system and converted in the dimensionless Sun-Earth+Moon rotating reference system $(\mathbf{r_p}, \mathbf{v_p})$ centred in the Earth+Moon barycentre.

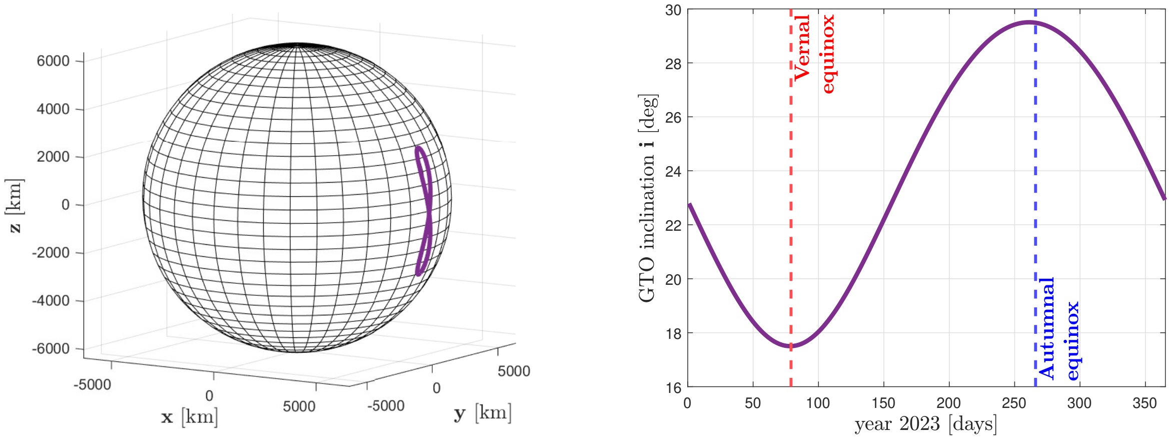

(a) (b)

Figure 3.9: Ariane GTO parking orbit in the Sun-Earth+Moon rotating frame. Locus of pericenter on the left and orbit inclination on the right.

In Fig. **[3.9]** the locus of pericentres and the orbit inclination computed by:

$$i = \arccos\left(\frac{\mathbf{r_p} \times \mathbf{v_p}}{||\mathbf{r_p}||\ ||\mathbf{v_p}||} \bullet \hat{\mathbf{k}}\right) \tag{3.13}$$

In Fig. **[3.10]** the longitude α and latitude i_z of pericenter according to Eq. **[3.2]**.

Note that:

- the orbit inclination ranges between 17.5 [deg] at vernal equinox and 29.5 [deg] at autumnal equinox;
- pericenter longitude onto the ecliptic plane is bounded between -4.5 and 0.5 [deg];
- pericenter latitude respect to the ecliptic plane lies between -23.3 and 23.7 [deg];

In order to estimate the Δv from Ariane GTO pericenter it can be applied the same approach seen so far, by selecting a suitable Poincaré section. We choose $(y = 0) \wedge (x > 1 - \mu_1)$. In Fig. **[3.11]** the stable manifold and their trace on the Poincaré section are shown. Multiple passage have been considered until stable manifolds approach the Earth, for this reason the transfer time is about 8.4 months. In Fig. **[3.12]** is shown the insertion

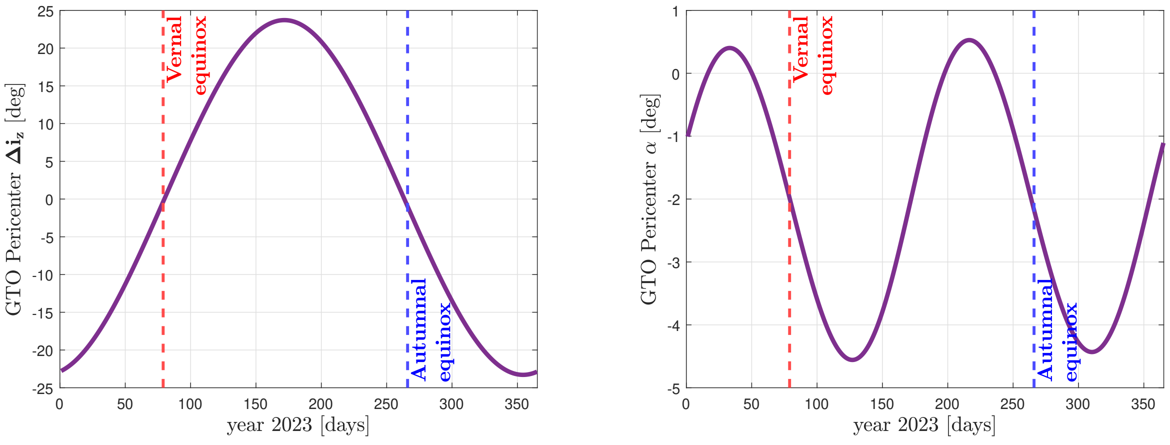

(a) (b)

Figure 3.10: Ariane GTO parking orbit spherical coordinates in Earth centred synodic reference system. Pericenter latitude at left and longitude on the right.

cost: approximately 0.804 km/s from GTO and 3.25 km/s from LEO. Note that the cost is comparable to the result already found at section $(y = 0) \wedge (x < 1 - \mu_1)$, what changes is the amplitude of the targeted halo orbit and the transfer time.

3.3. Sample Approach

In this section, a Δv_{TTI} sample survey from parking orbit to halo is proposed without imposing a Poincaré section. Let us consider a pool of stable manifolds to same halo. The algorithm computes the transfer budget for each sample in the pool and provides the minimum. It's a pure numerical method exploiting manifolds and working backward:

- The set of halos considered have A_z amplitude between 20,000 km and 500,000 km with step 10,000 km. For each halo 3600 HOI with ϵ 6,500 km are sampled[5].
- Then the stable manifolds are propagated backward for one year time span. The integration stops if the s/c collides on Earth or escapes in the interplanetary space.

---

[5] According to Barden [1994] in Sun-Earth system a ϵ between 200 and 9,000 km can be selected, depending on station keeping requirements.

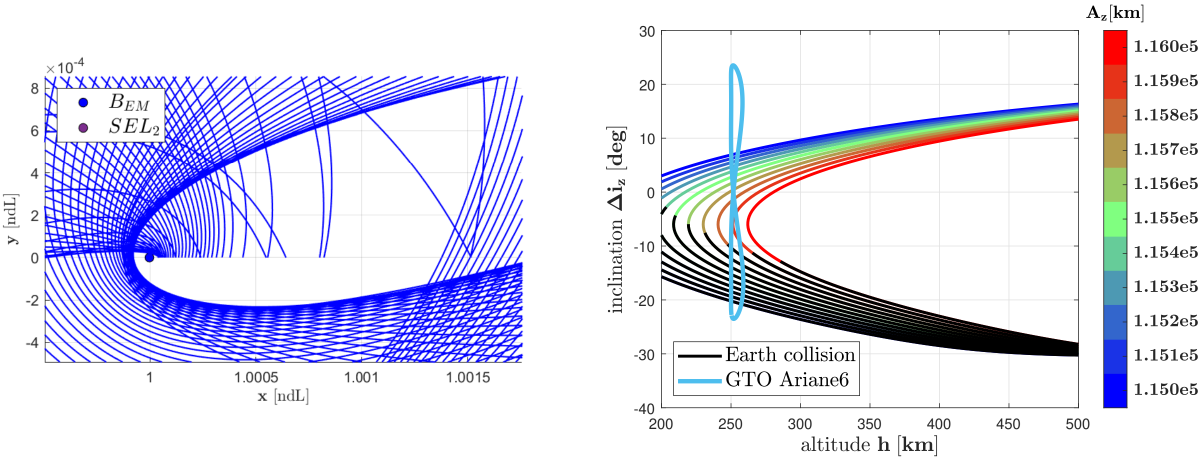

(a) (b)

Figure 3.11: Stable manifold trajectories approaching the Earth projected onto Poincaré section $(y = 0) \wedge (x > 1 - \mu_1)$. On the left stable manifolds to SEL2-halo A_z 115,000 km. On the right the traces onto the Poincaré section of manifolds to halos and of Ariane GTO. Halo orbits parameterized between 115,000 and 116,000 km. In black the trajectories impacting the Earth.

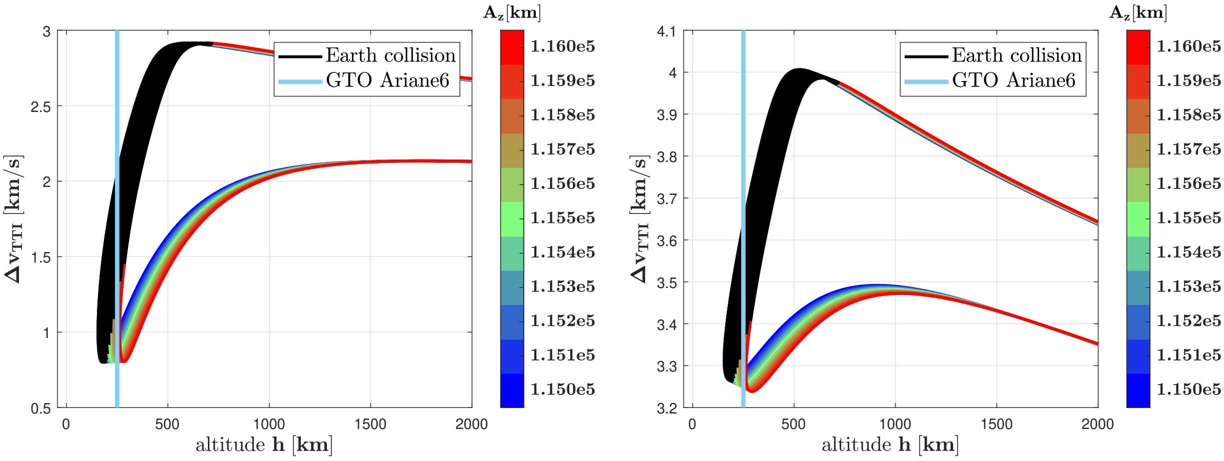

(a) (b)

Figure 3.12: Δv budget from Earth to SEL2-Halo. On the left the parking orbit is a GTO perfectly inclined with pericenter on the Poincaré section $(y = 0) \wedge (x > 1 - \mu_1)$ and TTI altitude h. On the right the parking orbit is a LEO, perfectly inclined on the same Poincaré section and TTI altitude.

- Furthermore, during the propagation some no-stop events are checked: transitions for Poincaré planes $x = 1-\mu_1$ or $y = 0$; perpendicularity between location respect to the Earth and velocity. The first check allows the algorithm to cover the solutions obtained in the previous analysis, as well as some in the literature review. The second check is used to detect manifolds perigee occurrences.
- Any times the manifolds approach the Earth to an altitude compatible with the parking orbit the $\mathbf{\Delta v_{TTI}}$ is computed by vectorial difference.
- For each halo A_z, the minimum $||\mathbf{\Delta v_{TTI}}||$ obtained is considered optimal, its trajectory is plotted and solution is tabled.

The parking orbit can be a GTO or a LEO.

3.3.1. Efficient low-cost Δv_{TTI} from GTO

GTO is modelled with perigee altitude 200 km and perfectly oriented, such that knowing the pericenter r_p, the apocenter r_a, the manifold state $(\mathbf{r}, \mathbf{v})$ with $r_p \leq ||\mathbf{r}|| \leq r_a$:

$$e = \frac{r_a - r_p}{r_a + r_p}$$

$$a = \frac{r_a + r_p}{2}$$

$$\theta = \arccos\left[\frac{a(1-e^2)}{e||\mathbf{r}||} - \frac{1}{e}\right] \text{ s.t. } \begin{cases} \theta \in [0, \pi] & \text{, if } \mathbf{r} \bullet \mathbf{v} \geq \mathbf{0} \\ \theta \in [0, -\pi] & \text{, otherwise} \end{cases}$$

$$v_{pk} = \sqrt{\mu_E\left(\frac{2}{||\mathbf{r}||} - \frac{1}{a}\right)}$$

$$v_r = \sqrt{\frac{\mu_E}{a(1-e^2)}}e\sin\theta$$

$$v_\theta = \sqrt{v_{pk}^2 - v_r^2}$$

$$\mathbf{v_{pk}} = v_r\frac{\mathbf{r}}{||\mathbf{r}||} + v_\theta\frac{(\mathbf{r} \times \mathbf{v}) \times \mathbf{r}}{||\mathbf{r}||^2||\mathbf{v}||}$$

Modelling the GTO in this way the TTI is located in $\mathbf{r}$ and it's at any altitude between the GTO pericenter and apocenter.

Remark, it was yet proven by previous analysis:

- Since the launcher contribution is fixed by the orbit shape but the total cost grows with altitude, the insertion cost is lower about to pericenter than to apocenter.
- For $\alpha = \pi$, after about 4.2 months large halos reach pericenter altitude. For $\alpha = 0$, small halos gain the same altitude after about 8.4 months. Accordingly, for small and large halos sampled TTI with optimum Δv_{TTI} lower then 0.81 km/s is expected in the most of cases.

Minima provided by this survey can be organized respect to types of transfer:

- **Multiple Earth Passages** (Fig. **[3.13a]**): for halo orbits with an amplitude lower than 140,000 km, the s/c leaves the Earth with a repulsive trajectory toward SEL1. After SEL1 rejections, the s/c orbits in Earth domain until a fly-by occurs. Then, SEL2-halo is reached. Some fly-by pericenter is no far from GEO altitude or lower. As shown in Tab. **[3.7]** for $A_z \leq 120,000$ the Δv_{TTI} is slightly above 0.80 km/s and the TTI altitude h lower then 300 km, the Δt transfer time is 8.5 ± 0.5 months, the longitude α is 0 ± 34 deg, the TTI latitude $\Delta \iota_z$ is no far from ecliptic plane. Unlike, the halos with $A_z \geq 120,000$ km do not have minima at perigee altitude, so the insertion cost grows.

- **Tour of Earth domain** (Fig. **[3.13b]**): It concerns halo orbits of middle amplitude. The s/c leaves the Earth with a repulsive trajectory toward SEL1. After SEL1 rejection, it performs an orbit lapping the Earth domain. Finally the s/c reaches SEL2-halo. As shown in Tab. **[3.8]** the TTI altitude is up to 9,700 km and the

Table 3.7: from GTO to SEL2-Halo $A_z \leq 140,000$

A_z [km]	Δv_{TTI} [$\frac{km}{s}$]	Δt [days]	h [km]	Δi_z [deg]	α [deg]
20,000	0.80717	249.64	293.07	2.4313	-7.7753
30,000	0.80380	249.69	247.06	2.9052	-11.033
40,000	0.81071	272.20	219.26	0.41442	32.459
50,000	0.81072	272.05	338.76	-6.4556	11.585
60,000	0.81267	250.00	381.48	-5.9267	-33.426
70,000	0.80909	250.19	217.54	5.6317	-12.131
80,000	0.80189	270.95	215.53	0.22333	28.257
90,000	0.80191	250.79	201.46	3.7961	-14.155
100,000	0.80583	251.38	276.79	11.28	-6.8056
110,000	0.80374	252.86	241.65	9.3861	-5.5851
120,000	0.88397	262.61	1557.1	39.125	27.134
130,000	1.1094	263.62	5580.7	-65.547	-32.873
140,000	1.2797	264.82	8761.5	-69.639	-49.829

Table 3.8: from GTO to SEL2-Halo $150,000 \leq A_z \leq 260,000$

A_z [km]	Δv_{TTI} [$\frac{km}{s}$]	Δt [days]	h [km]	Δi_z [deg]	α [deg]
150,000	1.3018	338.87	9205.6	32.539	-66.196
160,000	1.3123	338.24	9491.4	35.865	-68.818
170,000	1.3294	343.72	9707.4	29.244	-63.337
180,000	1.2928	343.65	9039.4	-28.312	92.207
190,000	1.2629	343.97	8434.5	33.936	-63.616
200,000	1.2327	344.50	7883.6	35.555	-63.291
210,000	1.1972	345.21	7198.0	36.809	-62.041
220,000	1.1529	346.05	6336.8	37.773	-59.584
230,000	1.0973	346.96	5301.3	38.504	-55.602
240,000	1.0282	347.87	4010.8	38.91	-48.348
250,000	0.9446	348.70	2566.1	38.311	-36.363
260,000	0.84948	349.34	953.10	32.232	-12.708

optimal Δv_{TTI} is far greater than 0.81 km/s.

- **Direct Transfer to SEL2-halo** (Fig. **[3.13c]**): for large halos, the s/c leaves the Earth toward SEL2 and approach the halo after a Δt of 4.35 ± 0.15 months (**[3.9]**). The Δv_{TTI} is slightly above 0.80 km/s and the TTI altitude h lower than 300 km in the most of the cases, the longitude α is 193 ± 20 deg. Probably the path is eclipse free, so thermal environment is about stable.

Table 3.9: from GTO to SEL2-Halo $270,000 \leq A_z \leq 500,000$

A_z [km]	Δv_{TTI} [$\frac{km}{s}$]	Δt [days]	h [km]	Δi_z [deg]	α [deg]
270,000	0.80303	128.08	200.90	16.137	-164.13
280,000	0.80261	128.32	205.48	15.898	-167.63
290,000	0.80418	128.57	228.56	15.330	-165.07
300,000	0.80755	128.84	274.96	20.115	176.08
310,000	0.80482	129.11	234.88	15.443	-166.18
320,000	0.80717	129.40	271.92	22.231	175.08
330,000	0.80540	129.59	231.50	22.827	-153.21
340,000	0.80945	129.88	217.46	23.525	-153.27
350,000	0.81201	130.34	342.66	12.241	-162.4
360,000	0.80698	130.68	209.47	18.171	-171.79
380,000	0.80996	131.41	212.68	18.407	-172.03
390,000	0.80859	131.47	277.15	31.017	-148.11
400,000	0.80774	132.20	265.19	29.988	174.05
410,000	0.80816	132.61	253.88	30.155	175.13
420,000	0.80658	132.59	238.34	31.676	-150.93
430,000	0.81681	132.99	392.01	11.538	-165.93
440,000	0.80983	133.95	288.04	15.793	-171.07
450,000	0.82283	133.84	487.05	8.6498	-165.64
460,000	0.81792	134.94	415.14	10.648	-169.36
470,000	0.80905	134.76	260.59	38.047	-151.02
480,000	0.81016	136.02	278.27	38.454	175.67
490,000	0.80825	136.58	236.61	36.024	178.08
500,000	0.80652	136.29	213.68	35.907	-154.3

- **Indirect Transfer to SEL2-halo** (Fig. **[3.13d]**): This occurs only for the halo with amplitude 370,000 km with the adopted sample pool. The trajectory, after rejection from SEL1 moves through the Earth domain directly to SEL2. As with other large halo, the budgeted Δv_{TTI} is always low, but the transfer time Δt is 7.4 months. The interesting aspect of this solution is that it allows a tour of deep space bordering the terrestrial domain at low cost. Time in the eclipse zone is small or absent, so thermal environment is approximately stable.

Table 3.10: from GTO to SEL2-Halo $A_z = 370,000$

A_z [km]	Δv_{TTI} $[\frac{km}{s}]$	Δt [days]	h [km]	Δi_z [deg]	α [deg]
370,000	0.80531	224.91	231.52	-14.533	1.4233

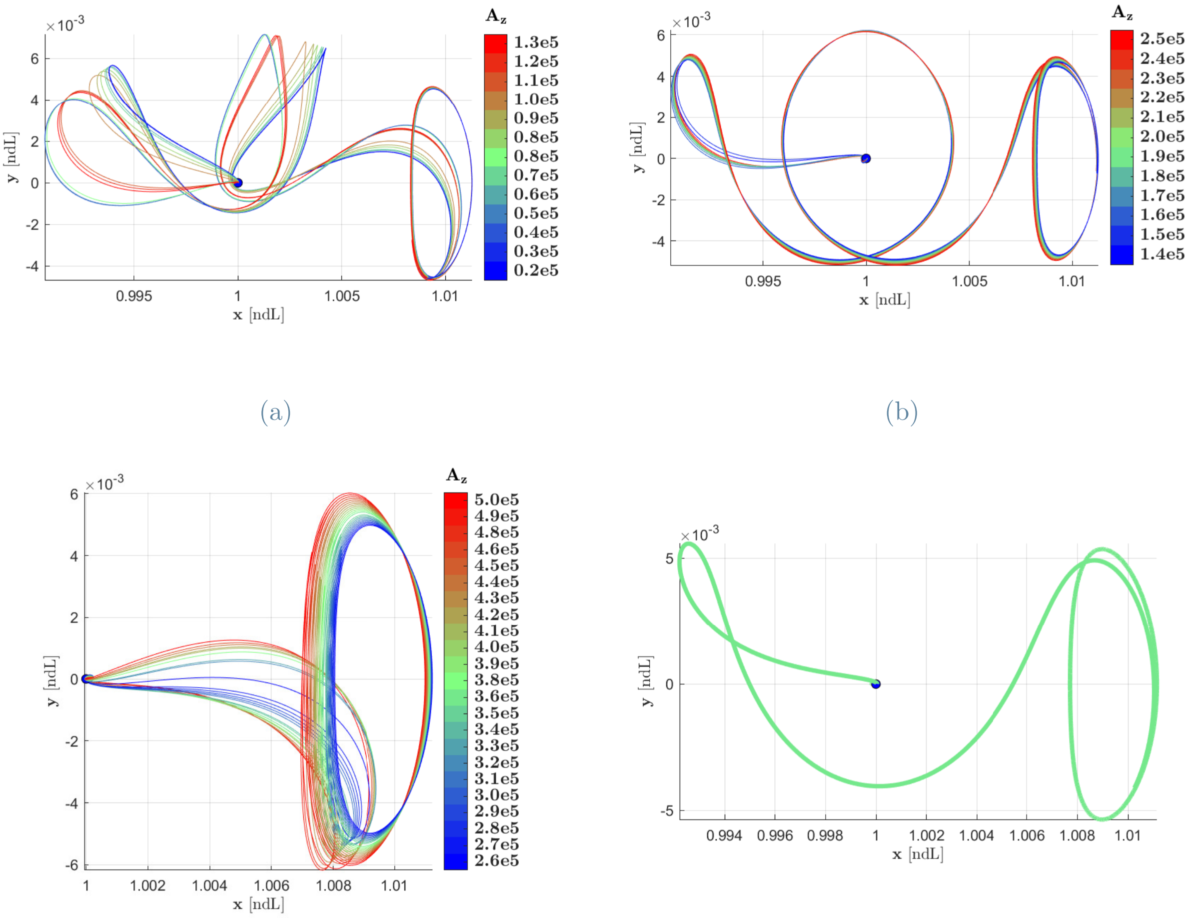

(a)

(b)

(c)

(d)

Figure 3.13: Transfer trajectories from GTO to halo. The transfer minimize the ΔV_{TTI} budget to each SEL2-halo within a year transfer time. The GTO has pericenter altitude 200 km and perfect orientation. **[3.13d]** refers to halo A_z 370,000 km.

Summarising, all the transfers seen so far exploit hyperbolic manifolds. All of them provide a low-cost design to leave a GTO parking orbit to reach a libration point orbit at SEL2. Between them multipassages, indirect and direct paths perform better then tour transfer type. Minima can be denoted as efficient but not optimal since they are obtained by a sample pool. However, if the mesh is dense, these efficient minima provide a initial good guess to optimisation methods.

3.3.2. Efficient low-cost Δv_{TTI} from LEO

The LEO is modelled as a circular orbit with altitude between 200 and 2,000 km. The LEO velocity direction and magnitude are computed by Eq. **[3.4]**,**[3.5]**.

From the previous analysis, note that:

- The insertion cost Δv_{TTI} from LEO decreases with altitude. So, if the cost of the Hohmann manoeuvre Δv_H to reach the LEO is not added the optimum will be as close as possible to highest altitude h.
- The highest border of this analysis is 2,000 km. So, looking to Fig. **[3.8a]** at this altitude an insertion budget of 2.88 km/s is expected.
- For about $\alpha = \pi$ the most of the trajectories will be direct transfers to large amplitude SEL2-halo. For around $\alpha = 0$ Earth multiple passages transfers to small amplitude SEL2-halo are expected.
- In the current time span of a year, transfer from LEO to some of the medium-amplitude halo orbits may prove impossible.

The results in Tab. **[3.11]** show indeed that no trajectories from LEO to halo of amplitude $140,000 \leq A_z \leq 210,000$ are available. For the rest, the different types of trajectory can be recognised by the transfer time and longitude angle α.

- Transfer time of about 4.3 months are related to direct transfer. Most of halos with amplitude $A_z \geq 220,000$ have this behaviour. Just few of them are reached by means of indirect transfer, such us halo A_z 370,000. In this case the transfer requires between 7.3 and 8.3 months.
- With a transfer time of approximately 8.3 most of halos $A_z \leq 130,000$ km arrive to SEL2 after rejection from SEL1 and Earth passage. Only for A_z 40,000 and 60,000 km SEL2 is reached in 11 months after tour transfer.

3.4. 1^{st} Level Targeting Algorithm

Despite the execution of some corrective manoeuvres, in reality the s/c will have to perform the transfer at a slightly different location with respect to the space manifold TTI. A targeting manoeuvre between the actual initial state where the insertion manoeuvre is really executed and the desired final state in HOI must be considered to fulfill the mission.

One approach to implement the targeting is to solve a 2-points BVP i.e., the initial and final location $\mathbf{\bar{r}_1}, \mathbf{\bar{r}_2}$ are given as well as the transfer times $\mathbf{t_1}, \mathbf{t_2}$, while the velocities of initial and final state $\mathbf{v_1}, \mathbf{v_2}$ are the unknown.

The algorithm is a pure numerical method, so it presumes an approximate initial guess. Here it's assumed as reference the stable manifold between the TTI where the s/c would have to insert the manifold and the HOI that the s/c must reach.

Since the manifold is stable the method is applied backward. The main idea of algorithm is propagate backward the final state with its STM and compute the error i.e., the target variables. Then use the STM and the evaluated error to perform a 1^{st} order correction of control variables. Hence propagate backward again and reiterate until the error falls down a tolerance value.

Table 3.11: from LEO to SEL2-Halo

A_z [km]	Δv_{TTI} [$\frac{km}{s}$]	Δt [days]	h [km]	Δi_z [deg]	α [deg]
20,000	2.8850	249.66	1973.0	0.67569	-21.380
30,000	2.8833	249.70	1984.2	0.8917	-21.848
40,000	2.8846	333.57	1975.8	1.5304	14.322
50,000	2.8820	249.83	1994.7	1.9785	-19.936
60,000	2.8847	331.40	1974.7	2.0507	11.539
70,000	2.8846	250.04	1976.5	2.0480	-20.481
80,000	2.8854	250.18	1972.2	2.7950	-19.114
90,000	2.8848	250.37	1974.9	2.9138	-18.616
100,000	2.8829	250.61	1987.6	3.4007	-17.355
110,000	2.8835	250.97	1984.0	3.4819	-15.985
120,000	2.8833	251.65	1985.8	3.5591	-13.421
130,000	2.8813	254.89	1996.7	2.0463	-4.3647
220,000	2.8814	127.14	1999.0	12.941	-165.35
230,000	2.8828	127.33	1993.5	13.640	-163.14
240,000	2.8842	127.52	1987.3	13.949	-163.62
250,000	2.8822	127.71	1998.4	14.271	-171.94
260,000	2.8816	127.94	1999.4	15.348	-160.94
270,000	2.8854	128.15	1978.7	15.940	-160.33
280,000	2.8830	128.41	1993.1	15.948	-174.34
290,000	2.8880	128.61	1965.2	17.093	-159.30
300,000	2.8888	128.93	1961.5	17.149	-175.62
310,000	2.8851	129.21	1983.3	17.661	-176.01
320,000	2.8847	129.37	1990.7	18.442	-158.65
330,000	2.8831	129.80	1998.8	18.424	-176.18
340,000	2.8862	130.12	1980.2	19.131	-176.81
350,000	2.8872	130.22	1974.7	20.712	-156.76
360,000	2.8854	130.79	1987.4	20.868	-178.38
370,000	2.8866	224.28	1979.7	-19.816	-1.7383
380,000	2.8853	226.66	1990.8	-20.589	3.0885
390,000	2.8897	229.05	1965.5	-19.701	7.5218
400,000	2.8909	131.86	1958.2	23.912	-155.30
410,000	2.8848	233.73	1994.6	-21.889	15.246
420,000	2.8858	132.62	1993.9	26.194	-154.06
430,000	2.8920	133.60	1959.2	25.474	179.97
440,000	2.8893	134.07	1971.7	25.222	-179.45
450,000	2.8865	134.55	1988.8	25.857	-179.59
460,000	2.8854	134.31	1996.7	27.820	-154.30
470,000	2.8943	253.71	1950.7	-25.903	44.411
480,000	2.8881	135.26	1983.1	29.661	-153.97
490,000	2.8882	136.70	1984.9	29.069	179.87
500,000	2.8880	136.30	1987.4	30.771	-154.04

The algorithm requires a variational control equation. Let's set:

fixed final point: $\bar{\mathbf{r}}_{\mathbf{2}} = \mathbf{r}_{\mathbf{HOI}}$
fixed constraints: $\delta\mathbf{r}_{\mathbf{2}} = 0, \delta t_1 = \delta t_2 = 0$
free variables: $\delta\mathbf{v}_{\mathbf{1}}$
target initial point: $\bar{\mathbf{r}}_{\mathbf{1}}$
target variables: $\delta\mathbf{r}_{\mathbf{1}} = \bar{\mathbf{r}}_{\mathbf{1}} - \mathbf{r}_{\mathbf{1}}$
control variables: $\delta\mathbf{v}_{\mathbf{2}}$

Each i-state is defined by its location $\mathbf{r}_{\mathbf{i}}$, velocity $\mathbf{v}_{\mathbf{i}}$, acceleration $\mathbf{a}_{\mathbf{i}}$ and time t_i. Therefore, in the general case the differential variational system has 20 variables:

$$\begin{bmatrix} \delta\mathbf{r}_{\mathbf{2}} - \delta\mathbf{v}_{\mathbf{2}}\delta t_2 \\ \delta\mathbf{v}_{\mathbf{2}} - \delta\mathbf{a}_{\mathbf{2}}\delta t_2 \end{bmatrix} = \begin{bmatrix} \mathbf{A}_{\mathbf{21}} & \mathbf{B}_{\mathbf{21}} \\ \mathbf{C}_{\mathbf{21}} & \mathbf{D}_{\mathbf{21}} \end{bmatrix} \begin{bmatrix} \delta\mathbf{r}_{\mathbf{1}} - \delta\mathbf{v}_{\mathbf{1}}\delta\mathbf{t}_{\mathbf{1}} \\ \delta\mathbf{v}_{\mathbf{1}} - \delta\mathbf{a}_{\mathbf{1}}\delta\mathbf{t}_{\mathbf{1}} \end{bmatrix} \tag{3.14}$$

Adding the fixed constraints, the system becomes:

$$\begin{bmatrix} \mathbf{0} \\ \delta\mathbf{v}_{\mathbf{2}} \end{bmatrix} = \begin{bmatrix} \mathbf{A}_{\mathbf{21}} & \mathbf{B}_{\mathbf{21}} \\ \mathbf{C}_{\mathbf{21}} & \mathbf{D}_{\mathbf{21}} \end{bmatrix} \begin{bmatrix} \delta\mathbf{r}_{\mathbf{1}} \\ \delta\mathbf{v}_{\mathbf{1}} \end{bmatrix} \rightarrow \begin{bmatrix} \delta\mathbf{r}_{\mathbf{1}} \\ \delta\mathbf{v}_{\mathbf{1}} \end{bmatrix} = \begin{bmatrix} \mathbf{A}_{\mathbf{21}} & \mathbf{B}_{\mathbf{21}} \\ \mathbf{C}_{\mathbf{21}} & \mathbf{D}_{\mathbf{21}} \end{bmatrix}^{-1} \begin{bmatrix} \mathbf{0} \\ \delta\mathbf{v}_{\mathbf{2}} \end{bmatrix} \tag{3.15}$$

Since the state is propagated backward, so is the STM. Hence:

$$\begin{bmatrix} \mathbf{\Phi}_{\mathbf{rr}} & \mathbf{\Phi}_{\mathbf{rv}} \\ \mathbf{\Phi}_{\mathbf{vr}} & \mathbf{\Phi}_{\mathbf{vv}} \end{bmatrix} = \begin{bmatrix} \mathbf{A}_{\mathbf{21}} & \mathbf{B}_{\mathbf{21}} \\ \mathbf{C}_{\mathbf{21}} & \mathbf{D}_{\mathbf{21}} \end{bmatrix}^{-1} \tag{3.16}$$

Hence, the variational control equation is :

$$\delta\mathbf{r}_{\mathbf{1}} = \mathbf{\Phi}_{\mathbf{rv}}\delta\mathbf{v}_{\mathbf{2}} \tag{3.17}$$

Finally, the 1^{st} order correction is obtained:

$$\delta \mathbf{v_2} = \mathbf{\Phi_{rv}}^{-1}\, \delta \mathbf{r_1} \tag{3.18}$$

Note that at each k-iteration $\delta \mathbf{r_1}^{(k)}$ is computable because the target $\bar{\mathbf{r}}_\mathbf{1}$ is known and $\mathbf{r_1}^{(k)}$ is obtained by integration.

Summarise, at each iteration given $\mathbf{s_2^{(k)}} = (\bar{\mathbf{r}}_\mathbf{2}, \mathbf{v_2^{(k)}})$ are updated the STM, the target variables and the control variables such that $\mathbf{s_2}^{(k+1)}$ is defined recursively as:

$$\mathbf{s_2}^{(k+1)} = (\bar{\mathbf{r}}_\mathbf{2}, \mathbf{v_2}^{(k)} + \delta \mathbf{v}^{(k)}) \tag{3.19}$$

The method does not guarantee a solution, but if it converges, it requires only a few iterations.

The last step is to compute the maneuver cost given the parking orbit and the targeted halo.

$$\Delta \mathbf{v_{TTI}} = \mathbf{v_1^{(k)}} - \mathbf{v_{pk}} \tag{3.20}$$

$$\Delta \mathbf{v_{HOI}} = \mathbf{v_{HOI}} - \mathbf{v_2^{(k)}} \tag{3.21}$$

$$\Delta v_{TOT} = ||\Delta \mathbf{v_{TTI}}|| + ||\Delta \mathbf{v_{HOI}}|| \tag{3.22}$$

Anderson and Lo [2009] highlight that optimization algorithms converges on manifold trajectories without knowledge of manifolds. Some remarks on it must be done:

- As yet pointed, a close manifold is a good initial guess for a targeting algorithm.
- The expected Δv_{HOI} is a small fraction of Δv_{TTI}. Indeed for a stable manifolds Δv_{HOI} is zero, so the targeting Δv_{HOI} converge to zero.
- For the sake of example, let's consider: a circular parking orbit 200 km altitude; a halo A_z 290,000 km; a close manifold on section $(y = 0) \wedge (x < 1 - \mu_1)$. The

targeting algorithm provides solutions $\Delta v_{TTI} = 3.2670$ km/s and $\Delta v_{HOI} = 0.26$ m/s.

In conclusion, also performing a targeting maneuver the mission Δv-budget is mainly driven by insertion from the parking orbit to the transfer trajectory.

3.5. Additional Costs

Up to now, only perfectly oriented parking orbits for a pericentre or apocentre insertion have been considered. However, even for dedicated launches, there is always the requirement to perform some corrective manoeuvres. In the case of non-dedicated commercial launches, corrections can become quite significant. This section considers manoeuvres for changing the inclination, shape and apse line. Referring to the parking orbit, this description is based on the dimensionless R2BP model, with Earth planetary constant μ_E. Manoeuvres for phase changes are not covered since they are related to time available to carry out the manoeuvre.

Change of inclination

The required budget is directly proportional to s/c velocity at maneuver time. For this reason the change of inclination budget is higher for a LEO that for a GTO. Indeed, for a circular LEO the velocity is constant and always high since it's at low altitude by definition. Instead a GTO can perform the maneuver at is apocenter, when the s/c is far from Earth and slower.

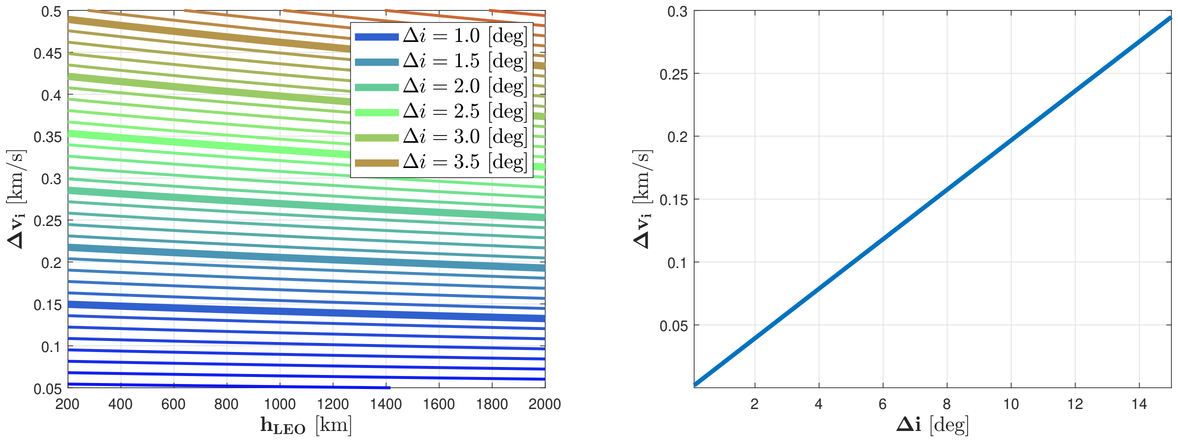

(a) (b)

Figure 3.14: Additional costs. Change of inclination budget for circular LEO with altitude between 200 and 2000 km at left. On the opposite side, the budget for GTO.

The change of inclination budget Δv_i is estimated as follow.

$$\text{LEO: } \Delta v_i = 2\sqrt{\frac{\mu_E}{r}}\sin\left(\frac{\Delta i}{2}\right) \tag{3.23}$$

$$\text{GTO: } \Delta v_i = 2\sqrt{\frac{\mu_E}{r_a}}\sqrt{\frac{2r_p}{r_p + r_a}}\sin\left(\frac{\Delta i}{2}\right) \tag{3.24}$$

As shown by Fig. **[3.14]** on the right, for LEO the Δv_i is not really sensible to altitude h but to inclination change magnitude Δi. To guarantee a change of just 3.5 degrees a budget slightly less then 0.5 km/s Δv_i must be expected. This is a modest change of angle, allowing limited flexibility at launch. However, a further increase in the corrective manoeuvre budget could result in an unacceptable burden on the mission.

On the right of the same figure we show the budget for a GTO orbit. Since the change of plane is performed to apocenter, the expected Δv_i is considerably less. A maneuver of 5.0 degrees has a budget of about 0.1 km/s.

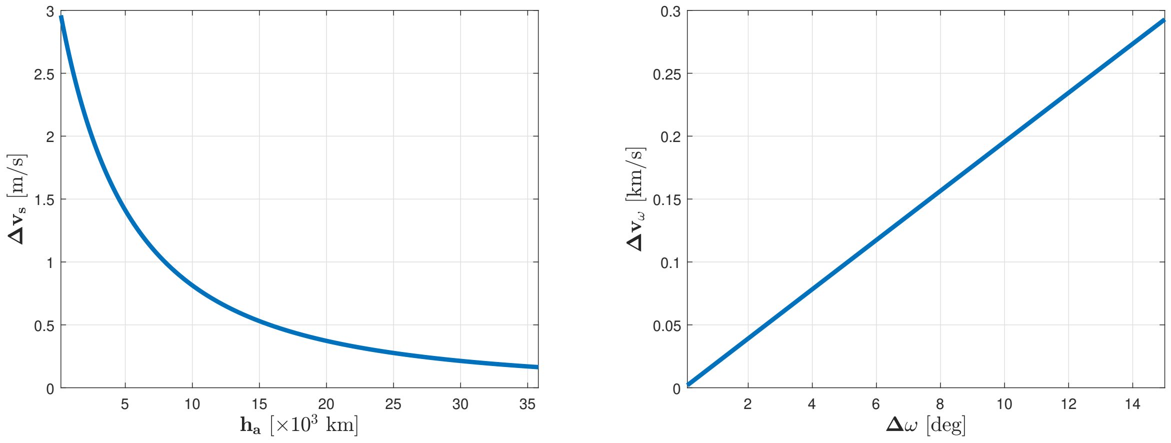

(a) (b)

Figure 3.15: Additional costs. On the left the budget Δv_S for a change of shape maneuver: pericenter at 200 km altitude, while the altitude of apocenter at h_a is increased of 10 km. At right the cost Δv_ω for a apse line rotation manoeuvre of a GTO.

Change of Shape

Let's consider an orbit with 200 km altitude pericenter and apocenter altitude h_a. In Fig. **[3.15a]** it is computed the cost to reshape the apocenter altitude of 10 km δh using:

$$\Delta v_s = \sqrt{\frac{\mu_E}{r_p}} \left(\sqrt{\frac{2(r_a + \delta h)}{r_p + r_a + \delta h}} - \sqrt{\frac{2r_a}{r_p + r_a}} \right) \tag{3.25}$$

The budget is between 2.0 and 3.0 m/s for LEO, and less than 0.2 m/s for GTO. Overall, the change of shape maneuver is negligible in preliminary analysis.

Apse Line Rotation

In order to achieve a perfect orientation it's possible change the argument of pericente ω_p. Clearly a circular orbit doesn't requires such a maneuver, but it's used on GTO. Assumed that the GTO size must be maintained, in R2BP the budget Δv_ω is given by:

$$\Delta v_\omega = 2\sqrt{\frac{\mu_E}{a(1-e^2)}}\; e \;\sin\left(\frac{\Delta\omega_p}{2}\right) \tag{3.26}$$

As illustred by Fig. **[3.15b]**, the maneuver has approximately the same behaviour of a change of inclination. Similarly, a cost of 0.1 km/s for a 5.0 degrees change is expected.

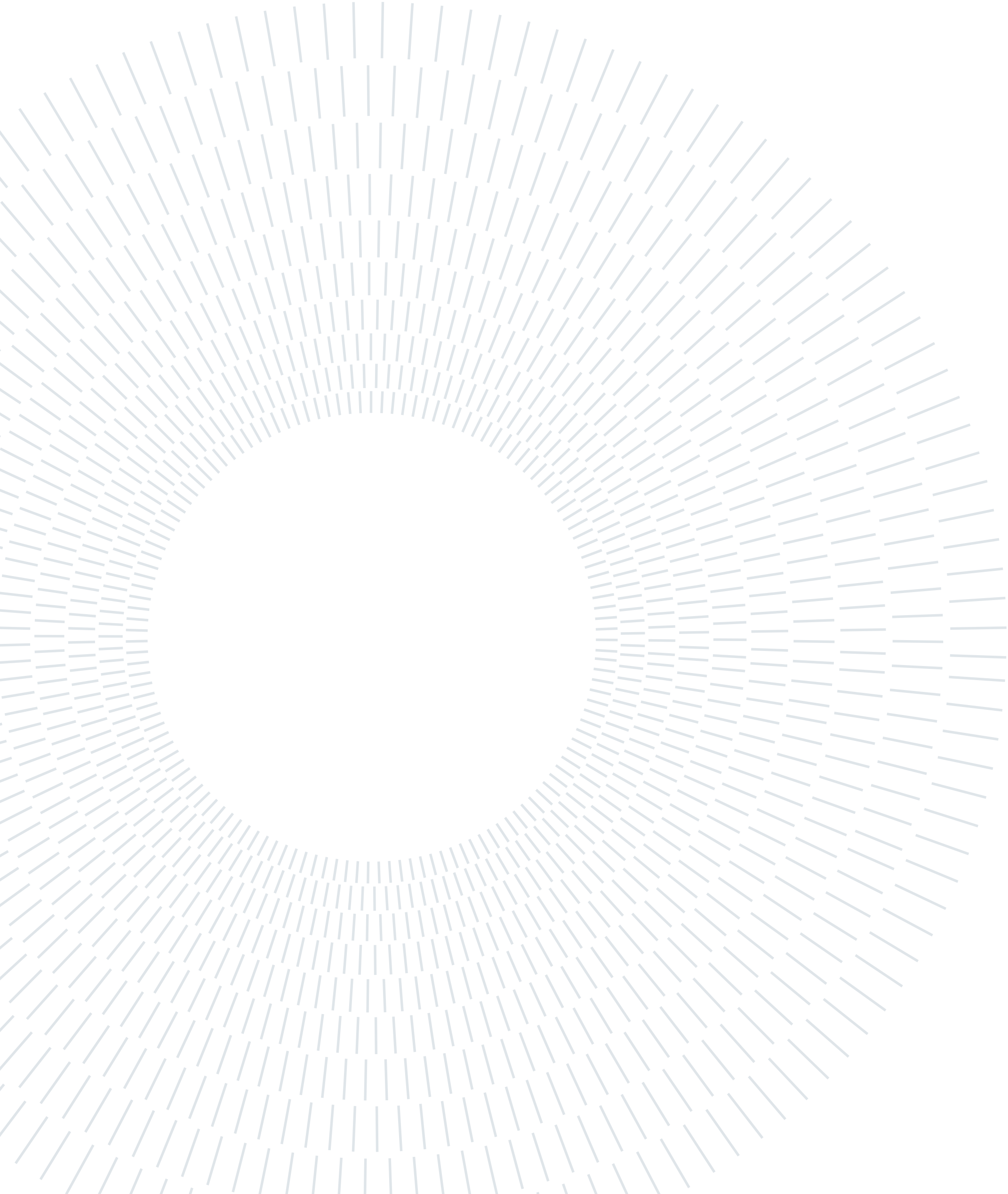

4 | Orbit selection and application to the REMEC mission

4.1. Introduction

This study offers a parametric analysis to support the preliminary design of a SEL2-halo space mission. The investigation is conducted in the CR3BP, which offers a conservative approach and timeline independence.

Although in the literature are already planned missions to SEL2 in the Sun-Earth system, there is no detailed work doing a parametric analysis to choose the operational orbit. Producing such an analysis is the research problem we deal with in this chapter.

The interest of this particular scenario is clarified by the trade-off analysis by Aguilar et al. [04/2023]. Despite the report refers to a case studio (REMEC mission), by extension it covers any S-class ESA missions (budget $\leq$ 50 M€). The report demonstrates that albeit small class missions have limited performances and restricted budget they can have access to the deep space not only through piggyback, but also by means of a clever mission design that optimises the use of hyperbolic manifolds: trajectories targeting a SEL2-halo orbit fit into this category. Piggyback resets the launch Δv_{TTI} budget, however the range of available orbits is constrained by the primary mission. Conversely, a possible ridesharing at a commercial LEO or GTO allows a broad mission spectrum at a low Δv_{TTI} cost.

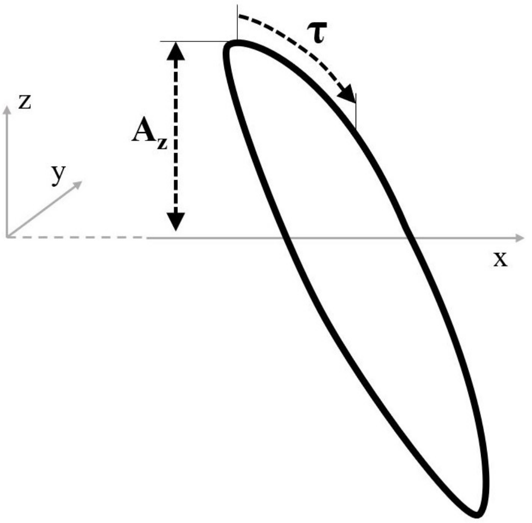

(a)

Figure 4.1: Sketch of the arrival parameterisation: A halo orbit by the maximum positive z-coordinate such that $A_z = \max(+z)$; along the orbit a point is identified by τ.

This investigation parameterised the halo orbits according to the A_z amplitude and τ time as described in Fig. **[4.1]**. The parameter A_z is equal to the maximum value in the $+z$ coordinate reached by a generic halo orbit, while τ is the forward propagation time from $z = A_z$. The parameter τ can be normalised over the halo period of the orbit T.

By means of the two coordinates $(A_z, \tau/T)$ a phase-space surface is defined. The phase space can be used to characterize the performance of the transfer trajectories between a Geostationary Transfer Orbit (GTO) and a halo orbit. In this investigation, the phase space $(A_z, \tau/T)$ it is named arrival surface.

On the other side, fixing an altitude with respect to the Earth surface, the departure point can be identified by two angular coordinates as shown in Fig. **[3.3]**, using as angles α and Δi_z. Concerning the reference system centred in Earth, the x-axis is directed along the Sun-Earth conjunction line, the z-axis is represented by the out-of-plane direction and the y-axis belongs to the ecliptic plane. With respect to principal x-axis the angles $\alpha, \Delta\iota_z$ are the ecliptic longitude and latitude. However in CR3BP the reference system is rotating and the x-axis is not the vernal axis, so this thesis refers to α as in-plane angle and $\Delta\iota_z$ as inclination angle.

Main References: This works try to merge a phase space approach to a mission design exploiting manifolds (Canalias Vila [2007], Koon et al. [2011] and Canales et al. [2021]). By similarity is also worth mentioning the recent contribution of Ojeda Romero and Howell [2022]. Further references are given inside.

Chapter Outline: In this chapter is performed a parametric analysis to select a Earth-to-SEL2-halo transfer. The main driver of the selection is the transfer budget. Performance parameters of halo maps are stability **[4.2.2]** **[4.2.3]**, Earth visibility **[4.2.4]**, eclipse avoidance **[4.2.5]**, availability of and hyperbolic manifold from Earth **[4.3.1]**. On the departure surface are mapped transfer performances as budget, transfer time and A_z of reachable halos **[4.3.2]**. All data are related to TTI coordinates $(\alpha, \Delta\iota_z, h)$. Departure maps allows to identify the Poincaré surfaces to investigate both the insertion budget Δv_{TTI} versus the altitude h, and the relationship between the Launcher and the TTI selection. TTI budget was covered by previous chapter, however here that investigation is extended **[4.3.4]**. Simultaneously a case studio is conducted: the REMEC preliminary mission design. Then, starting from the data provided by the parametric analysis an initial guess to optimize a low-budget objective function in CR3BP **[4.4.1]** and BR4BP **[4.4.2]** is set. To conclude, two End-of-Life (EoL) design profiles are conducted and compared **[4.5]** and it's carried a parametric description of EoL time versus budget trade-off **[4.5.1]**.

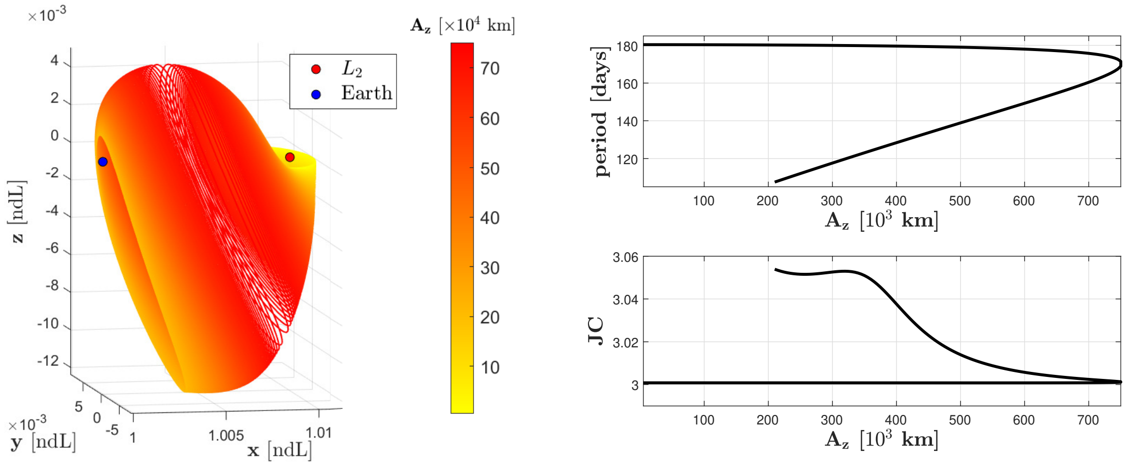

(a) (b)

Figure 4.2: South SEL2-halo orbits. **[4.2a]**: 3D view of family in the dimensionless synodic frame; the color bar shows halo A_z amplitude between 5,000 km up to 750,000 km. **[4.2b]** halo orbital T period (top) and JC Jacobi constant (bottom) versus A_z halo amplitude.

4.2. Halo Parametric Selection

In this section it is performed a parametric analysis to select a target halo. The main driver of the selection is the transfer Δv-budget. The performance parameters considered are the transfer time, the robustness and the stability of the selected orbit, orbit time in the excluded zone[1] and in the eclipse zone. All these parameters will be explained in the following.

The family of halo orbits together with the corresponding amplitude, period and energy level is shown in Fig. **[4.2]**. The halo family is obtained through continuation method from the SEL2-Lyapunov orbit as detailed in Sec. **[2.7]**. The adopted driver parameter is the north sphere amplitude A_z, that is the maximum positive z-coordinate of each orbit.

From the maximum amplitude of about 750,000 km the halo family branches into two legs: one move to SEL2, the other one to Earth. In both of them the A_z parameter

---

[1] A region between the Sun and Earth characterised by significant magnetic phenomena (Canalias Vila [2007]).

decreases. On the one hand, the continuation method stops as planar Lyapunov orbit bifurcation is reached. On the other hand, the continuation method could continue until collision with the Earth. Alternatively, it could be stopped around EML1 distance ($\approx$ 326,390 km) at which the Moon passing by causes a ballistic capture (Miller and Belbruno [1991]). Actually, the method is stopped for amplitude 5,000 km in proximity of SEL2, while close to Earth the minimum A_z is 220,000 km. It's used an A_z step of 5,000 km.

The halo's selection proposed here proceeds initially through considerations based on energy level and orbit stability.

4.2.1. Jacobi Constant

Regarding the Jacobi constant (JC), it is interesting to note that, for the family of orbits approaching L2 the JC value is almost constant. More correctly its value very slight decreases from SEL2 to A_z 525,000 km, where the minimum 3.0008 is reached. On the other leg the JC value grows up to the maximum 3.053 at A_z 320,000 km. Then, with A_z 255,000 there is a local minimum of 3.051. We must point out:

- There are for the same amplitude A_z two values of JC (and period T). This is because there are halo orbits that have the same amplitude but are either closer to SEL2 or closer to Earth. The halo orbits towards SEL2 have at the same A_z lower Jacobi constant (and higher T).
- The presence of orbits with the same JC means the possibility to search for a zero budget transfer trajectory.
- Also when a zero budget trajectory cannot be found, it's remarkable that the difference between the maximum and minimum JC is just 0.043. Consistently, in the literature, a halo-to-halo transfer is a low-cost manoeuvre, requiring a Δv in the order of few m/s, achievable even with continuous thrust.

- For A_z equal to 471,267 km, JC is 3.0185, which is about the same as for a GTO orbit with altitude of the pericentre equal to 200 km. Unfortunately, this does not means that such an transfer trajectory can be performed in a reasonable transfer time.

It is reasonable to assume that injection from GTO to transfer orbit requires an increase in kinetic energy. This implies that, assuming to use a GTO as a near-Earth parking orbit, it will be possible to reach a halo orbit characterized by a JC value slightly lower than that of a GTO. It is suggested to target a halo such that the JC value is less than 3.0185.

4.2.2. Stability Index

In this study, as a proxy of the station keeping cost the stability index of a halo orbit is used. Information about the stability of an orbit is embedded in its monodromy matrix **M**, which is known numerically. Indeed, the monodromy matrix M is defined as the State Transition Matrix (STM), computed over an orbital period. An introduction to monodromy matrix and his 6 eigenvalues is provided in Sec. **[2.5]**. The literature provides a well-established description of the topic. Here we refer to Deprit and Price [1965], Davis et al. [2017], Zimovan-Spreen et al. [2020].

In order to evaluate the stability of a reference orbit trajectory an initial displacement $\delta\mathbf{x_0}$ from a reference state is supposed. $\delta\mathbf{x_0}$ defines the radius of a 6-dimensional spheroid centred into the initial state. The spheroid bounds the initial uncertainty. After a given time, by natural dynamics the state of the s/c is bounded inside a 6-dimensional ellipsoid and the vector $\delta\mathbf{x}(\mathrm{t})$ provided the 6-dimensional ellipsoid semi-axes.

The initial and final uncertainties $\delta\mathbf{x_0}$, $\delta\mathbf{x}(\mathrm{T})$ are related by the monodromy matrix **M** i.e., by the eigenpairs $(\lambda_n, \mathbf{e_n})$, such that for small displacements follows:

$$\delta\mathbf{x}(kT) = \sum_{i}^{n} \lambda_i^k \, \delta x_0 \mathbf{e_i} \tag{4.1}$$

Hence, it's clear that the stability is related to eigenvalues λ_i since if $|\lambda_i| < 1 \; \forall \; i$ then $||\delta\mathbf{x}(kT)|| \rightarrow 0$. In the first chapter, it has already been observed that all halos have an eigenvalue λ_1 greater than 1 and are therefore unstable. Precisely for this reason, λ_1 magnitude is usable to formulate a measure of orbit instability. Find eigenvalues in planar case can be avoided. Indeed, since a matrix trace is equal to the sum of all eigenvalues, $\lambda_2 = 1/\lambda_1$ and $\lambda_3 = \lambda_4 = 1$:

$$\mathrm{tr}(\mathbf{M}) \approx \lambda_1 + \frac{1}{\lambda_1} + 2 = 2 \; \mathrm{SI} + 2 \tag{4.2}$$

Where the monodromy matrix $\mathbf{M}$ is known numerically and SI is the Stability Index. Straightforward, two possible definitions of Stability Index (SI) are used from the literature (Soldini [2016]):

$$\mathrm{SI}_\lambda = \frac{1}{2}\left(|\lambda_1| + \frac{1}{|\lambda_1|}\right) \tag{4.3}$$

$$\mathrm{SI}_{tr} = \frac{1}{2} \; \mathrm{tr}(\mathbf{M}) - 1 \tag{4.4}$$

In planar case, until λ_1 is real and positive the two SI formulations are equivalent. In the first equation the absolute operator is added since the monodromy matrix is numerically obtained and computational error affect the eigenvalue.

In general the monodromy matrix has two further complex conjugate eigenvalues λ_5, λ_6 such that $|\lambda_5| = |\lambda_6| = 1$. So, if $\lambda_1 >> 1$ the contribution of $\Re(\lambda_5), \Re(\lambda_6)$ to $tr(\mathbf{M})$ is negligible and $\mathrm{SI}_\lambda \approx \mathrm{SI}_{tr}$ is still true. However, as the orbit becomes less unstable λ_1 decreases and the two SI formulations describes a slightly different behaviours, as Fig. **[4.3]** elucidates: from the maximum amplitude the SI branches in two legs. The first leg

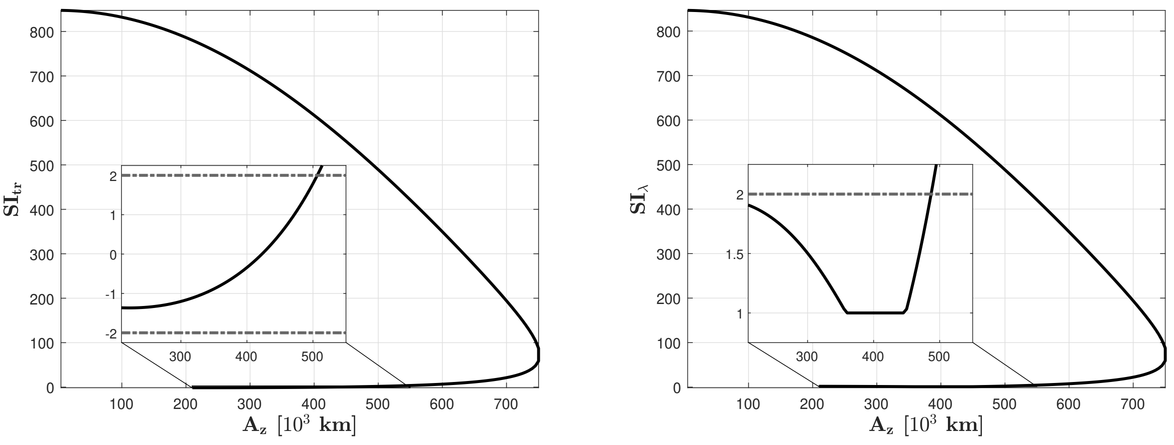

(a)
(b)

Figure 4.3: Comparison between SEL2-halos Stability Index computation in the Sun-Earth+Moon system, overview and zoomed sub-window for NRHO. On the left, SI_{tr} is computed by the trace of monodromy matrix $\mathbf{M}$. At right the $\mathbf{M}$ maximum eigenvalue is used to compute SI_{λ}.

reaches SEL2 with increasing instability. On the second leg, halos approaching the Earth show a low SI value. In the picture the second leg is zoomed for $A_z <$ 550,000 km.

According to the literature, an orbit is marginally stable when its $|\mathrm{SI}| = 1$, it is slightly unstable for $|\mathrm{SI}| < 2$, it is unstable for $|\mathrm{SI}| \geq 2$. This subdivision applies to both above definitions. In Fig. **[4.4]** they are highlighted in green the halos such that both the SI formulations meet the marginally stable condition, while orbits for which only one of the two SI formulations describes a marginally stable condition are highlighted in yellow. The orbits identified by the colour grey are unstable or slightly unstable according to SI_{λ}. It's clear that the SI_{λ} is the most strict criterion (Fig. **[4.4b]**).

Considering the family of halos approaching Earth instead of L2, SI_{λ} is equal to 1 for values of A_z between 360,000 km and 450,000 km. For $A_z <$ 360,000 km, orbits will be slightly unstable since they are bounded by marginally stable halos. Consequently, halo orbits approaching Earth with $A_z \leq$ 450,000 km are Near-Rectilinear Halo Orbits (NRHOs). On the other hand, all halos from the planar Lyapunov bifurcation up to

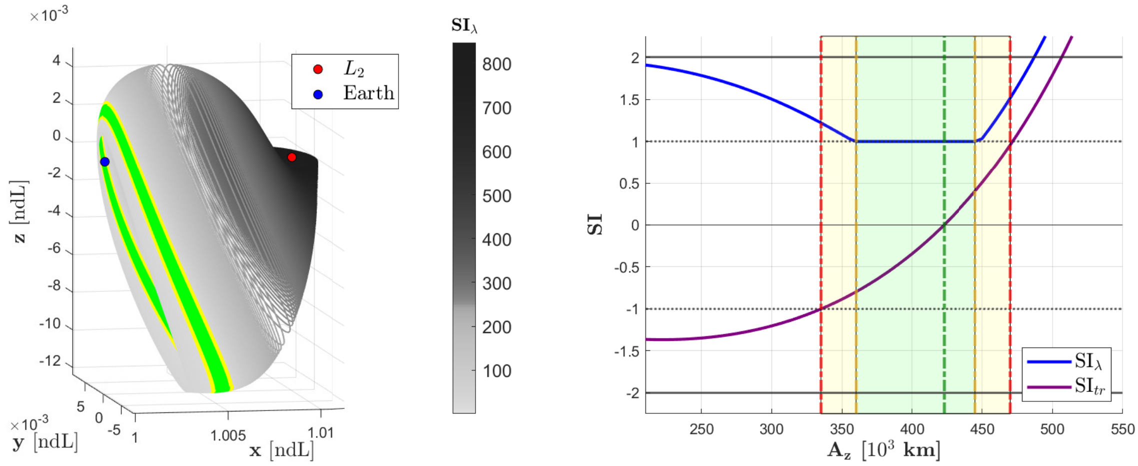

(a) (b)

Figure 4.4: Stability Index on SEL2 Halo orbits **[4.4a]** and comparison between SI_λ and SI_{tr} **[4.4b]**: green when both the indices fulfill the marginally stable condition, yellow if just one, otherwise gray per SI_λ.

NRHO are unstable[2].

4.2.3. Finite Time Lyapunov Exponent

Let us recall that:

$$\delta\mathbf{x}(t_0 + \Delta t) = \mathbf{\Phi}(t_0 + \Delta t, t_0)\ \delta\mathbf{x}(t_0)$$

Thus, performing the scalar product $\delta\mathbf{x} \cdot \delta\mathbf{x}$:

$$||\delta\mathbf{x}||^2 = \delta\mathbf{x_0}^T\ \mathbf{\Phi}^T\ \mathbf{\Phi}\ \delta\mathbf{x_0}$$

Note that $\mathbf{\Phi}^T\mathbf{\Phi}$ is the Cauchy-Green tensor. Given its maximum eigenvalue λ_1:

$$\max||\delta\mathbf{x}||^2 = \lambda_{1,\mathbf{\Phi}^T\mathbf{\Phi}}\ ||\delta\mathbf{x_0}||^2 \tag{4.5}$$

---

[2] Between NRHO and $A_z \leq 487{,}000$ km the orbits fulfill the slightly unstable condition, however their natural dynamics can easy evolve to the stronger unstable halos.

Under the linear approximation, it's assumed an exponential relation between the propagation time Δt and the perturbation $\delta \mathbf{x}$. Accordingly, let us define FTLE σ such that:

$$\max||\delta \mathbf{x}(t_0 + \Delta t)|| = e^{\sigma(t_0, \Delta t)\ \Delta t} \max||\delta \mathbf{x}(t_0)||$$

That is,

$$\max||\delta \mathbf{x}||^2 = e^{2\sigma \Delta t} \max||\delta \mathbf{x_0}||^2 \tag{4.6}$$

By comparison between Eq. 4.5 and Eq. 4.6:

$$\sigma(t_0, \Delta t) = \frac{\ln \lambda_{1,\mathbf{\Phi}^T\mathbf{\Phi}}}{2\Delta t} \tag{4.7}$$

On an orbit $\mathbf{\Phi}^T\mathbf{\Phi} = \mathbf{M}^T\mathbf{M}$ and $\Delta t = T$.

$$\sigma(t_0, T) = \frac{\ln \lambda_{1,\mathbf{M}^T\mathbf{M}}}{2T} \tag{4.8}$$

That defines the FTLE on an orbit[3]. It's logarithmically proportional to the Cauchy-Green maximum eigenvalue and inversely proportional to the propagation time. This means that for the same amount of time, a lower FTLE indicates an exponential decrease in the Cauchy-Green principal stress. The FTLE does not measure the stability of an orbit but its chaoticity, or, in other words, its sensitivity.

By definition, an orbit with a low FTLE value is desired since the latter belongs to a robust orbit. Figure **[4.5]** shows the FTLE trends on halo orbits and compares it to SI_λ. The FTLE is about constant and lower than 2.75 for halos towards SEL2. Instead, slightly unstable halos and NRHO have high FTLE value.

---

[3] For details, we refer to Parker and Chua [2012] and Tang and Boozer [1996].

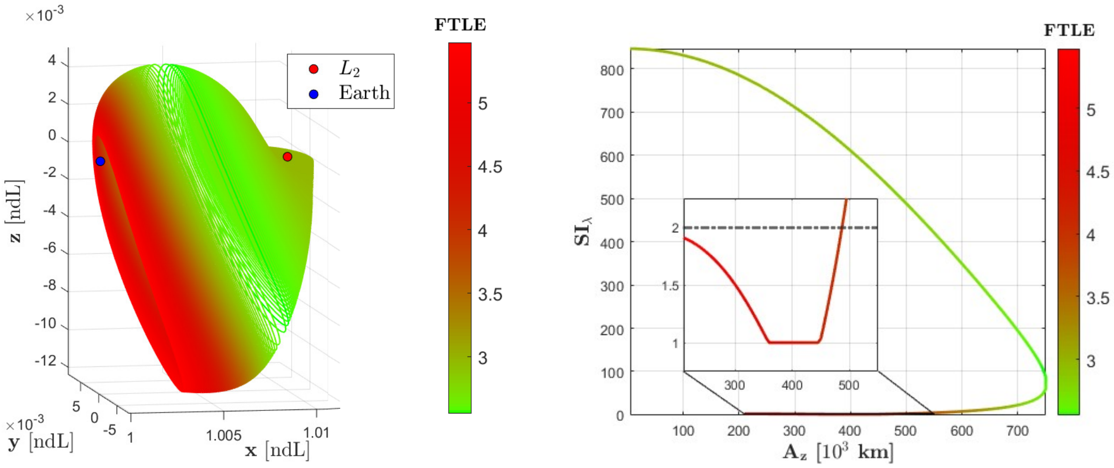

(a) (b)

Figure 4.5: FTLE versus SI_λ on Halos. Low FTLE characterizes mostly halos toward L2 **[4.5a]**. NRHO have high FTLE **[4.5b]**.

4.2.4. Telecommunication constraints

At this point, in compliance with what was stated beforehand, the analysis can be restricted to only halo orbits between A_z 750,000 km and SEL2.

To assess the requirements for the telecommunication subsystem, we consider that its performance will be related to the position of the spacecraft with respect to the Earth, which can be expressed in spherical Earth centred coordinates $(h, \alpha, \Delta\iota_z)$. The altitude h is a variable of the Link Budget equation[4]. The latitude $\Delta\iota_z$ influences the ground stations choice.

In Fig. **[4.6]** the distance with respect to Earth r_E and the latitude $\Delta\iota_z$ of the family of studied halo orbits are shown, both as average and as intervals along the orbit. While the mean value is about constant, it should be noted that the range widens considerably as A_z increases.

To meet the requirements of the telecommunications subsystem, a small halo orbit would

---

[4] Allnutt [1989]

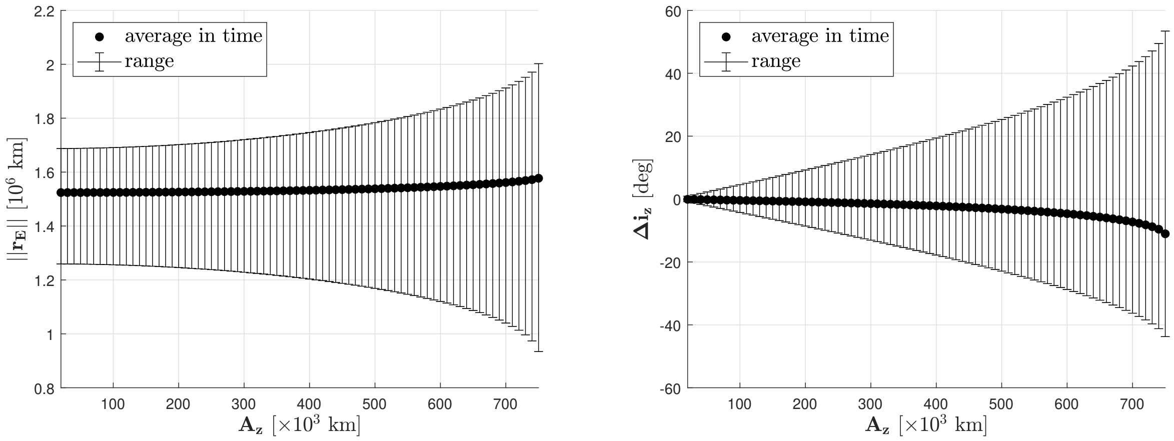

(a) (b)

Figure 4.6: Earth visibility and telecommunication for halo orbits between A_z 750,000 km and SEL2. Versus the A_z halo amplitude the Earth distance r_E **[4.6a]** and the ecliptic latitude $\Delta\iota_z$ **[4.6b]**.

be preferable. Indeed, in Europe, for obvious reasons, there are very few radar stations above 60° latitude, and the angle between the equatorial and ecliptic plane is 23.5°. Therefore, to limit the maximum inclination, it is reasonable to set $A_z < 500{,}000$ km.

4.2.5. Power and thermal constraints

The power and thermal requirements are related to the sunlight presence, to its direction with respect to the spacecraft and to solar radiation pressure. The absence of sunlight during some phases of the orbital motion is mainly related to the eclipse due to the Earth. Other shadow sources, such as the Moon or other celestial bodies, are not considered in this analysis. Earth's shadow region is drawn as a truncated cone, with radius equal to 14,000 km in SEL2 (Canalias Vila [2007]). For in-depth investigation, it is suggested the approach adopted in Pergola and Alessi [2012].

In Fig. **[4.7]** the relationship between eclipse time, considered both as days and in relation to orbital period, and A_z is illustrated.

- To have an eclipse free halo orbit it's enoungh to set $A_z > 13{,}000$ km.

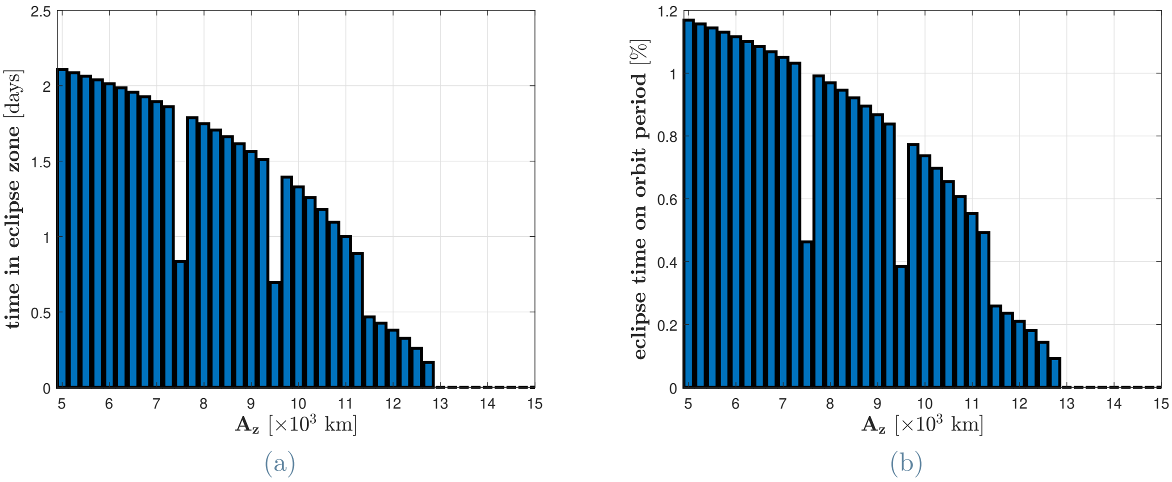

(a) (b)

Figure 4.7: Eclipse time in days **[4.7a]** and in relation to the orbital period **[4.7b]**. On the x-axis the halo orbit amplitude A_z.

- For $A_z < 13{,}000$ km the eclipse time is quite short compared to the orbital period but is not negligible. In fact, for all cases analysed, the satellite enters the shadow only once or twice. Each time this occurs, it remains in the eclipse zone for up to 24 hours.

In Fig. **[4.8]**, the mean distance between the spacecraft and the Sun r_S is represented as function of A_z. The value of r_S is almost constant and barely above 1 AU. . The above is sufficient to say that the distance between the Sun and the satellite does not create any issue related to energy availability. Moreover, since the standard deviation of that distance computed over an orbital period, σ_{r_S},is small for all the studied orbits, in sunlight the thermal influence of the Sun on the satellite is almost constant. Thus, if an eclipse phase can be avoided, the requirements of the thermal control subsystem can be greatly narrowed.

In the same figure, also the angle δ_{EpS} between Earth and Sun, calculated with respect to the spacecraft. The angle δ_{EpS} is computed versus the amplitude A_z and in terms of maximum, minimum and average on the orbit. From the image it is possible evaluate for each halo δ_{EpS} range and deviation. Overall, its maximum positive deviation is 18.8

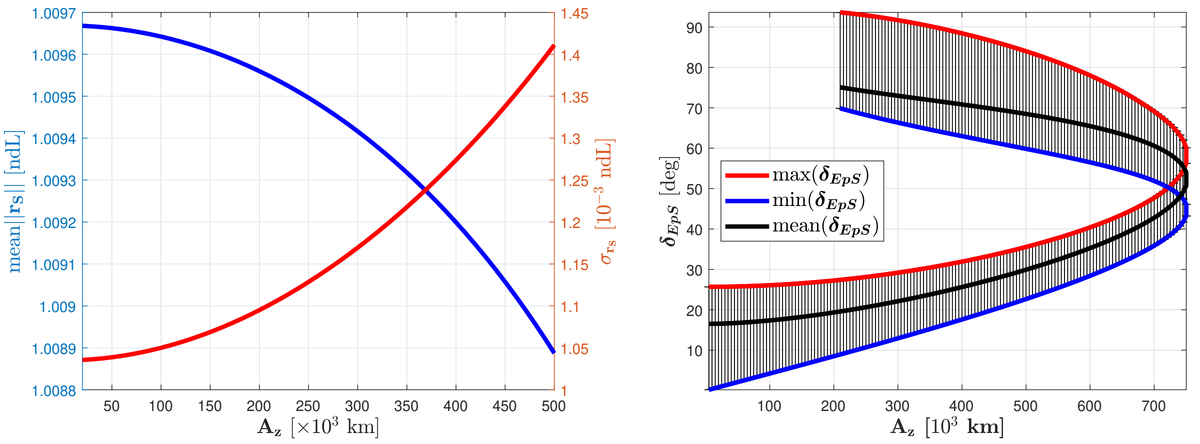

(a) (b)

Figure 4.8: Power constraints versus A_z halo amplitude: Sun distance from the operative orbit mean value and divergence **[4.8a]**; Earth-halo-Sun δ_{EpS} angle minimum, maximum and mean on each operative halo orbit **[4.8b]**.

degrees, while the negative deviation is 16.3 degrees. The behaviour of angle δ_{EpS} is required to perform design choices in the spacecraft configuration e.g., antennas and solar panels.

4.3. Transfer Parametric Selection

In the previous Sec. **[4.2]** the parametric study on the operational orbit is presented. In this section the parametric study of the transfer trajectory is performed instead. Finally in Section **[4.4]** based on the results of Sec. **[4.2]** and this section, the final orbit selection for a baseline mission is performed.

To select the operational halo orbit, in addition to the criteria outlined so far, one must certainly consider the trajectory and Δv-budget required to reach the orbit. The aim of this section is to perform a parametric analysis of the transfer trajectories from Earth to SEL2-halo. The goal is archived by mapping the transfer performances in three ways: on the arrival map, on the departure map, on the Poincaré map.

- The arrival map is defined as a phase space that characterizes halo orbits by means of two coordinates, A_z and τ/T.
- The departure map is characterized by a second phase space, which is used to parameterize the Earth-centred synodic reference system using two sets of coordinates: (1) spherical coordinates: altitude h (fixed), ecliptic latitude Δi_z and longitude α defined with respect to the x-axis (Fig. **[3.3]**); (2) altitude h, true anomaly θ of the spacecraft at transfer trajetory insertion, manoeuvre angle β (Fig. **[4.15a]**).
- The Poincaré map is defined as a surface with a fixed longitude α, a variable altitude h and latitude Δi_z.

The analysis is performed in the dimensionless Sun-Earth+Moon synodic reference system, where the position of the Earth is assumed to be that of the barycentre of the Earth+Moon system. For analyses related to the parking orbit, only the Earth influence is considered. It's assumed that a low-cost transfer trajectory at a targeted halo will be similar to a stable manifold associated with the same orbit. The transfer orbit is stretched between two fixed points. The first of the latter belongs to the parking orbit and is called TTI (Transfer Trajectory Insertion) point, it will be identified also as the departure point. The second, or arrival point, is identified as HOI (Halo Orbit Insertion) point.

4.3.1. General Performances at fixed altitude

As starting point, let us consider the simple design strategy illustrated in Fig. **[4.9]**. First, the halo Orbit Insertion (HOI) points are computed: they are the arrival points of the corresponding stable invariant manifold. Assume that the stable manifolds are propagated backward in time for 1 year or until it is reached a 200 km altitude respect to Earth. Now the stable manifolds connect two extremes: on one hand, the arrival points belong to halo orbits; on the other hand, only a fraction of the initial points reached the vicinity of Earth.

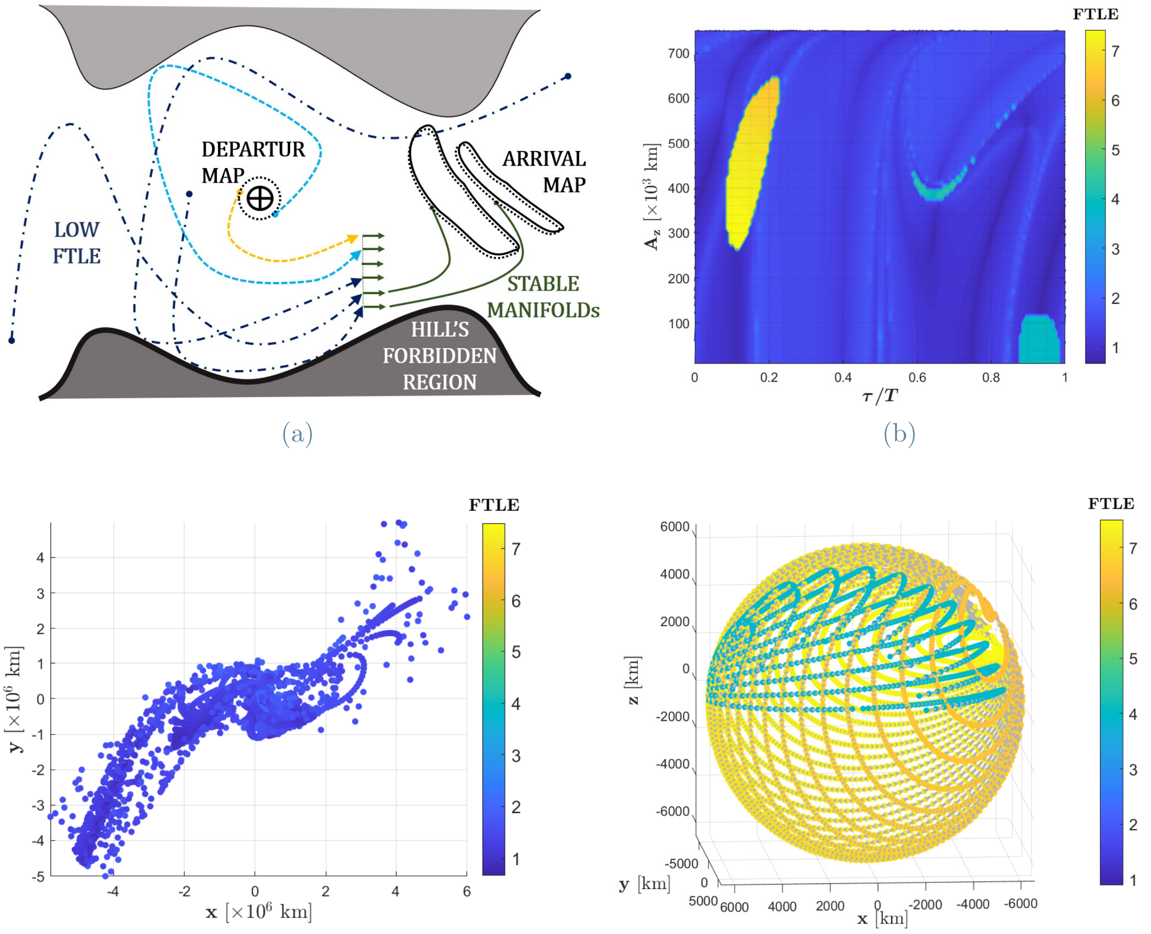

(a) (b)

(c) (d)

Figure 4.9: Transfer trajectory and FTLE. Arrival and departure map are defined, then from halos stable manifolds are propagated backward 1 year time span **[4.9a]**. Transfer trajectory FTLE is mapped on the arrival map **[4.9b]**. The higher the value, the more robust the transfer is: low FTLE defines initial states far from Earth belonging to a CR3BP invariant structure **[4.9c]**; high FTLE locates launch points i.e., the stable manifold leaves tracks on the departure surface **[4.9d]**.

Simultaneously with the state, the STM is propagated along the trajectory. It is possible to map the FTLE value reached at the end of each backward propagation, as a function of A_z and τ/T. The result of the mapping process is illustrated in Fig. **[4.9b]**. Analysing the FTLE values obtained allows some suboptimal transfer trajectories to be discarded. A high FTLE indicates that a highly sensible position (for example Earth proximity) is reached in a short time. Regarding the analysis described in this report, the latter condition identifies a good solution.

Moreover, for a low value of FTLE, empirically fixed as 2.6, trajectories never reach Earth and so all this group of transfer trajectory can be discarded. In Fig. **[4.9c]** it is shown the departure location of these trajectories in the synodic reference system. They mostly belong to stable manifolds from internal or external interplanetary space.

Looking at Fig. **[4.9b]**, it is possible to identify three regions of interest: the first, yellow-coloured, in the upper left part of the graph, the second and third, cyan-coloured, in the right part of the graph. With FTLE > 2.6, they identify trajectories that, when propagated backward, reach Earth (Fig. **[4.9d]**). Anyway, different kinds of transfer can be classified. As summarize in Tab. **[4.1]**, following the classification introduced in Sec. **[3.3]** the transfer can be:

- **Direct to SEL2-halo**: this condition is achieved for a high FTLE value and 270,000 $\leq A_z \leq$ 640,000 km. The spacecraft leaves Earth in the direction of SEL2 and approaches the halo orbit after a transfer time of about 128.0 $< \Delta t <$ 148.5 days. For very large halos, a polar or retrograde parking orbit may be required. Therefore, it might be appropriate to target halos for which $A_z \leq$ 500,000 km. In Fig. **[4.11a]**, direct transfers to halo orbits are illustrated.
- **Multiple Earth passages**: this condition is characterized by an average value of FTLE and $A_z \leq$ 110,000 km. In the case of small-amplitude halos as target

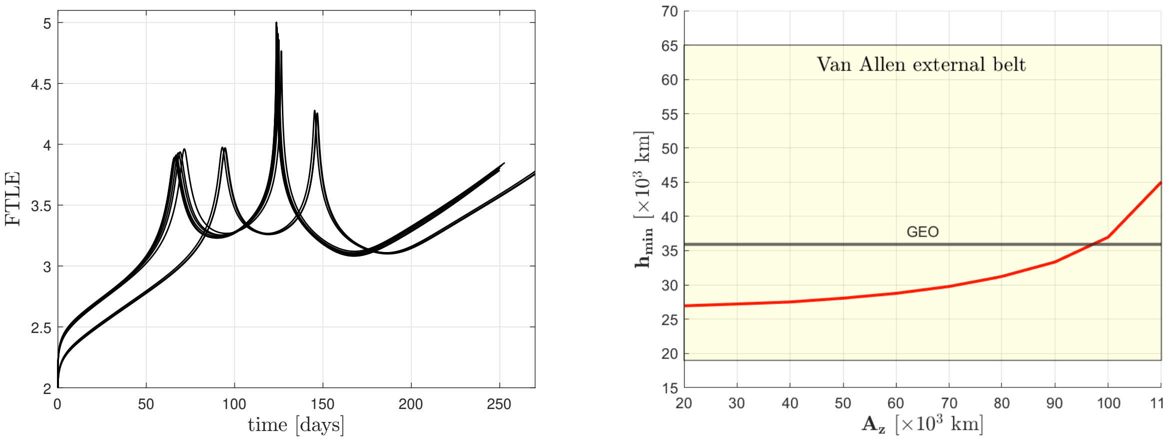

(a)

(b)

Figure 4.10: Transfer trajectory to small amplitude halos and risks. **[4.10a]** FTLE in time on the transfer path; presence of multiple picks are related to Earth passages. **[4.10b]** Minimum altitude versus A_z: comparison with GEO and Van Allen external belt altitude.

orbits, the spacecraft leaves Earth with a repulsive trajectory toward Sun Earth L1. After Sun Earth L1 repulsion, the spacecraft passes very close to Earth several times before reaching one of the operational halo orbits. The transfer time is $249.6 < \Delta t < 271.2$ days. In Fig. **[4.11c]**, these kinds of transfers are illustrated. The presence of multiple near-Earth passages affects the mission risk: (1) the effect of perturbations due to the proximity between Earth and the transfer orbit must be considered; (2) crossing the upper bound of the Van Allen Belt shortens the on-board electronics lifetime; (3) the collision risk with other objects must be evaluated and in case avoided, if the spacecraft gets lower than the Geosynchronous Earth Orbit (GEO) altitude. To plan possible corrective manoeuvres, Fig. **[4.10a]** shows the evolution of the FTLE value along some transfer trajectories chosen as examples. The FTLE value is represented as a function of transfer time. The peaks are correlated with the satellite's near-Earth passages. The higher the peak, the lower the altitude reached relative to Earth's surface. In Fig. **[4.10b]**, the trend of the minimum altitude reached by the spacecraft versus A_z is represented, too.

- **Indirect to SEL2-halo**: this condition is identified by an average value of FTLE

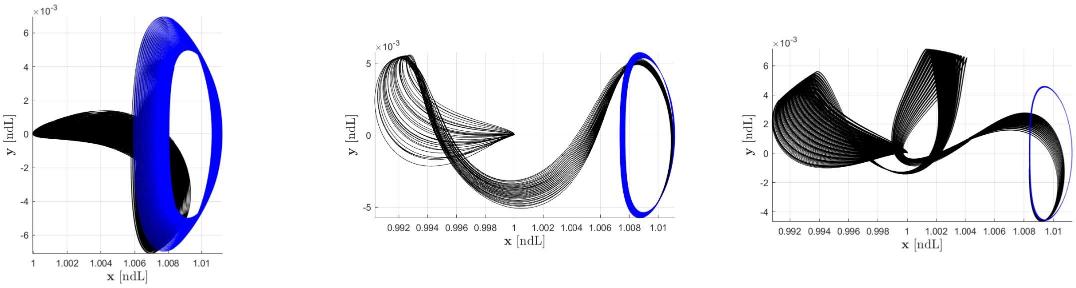

(a) (b) (c)

Figure 4.11: Transfer trajectory options within 1 year transfer time to SEL2-halo from 200 km altitude parking orbit: (a) direct transfers to SEL2-halo; (b) indirect transfer to SEL2-halo; (c) multiple Earth passages

Table 4.1: link options within 1 year to SEL2 Halo from 200 km altitude

$\mathbf{A_z}$ [km]	**Multipassage**	**Tour**	**Indirect**	**Direct**
$\leq 110,000$	V	X	X	X
$120,000 - 260,000$	X	X	X	X
$270,000 - 360,000$	X	X	X	V
$370,000 - 420,000$	X	X	V	V
$430,000 - 640,000$	X	X	X	V
$\geq 650,000$	X	X	X	X

and 370,000 $\leq A_z \leq$ 460,000 km. The trajectory starts from TTI heading, first, toward Sun Earth L1. It then experiences a rejection action by the latter and moves back, traveling in the Earth's domain toward Sun Earth L2. The transfer time is $227.5 < \Delta t < 249.6$ days. In Fig. **[4.11b]**, indirect transfers to halo orbits are shown.

The detected Transfer Trajectory Insertion points allow to map the departure performances at a fixed Earth altitude, here fixed at 200 km.

Finally, Fig. **[4.12]** shows departure maps, graphs that relate the location of possible TTI points, identified by latitude and longitude of a spherical surface of radius equal to that of the Earth plus 200 km, to the relative halo amplitude A_z, transfer time Δt and inclination i_{TTI} values. The maps show that the TTIs are naturally arranged along isolines. Each isoline represents the trace of all stable manifolds leading to the same halo orbit, i.e., of a space tube. All TTI points belonging to the same isoline have a halo orbit with equal A_z amplitude as their target. With departure maps it is possible to visualize which halo is reachable, chosen a fixed TTI point, how much transfer time would be required, what orbital inclination of the TTI point, i_{TTI}, must be imposed to enter the space manifold. Remarkably, many solutions require polar or retrograde GTOs, especially for large halo $A_z > 500{,}000$ km. These considerations will be necessary to select a launcher for the mission.

4.3.2. Budget Performance at fixed altitude

The results obtained following the procedure described in Sec. **[4.3.1]** can be analyzed as a budget performance. Indeed, one of main driver of a transfer selection is the insertion budget Δv_{TTI}.

A GTO is selected as a possible parking orbit. The chosen orbit has a pericentre altitude of 200 km and an apocentre altitude equal to that of a GEO, such radii r_p, r_a are given. In addition, the orientation of the GTO is selected such as:

- Its perigee coincides with the injection point in the transfer trajectory.
- The orbit belongs to the plane of the manifold that connects it to the operational halo orbit.

Let us call $\tilde{\mathbf{v}}_{\mathbf{pk}}$ the velocity of the parking orbit in the R2BP inertial reference system, $\mathbf{v_{pk}}$ in the CR3BP synodic reference system. Remind that $\mathbf{n_1}$ is the angular rate to move from inertial to synodic reference system, μ_E is the dimensionless Earth gravity constant, e is the parking orbit eccentricity. Finally, let us suppose to know the states $\mathbf{r}, \mathbf{v}$ of stable manifolds mapped at pericentre altitude, where $\mathbf{r}$ is the radius respect to Earth.

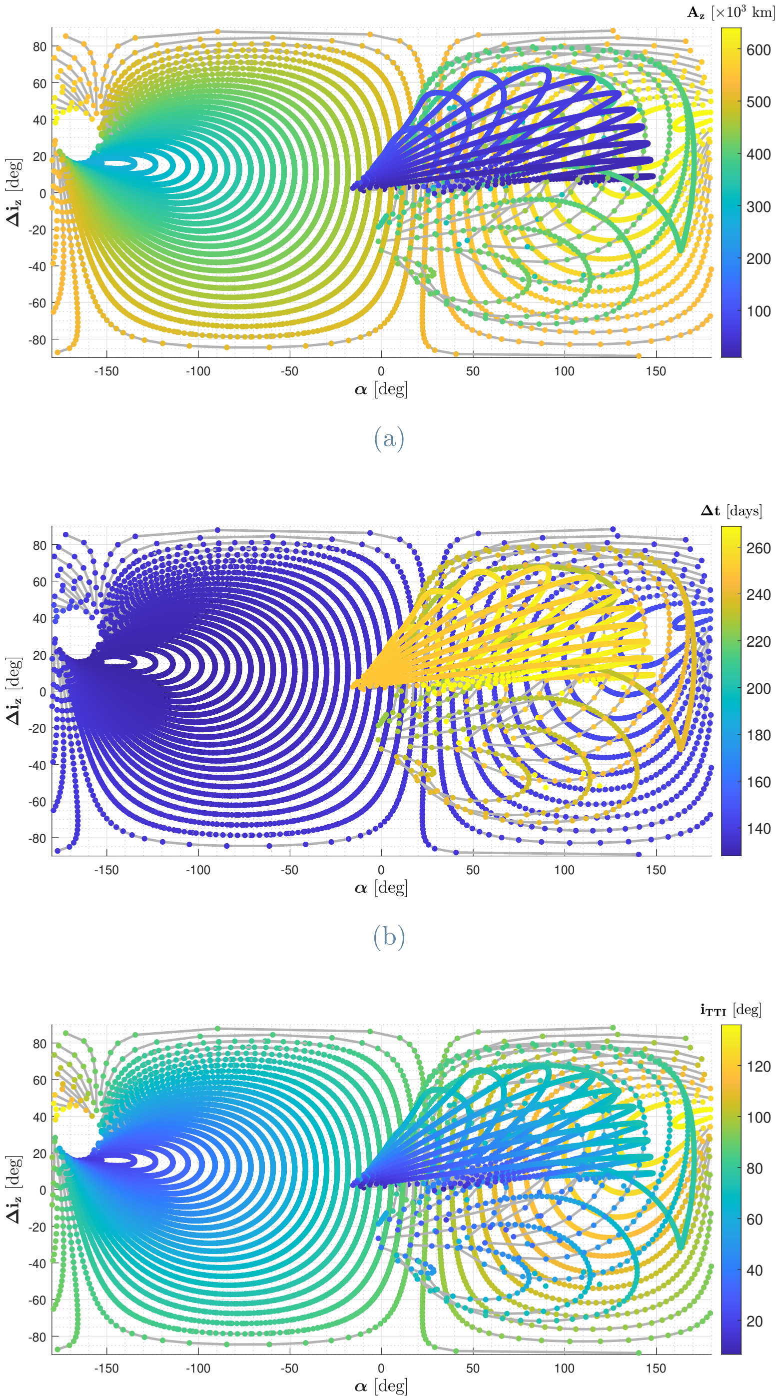

(a)

(b)

(c)

Figure 4.12: Parametric analysis at 200 km altitude. The color bar reports the amplitude **[4.12a]**, the transfer time **[4.12b]** and the orbital inclination at TTI **[4.12c]**. Each track is a stable manifold and a Jacobi constant isoline. On axes the spherical coordinated $(\alpha, \Delta\iota_z)$ define the departure location.

The following scalar and vectorial relationships must be fulfilled:

$$\begin{aligned}
&e = \frac{r_a - r_p}{r_a + r_p} \\
&\mathbf{\tilde{v}_{pk}} \perp \mathbf{r} \\
&(\mathbf{v} \times \mathbf{r}) \cdot \mathbf{v_{pk}} = 0 \\
&\tilde{v}_{pk} = \sqrt{\frac{\mu_E(1+e)}{r_p}} \\
&\mathbf{v_{pk}} = \mathbf{\tilde{v}_{pk}} + (-\mathbf{n_1}) \times \mathbf{r}
\end{aligned} \tag{4.9}$$

Point-by-point, given the manifold location respect to Earth $\mathbf{r}$, his velocity $\mathbf{v}$ and the magnitude of $\mathbf{\tilde{v}_{pk}}$:

1. It is computed the normal direction $\mathbf{\hat{h}} = \mathbf{r}/||\mathbf{r}|| \times \mathbf{v}/||\mathbf{v}||$,
2. It is imposed $\mathbf{\tilde{v}_{pk}} = \tilde{v}_{pk}\ (\mathbf{\hat{h}} \times \mathbf{r}/||\mathbf{r}||)$.
3. It's evaluated $\mathbf{v_{pk}}$ by Eq. **[4.9]**.
4. Finally the insertion budget is computed by vectorial difference $\Delta v_{TTI} = ||\mathbf{v} - \mathbf{v_{pk}}||$.

A LEO is also considered as a possible parking orbit. The considered LEO is circular, with an altitude of 200 km. The LEO orbit is designed in the same way of GTO simply by setting $r_a = r_p$.

The resulting maps **[4.13]** provide the GTO and LEO budget to a fixed altitude of 200 km on the departure surface. Budget maps detect the low-cost transfer opportunity at a fixed altitude in term of $(\alpha, \Delta\iota_z)$ coordinates. On the one hand, these could be constraints to dating the Launch and phasing the parking orbit. On the other side, the maps detect the in-plane angles α of interest for a variable altitude parametric analysis.

The minimum on-board Δv_{TTI} required is equal to 0.83 km/s for the GTO case, to 3.27

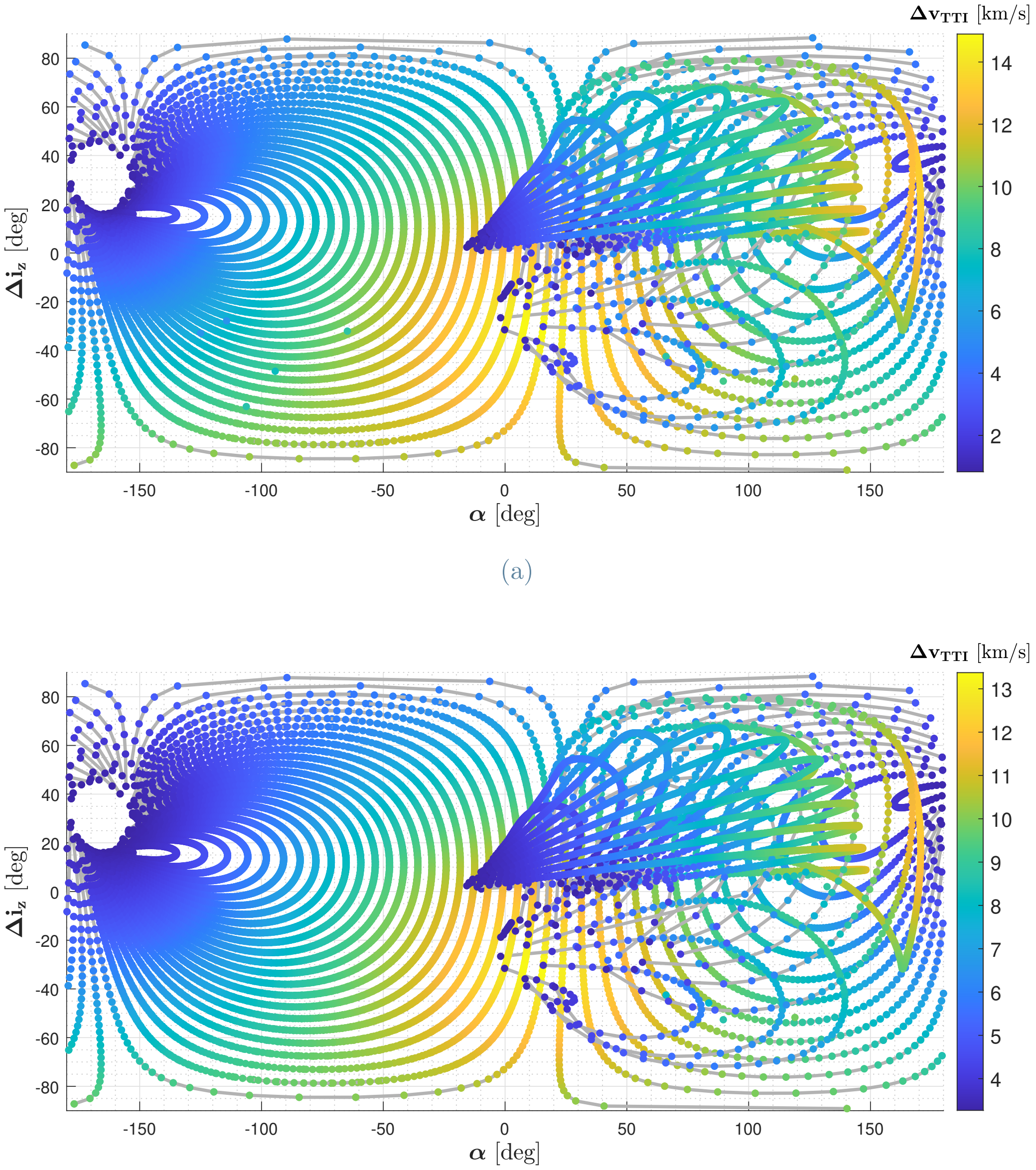

(a)

(b)

Figure 4.13: Parametric analysis at 200 km altitude. Departure map from GTO pericenter **[4.13a]** and LEO **[4.13b]**. On axes the spherical coordinated $(\alpha, \Delta\iota_z)$, the color bar reports the insertion budget Δv_{TTI}.

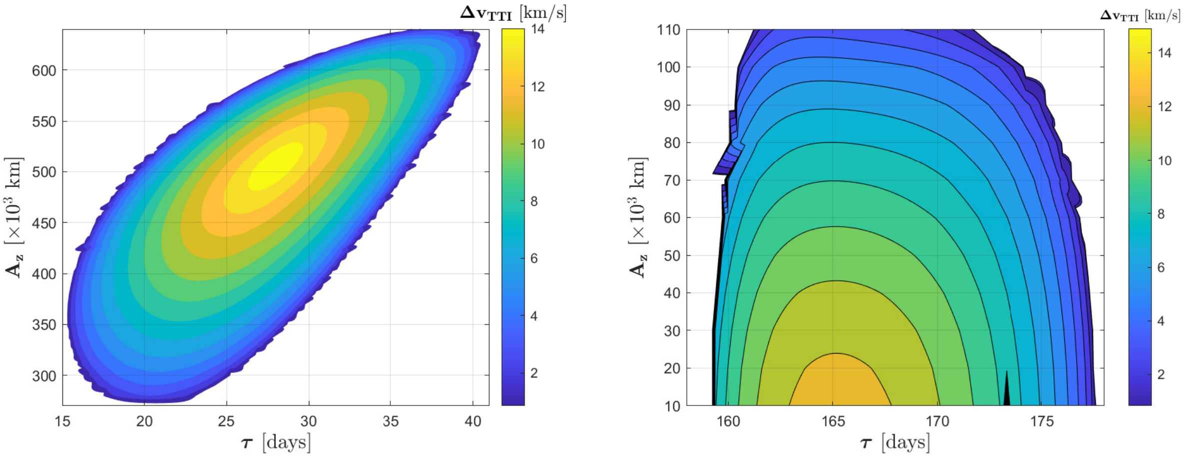

(a)

(b)

Figure 4.14: Parametric analysis at 200 km altitude. Arrival map from GTO pericenter and direct transfer at large halos **[4.13a]** or multipassages transfer to small halos **[4.13b]**. On axes the halo parameters (τ, A_z), the color bar reports the insertion budget Δv_{TTI}.

km/s for the LEO case. It should be noted that the GTO case will require a larger contribution from the launcher in terms of Δv at the beginning of the mission. Indeed, considering the launcher contribution, the overall consumed Δv is lower in the case a LEO is chosen as parking orbit. However, a GTO will allow for a lower Δv demand on board, so eventually the latter is more convenient.

In Fig. **[4.14]** the required Δv_{TTI} budget is represented as function of τ and A_z. It can be observed that there is a well-defined group of Halos for which insertion budget turns out to be small. From now on, the analyses will focus on the latter set of possible operational orbits.

4.3.3. Budget exploiting Poincaré maps

By imposing an in-plane angle α, while variable altitude and inclination, a $(h, \Delta\iota_z)$ surface is set. On this surface the incoming parking orbit trajectory and the outgoing stable manifolds leave their marks: the result is a Poincaré map. Once the trajectories are patched the required insertion manoeuvre Δv_{TTI} is known. This thesis carries out this approach for two possible longitudes:

- $\alpha = 0$: low-cost transfer are available to $20,000 \leq A_z \leq 110,000$ km halo, with a transfer time of about 8 months. The analysis can be conducted as in Sec. **[3.2.1]**.
- $\alpha = \pi$: low-cost transfers are available to $270,000 \leq A_z \leq 640,000$ km halo, with a transfer time of about 4 months. The analysis can be conducted as in Sec. **[3.2]**.

4.3.4. Budget from GTO

As a refinement of the method proposed in Sec. **[4.3.2]** and Sec. **[4.3.3]**, we now directly compute the injection from a GTO to the manifold itself.

Assume a halo set such that $20,000 \leq A_z \leq 500,000$ km with step 10,000 km. Let us mesh each halo orbit into a 3600 sample and compute the eigeinpairs of their monodromy matrix $(\lambda_i, \mathbf{e_i})$. Considering ϵ a small displacement with respect to nominal halo orbit, $\mathbf{e}_{\lambda_{\mathbf{MIN}}}$ the eigenvector associated with the real eigenvalue less than 1, the HOI belonging to stable manifold from Earth domain are given by:

$$\mathbf{r_{HOI}} = \mathbf{r_{HALO}} - \epsilon \, \mathbf{e}_{\lambda_{\mathbf{MIN}}}$$

We propagate the initial condition $\mathbf{r_{HOI}}$ backward in time for 1 year or until Earth collision at 200 km altitude occurs. What is obtained is a sample pool of 3600 stable manifolds to same halo. These include trajectories reaching GEO altitude or lower. Along such trajectories a Transfer Trajectory Insertion from GTO can be computed.

By modelling the GTO parking orbit as in Sec. **[3.3]**, the insertion budget is evaluated along the trajectory and the minimum obtained. In Sec. **[3.3]** the minima were tabulated and the associated trajectories represented. What is done here is extend that analysis.

Figure **[4.15a]** summarizes the transfer strategy just described. At the TTI two angles (θ, β) are evaluated, respectively the true anomaly and the manoeuvre insertion angle. Since a variable altitude approach is set, instead of $(\alpha, \Delta\iota_z)$ the departure surface is define by the plane (θ, β).

In **[4.15b]** the budget is described as a function of the halo parameters $(\tau/T, A_z)$. Let us compare it with the arrival maps obtained at fixed 200 km altitude:

- The increased flexibility results in a drop of the budget peak, not in an improved minimum.
- Since the constraint on altitude is relaxed, there are more transfer opportunities. This results in an enlargement of the already identified transfer zones and in the presence of a new one.
- Despite their enlargement, the yet analysed transfer zone have almost unchanged efficient low-cost solutions. Indeed in dark blue are recognisable: one annular structure about small amplitude halo performing multiple Earth passage transfer; one ring structure about large amplitude performing direct transfer; a third zone that provide indirect transfer to large halo. That these solutions do not change is due to the fact that the efficient solutions are spontaneously close to the parking orbit pericentre, and therefore at the same altitude of the previous constraint.
- The new transfer zone is identified by two thin lines running almost parallel. Despite its small extension, the new area allows a transfer for halo $A_z \leq 460,000$ km. They are not efficient low-cost transfers, but for halo $150,000 \leq A_z \leq 260,000$ km they offer a decreasing insertion budget between 1.3 and 0.85 km/s. It's lower than that the one provided from the other enlarged transfer zone to the same A_z.
- According to the nomenclature introduced in Sec. **[3.3]**, the new zone allows Tour

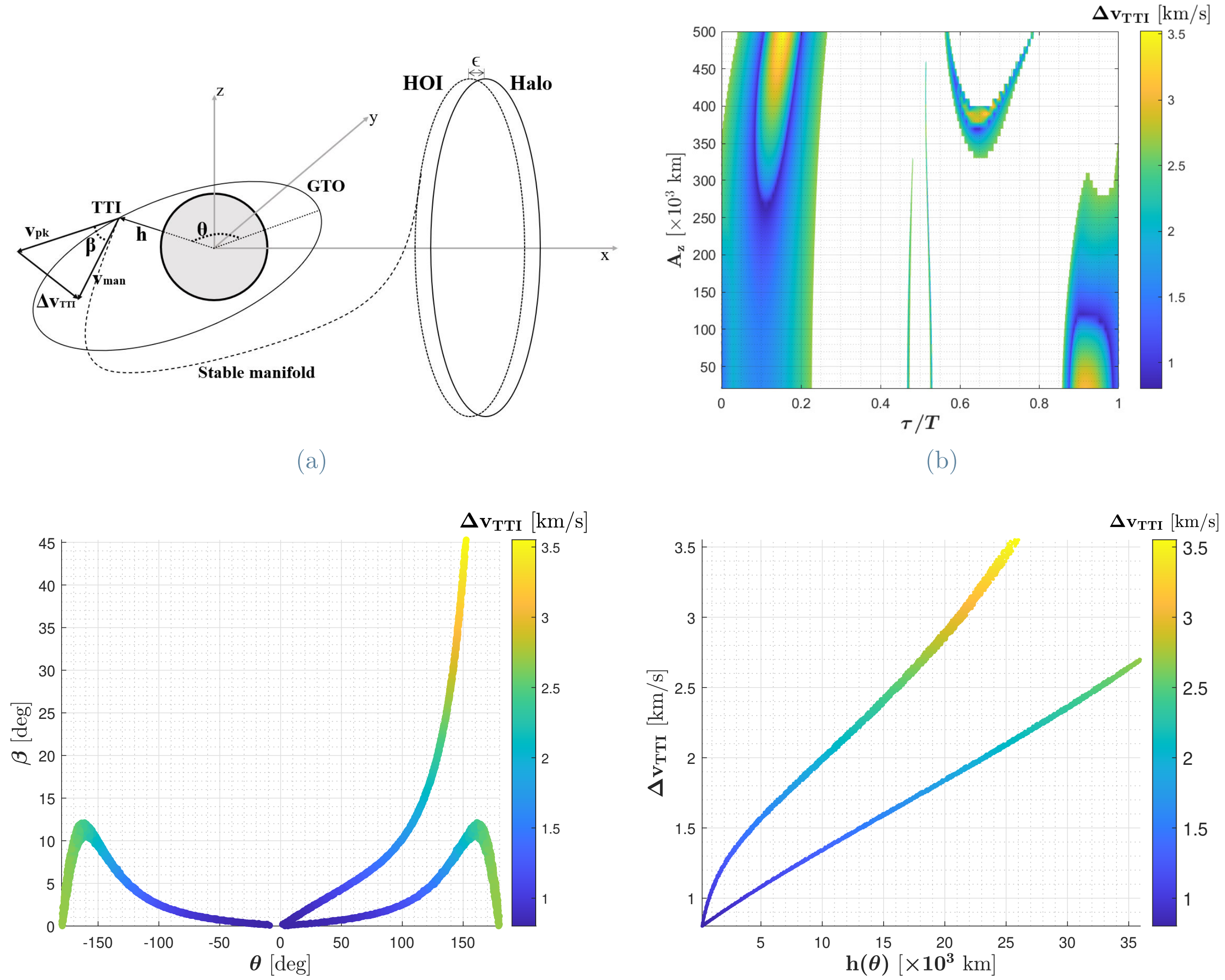

(a) (b)

(c) (d)

Figure 4.15: Parametric analysis from GTO to halo. **[4.15a]** sketch of the transfer design model from HOI backward in time to GTO. The color bar reports the budget. **[4.15b]** the arrival map: four transfer zones are defined, each one corresponding at a transfer type; efficient low-cost transfer are detected (dark blue). **[4.15c]** β versus θ. **[4.15d]** insertion budget versus TTI altitude h.

type transfer.

Figure **[4.15c]** interprets the insertion budget as a function of angles (θ, β). Note that:

- In the model the GTO shape is defined, but it's not imposed that the TTI occurs at the pericentre. However, low-cost transfers cluster at GTO pericentre.
- Both at pericenter and apocenter the β angle is almost zero, but the insertion budget at apocentre is three times higher than at the pericentre.
- β plays an outstanding role: a high value of the manoeuvre insertion angle implies an unsustainable exponential rise of the insertion budget.
- In order to keep Δv_{TTI} low a (θ, β) trade-off analysis could be object of investigation. To accept a small θ could keep β lower i.e., the budget. Indeed the most efficient solution is not at the pericentre, but at its surroundings.

In Fig. **[4.15d]** the insertion budget versus the altitude is shown. The plot shows two legs branching from the pericenter altitude. Note that whatever is the halo targeted, the insertion budget exhibits an uniform behaviour.

In Fig. **[4.16]** GTO with different pericentre altitude are compared. Note that:

- The lower is the pericentre, the lower is is the minimum insertion budget. Hence, it is better to have a TTI altitude as low as possible and a GTO with a pericentre just below.
- Setting GTO up to 500 km pericentre altitude, the performances are just slightly worse. It provides generality at the actual analysis.

So far, the entire solution space has been described, the analysis is now detailed on the selected minima. In Fig. **[4.17]** the minimum values are located on the arrival map and their performances summarized:

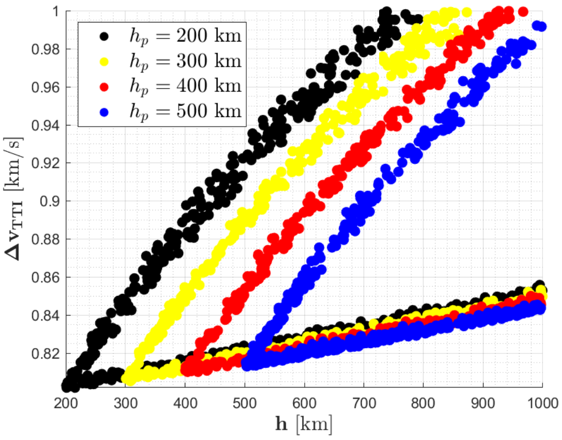

Figure 4.16: Comparison of the insertion budget Δv_{TTI} versus TTI altitude h for different GTO.

- The insertion budget does not appear to be the major driver for $A_z \leq 110,000$ km or $A_z \geq 270,000$ km, indeed the minimum Δv_{TTI} is about the same while the transfer time Δt halves.
- A lower transfer time doesn't implies a higher budget, or vice versa. Indeed, the graph shows solutions (1) with approximately the same budget but very different transfer times, or (2) high cost and long time.
- There are not efficient low-cost transfers serving halos $120,000 \leq A_z \leq 260,000$ km.
- Looking to the Δt colorbar the transfer type is clearly recognisable: yellow for multiple Earth passage; red for tour; blue for direct; cyan for indirect.

To conclude the analysis the time spent in eclipse and excluded zone is computed (Fig. **[4.18]**). Those are modelled has two trunks of cone, one with 14,000 km radius at SEL2, the other one with radius 90,000 km at SEL1 (Canalias Vila [2007]). It turns out that the eclipse is negligible for almost all the trajectories, consisting of only a few hours. In contrast, the time spent in the excluded zone can be not negligible for trajectories targeting small amplitude halos.

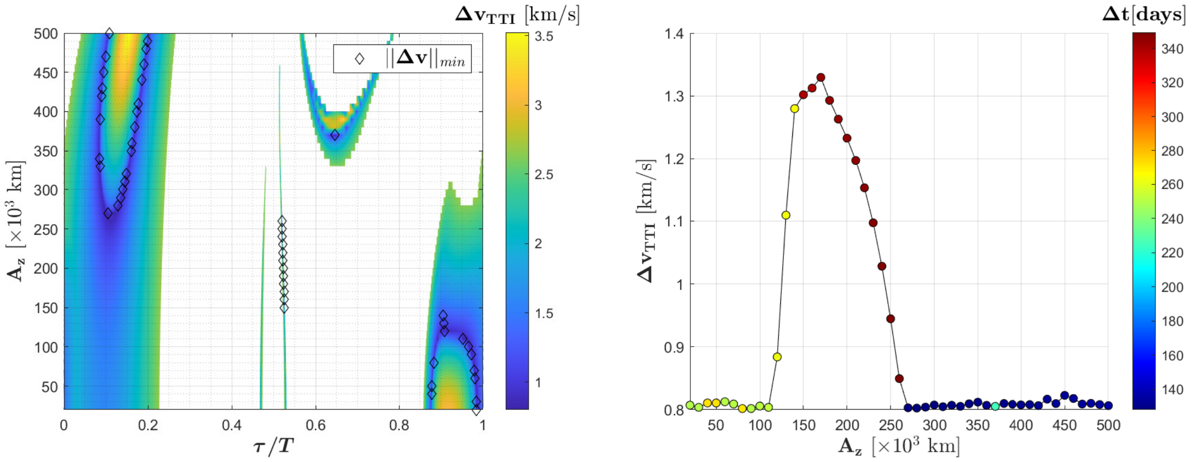

(a) (b)

Figure 4.17: Selected minima on the arrival map **[4.17a]**. In **[4.17a]** the minimum budget versus halo amplitude per transfer time.

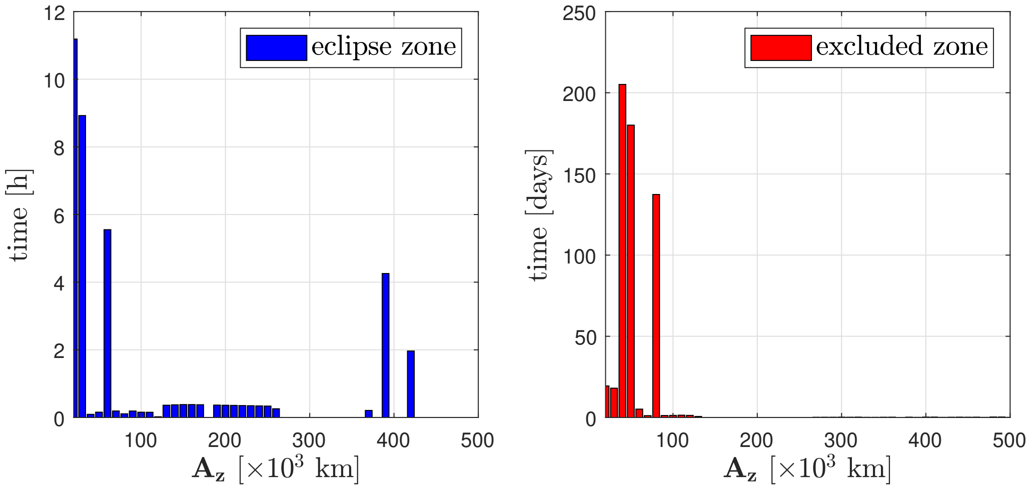

Figure 4.18: Transfer trajectory time in the eclipse zone projected by the Earth (left) and in the excluded zone between the Earth and L1 (right).

4.4. Transfer optimization

According to the parametric analysis performed so far two options can be considered for the preliminary design of the REMEC mission: the halo orbit of amplitude 30,000 km and the one of amplitude 280,000 km. Both operative orbit are eclipse free and allow an efficient low-cost transfer.

For small amplitude halos:

- Its low inclination angle Δi_z allows higher visibility from Earth.
- Its TTI fits better with Ariane 6 commercial GTO.
- In refined design stages the transfer is compatible with a Moon flyby, which benefits the budget and offers a secondary scientific mission.
- The impact of the excluded zone on the longevity of on-board electronics is not marginal but still acceptable.
- Deep space observations can begin only after the last Earth passage.
- Multiple Earth passages risks must be managed.
- The transfer trajectory is longer respect to second option, resulting in a potential greater commitment to correction manoeuvres.

For large amplitude halos:

- The direct transfer opportunities allow a short transfer time. Deep space observation can start during the transfer shortly after the launch.
- Robust transfer design.
- Marginal time in the excluded zone.
- Compatible with eclipse free trajectory.

4.4.1. In CR3BP

Results from the sample pool can provide a reference trajectory. In order to obtain a local optimal solution a multiple shooting transcription method is adopted. Main references for this topic are Betts [1998], Mingotti et al. [2011] and Topputo [2013]. The method is applied to the options selected in the previous section.

The objective function aims at minimizing the budget:

$$\min(||\mathbf{\Delta v_I}|| + ||\mathbf{\Delta v_{II}}||)$$

Where $\mathbf{\Delta v_I}$ is the manoeuvre from GTO pericenter to the transfer trajectory, and $\mathbf{\Delta v_{II}}$ is the manoeuvre from the transfer trajectory to the halo orbit insertion.

The control cariable are:

- τ halo parameter.
- Δt transfer time.
- $\Delta \mathbf{v_{II}}$ halo insertion manoeuvre.

The constraints are:

- halo amplitude A_z.
- Boundary conditions i.e.:

$$\mathbf{r}(t_0 + \Delta t) = \mathbf{r}(\tau)$$

$$||\mathbf{r}(t_0)|| = h_p$$

- altitude $h(t)$ higher than a minimum $\bar{h}$.

In Fig. **[4.19a]** the transfer model is summarized. The parking orbit is modelled as in Sec. **[4.3.2]**. In Tab. **[4.2]** same results is listed in budget order.

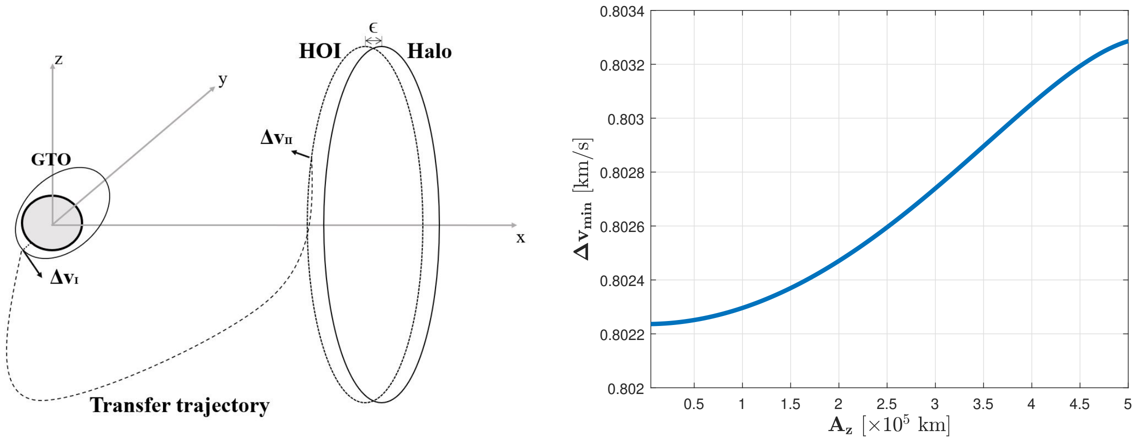

(a) (b)

Figure 4.19: Simple shooting transfer design. In **[4.19a]** sketch of the transfer design strategy from HOI backward in time to GTO pericenter. In **[4.19b]** minimum ideal budget versus targeted halo amplitude.

Table 4.2: CR3BP optimization

A_z [km]	Δv_I [km/s]	Δv_{II} [cm/s]	Δt [days]
30,000	0.802252	40.1809	249.7
280,000	0.805426	4.8830	128.3

The quality of the optimisation can be assessed by comparison with the ideal minimum budget given by Jacobi's constants (Fig.**[4.19b]**):

$$\Delta v_{min} = \sqrt{\mathrm{JC}_{GTO} - \mathrm{JC}_{HALO} + v_{GTO}^2} - v_{GTO} \tag{4.10}$$

4.4.2. In BR4BP

We now proceed to optimise in Bicircular Restricted 4 Body Problem (BR4BP) the trajectories obtained in CR3BP.

The Bicircular Restricted 4 Body Problem (Farquhar [1980]) is commonly used in literature to describe in a more realistic and accurate way the Sun-Earth+Moon system:

the Moon and the Earth are no more aggregated into a single celestial body, but placed on the ecliptic plane in circular motion around their barycentre (Fig. **[4.20a]**). The Moon orbit has eccentricity 0.055 and inclination over the ecliptic about 5.15 degrees, so the model is is based on some minor approximations. The price to pay for the BR4BP realism is twofold:

- A new variable ϕ_{EM} is introduced to describe the Earth-Moon location.

$$\phi_{EM} = \phi_{EM}(t_0) + n_2(t - t_0) \tag{4.11}$$

- The celestial bodies state is time-dependent.

$$\mathbf{x_E} = \begin{Bmatrix} 1 - \mu_1 - \rho_E \cos\phi_{EM} \\ -\rho_E \sin\phi_{EM} \\ 0 \\ \rho_E n_2 \sin\phi_{EM} \\ -\rho_E n_2 \cos\phi_{EM} \\ 0 \end{Bmatrix} \qquad \mathbf{x_M} = \begin{Bmatrix} 1 - \mu_1 + \rho_M \cos\phi_{EM} \\ \rho_M \sin\phi_{EM} \\ 0 \\ -\rho_M n_2 \sin\phi_{EM} \\ \rho_M n_2 \cos\phi_{EM} \\ 0 \end{Bmatrix} \tag{4.12}$$

$$\rho_E = \frac{\mathrm{EM}}{l_*}\frac{\mu_2}{\mu_1} \qquad \rho_M = \frac{\mathrm{EM}}{l_*}\left(1 - \frac{\mu_2}{\mu_1}\right) \tag{4.13}$$

Indeed, adopted the SB_{EM} CR3BP synodic reference system (with angular rate $n_1 = 1$) the Sun and the barycentre B_{EM} are motionless. Instead, the Earth-Moon system has angular rate n_2 in the synodic reference system of the SB_{EM} system:

$$n_2 = \frac{2\pi}{T_{EM}} - n_1 \rightarrow \tilde{T}_{EM} = \frac{2\pi}{n_2} \approx 29.53 \text{ days} \tag{4.14}$$

The introduction of the relative period $\tilde{T}_{EM}$ enhances the complexity of the mission design. The BR4BP provides periodic output related to the relative position Sun-Earth-

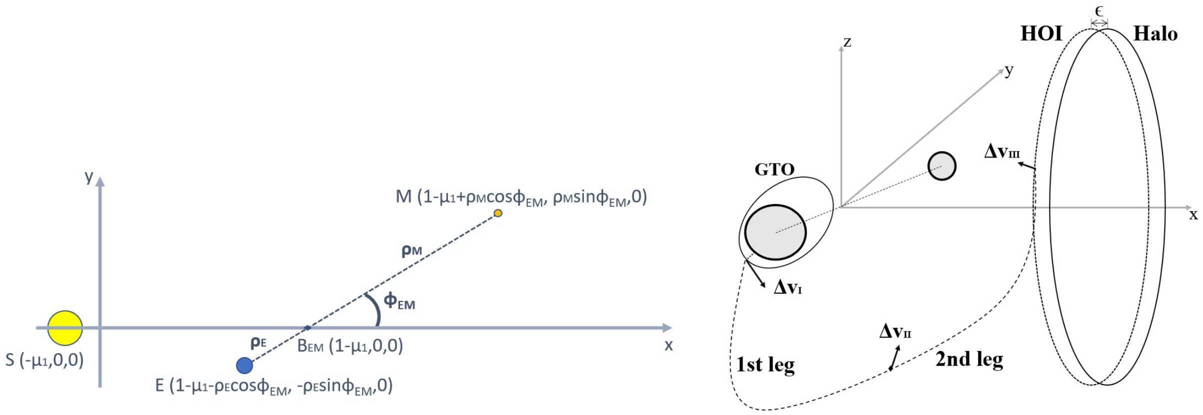

(a) (b)

Figure 4.20: BR4BP and Transfer trajectory. In **[4.23a]** sketch of the model view on the ecliptic plane: the Sun and the Earth-Moon barycentre B_{EM} are motionless on the x-axis while Earth-Moon move in a circular motion around their common barycenter, their position given by ϕ_{EM}. In **[4.23a]** draft of the transfer trajectory: the insertion from GTO pericenter; the correction manoeuvre Δv_{II} to insert the II leg; the insertion to HOI.

Moon such that date occurrence of the appropriate orientation must be considered.

BR4BP Equation of motion in Lagrangian form are:

$$\begin{cases} \dot{x} = v_x \\ \dot{y} = v_y \\ \dot{z} = v_z \\ \dot{v}_x = 2v_y + x - \frac{1-\mu_1}{r_S^3}(x+\mu_1) - \frac{\mu_1-\mu_2}{r_E^3}(x-x_E) - \frac{\mu_2}{r_M^3}(x-x_M) \\ \dot{v}_y = -2v_x + y - \frac{1-\mu_1}{r_S^3}y - \frac{\mu_1-\mu_2}{r_E^3}(y-y_E) - \frac{\mu_2}{r_M^3}(y-y_M) \\ \dot{v}_z = -\frac{1-\mu_1}{r_S^3}z - \frac{\mu_1-\mu_2}{r_E^3}z - \frac{\mu_2}{r_M^3}z \\ \dot{\Phi}_{EM} = n_2 \end{cases} \tag{4.15}$$

The parking orbit can be modelled as in Sec. **[4.3.2]** taking in account the Earth velocity

$\mathbf{v_E}$, such that instead of Eq. **[4.9]** it is used:

$$\mathbf{v_{pk}} = \tilde{\mathbf{v}}_{\mathbf{pk}} + (-\mathbf{n_1}) \times \mathbf{r} + \mathbf{v_E} \tag{4.16}$$

To add flexibility, the transfer trajectory is split in two legs (Fig.**[4.20b]**): one from GTO pericentre and the other from HOI. The reference trajectory is provided by CR3BP.

The objective function is:

$$\min \sum_{i}^{3} ||\mathbf{\Delta v_i}||$$

Where manoeuvres $\mathbf{\Delta v_I}, \mathbf{\Delta v_{II}}, \mathbf{\Delta v_{III}}$ are detailed in Fig. **[4.20b]**.

The control variables are:

- halo parameter τ.
- first leg transfer time $\Delta t_{I,II}$.
- second leg transfer time $\Delta t_{II,III}$.
- halo insertion manoeuvre $\Delta \mathbf{v_{III}}$.
- Transfer correction manoeuvre $\Delta \mathbf{v_{II}}$.
- The Earth-Moon location $\phi_{EM}(t_0)$.

The constraints are:

- halo amplitude A_z.

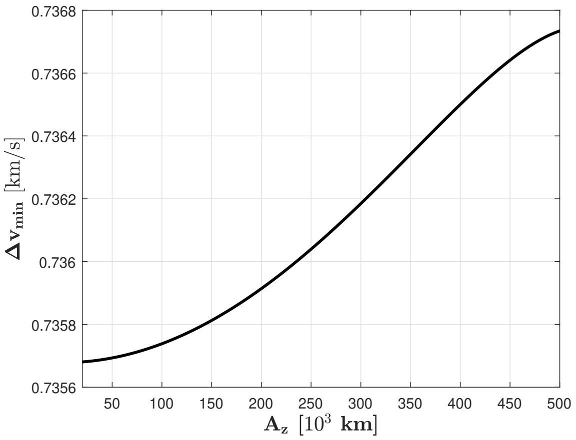

Figure 4.21: Guessed budget for a Earth-to-SEL2 halo transfer trajectory in BR4BP: the budget on the y-axis and on x-axis the halo amplitude.

- Boundary conditions i.e.:

$$\mathbf{r}(t_{III}) = \mathbf{r}(\tau)$$
$$||\mathbf{r}(t_I)|| = h_p$$
$$||\mathbf{r}(t_{II}^-)|| = ||\mathbf{r}(t_{II}^+)||$$
$$||\phi(t_{II}^-)|| = ||\phi(t_{II}^+)||$$

- altitude from Earth h_E and altitude from Moon h_M higher than a minimum altitude, respectively $\bar{h}_E$ and $\bar{h}_M$.

By means of Eq. **[4.10]**, a BR4BP budget can be computed, as shown in FIg. **[4.21]**, assuming:

$$JC = -2E \qquad E = K + U$$
$$K = \frac{1}{2}||\mathbf{v}||^2$$
$$U = -\frac{1}{2}(x^2 + y^2) - \frac{1-\mu_1}{||\mathbf{r_S}||} - \frac{\mu_1 - \mu_2}{||\mathbf{r_E}||} - \frac{\mu_2}{||\mathbf{r_M}||}$$

Since there is no integral of motion in the BR4BP[5], this formulation is a first guess. In Tab. **[4.3]** results are listed in budget order.

---

[5] Poincaré classification of BR4BP model proved its non-integrability (Poincaré [1892, 1893, 1899]).

Table 4.3: BR4BP optimization

A_z [km]	Δv_I [km/s]	Δv_{II} [m/s]	Δv_{III} [m/s]	Δt [days]	$\phi_{EM}(t_0)$ [deg]
30,000	0.705787	2.426671	1.441203	234.75	192.87
280,000	0.735978	0.219595	0.264546	126.82	158.61
30,000	0.739011	0.582239	0.209392	219.50	18.80

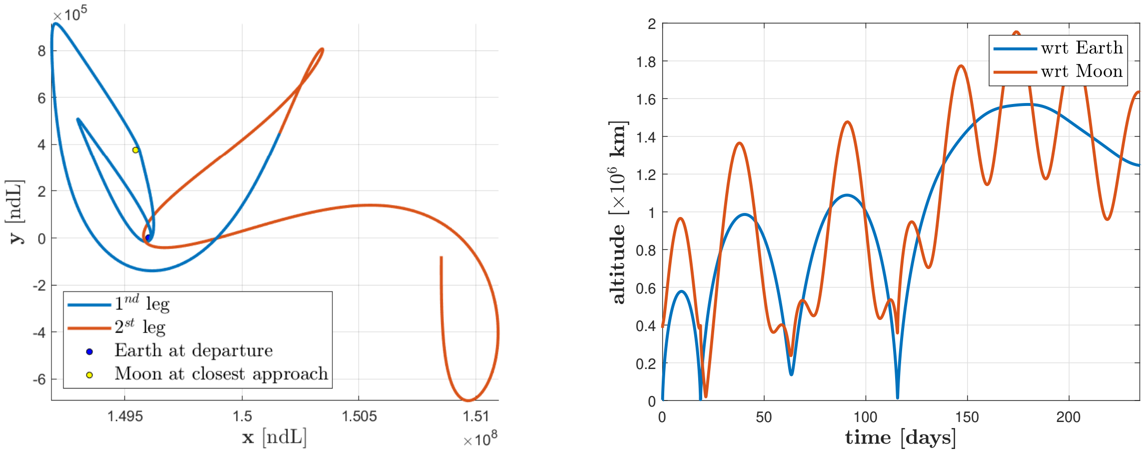

(a) (b)

Figure 4.22: Transfer Trajectory Earth-to-L2 Halo exploiting Moon gravity in BR4BP. On the right, view of the path on the x-y plane, on the opposite side the altitude respect to Earth and Moon versus the transfer time: from GTO pericentre the s/c moves along an high elliptical obit; to second orbit revolution the Moon is at 19,544 km altitude; later, an Earth second passage at 13,149 km altitude occurs.

The second and third transfer costs are within expectations, but not the first. Indeed, exploiting the additional degree of freedom ϕ_{EM} is performed a Moon gravity assist manoeuvre (Fig.**[4.22]**): not only is the minimum expected budget noticeably lower, but an additional benefit can be achieved by flyby manoeuvres. In conclusion, the BR4BP is both a more realistic and a less conservative approach at mission design than the CR3BP.

4.5. Disposal from SEL2-halo

In this section a brief analysis hint to End-of-Life (EoL) budget is done for completeness. From SEL2-halo orbit the strategy adopted here is to target a disposal orbit in the exterior interplanetary domain. The design trade-off is between chemical propulsion or Solar

Radiation Pressure (SRP) thrust (Colombo et al. [2014]). It should be noted that the EoL profile discussed is generally applicable, but not necessarily the most efficient. Especially for large halos, a return to Earth via direct transfer might be preferred. For more details Alessi [2015].

4.5.1. CR3BP Impulsive EoL Design

The EoL can be designed through 4 steps:

- **Decommissioning Countdown**: Its activation irreversibly establishes the residual duration of the operational phase. As the countdown begins, the s/c leaves the operational orbit and inserts into the decommissioning trajectory. The deviation between the operational orbit and the decommissioning trajectory is negligible at this stage. The countdown starts performing a fist decommissioning manoeuvre Δv^0_{EoL} according to a low-cost or short-term strategy, such as:
  - In about 8 months and 1 cm/s Δv^0_{EoL} budget the spacecraft inserts the unstable manifold towards the exterior interplanetary space.
  - In about 3 months and 10 m/s Δv^0_{EoL} budget. This strategy is recommended in preliminary design in order to keep a conservative approach.
- **Frozen Mode**: At the end of the science mode the s/c remains in standby for a time Δt_{EoL}. Only service systems to ensure survival remain in place.
- **EoL Manouevre**: Hill's forbidden zone is enlarged up to close SEL2 access. Hence, under CR3BP assumption it is guarantee that the s/c cannot return to the Earth domain. The required budget can be roughly estimated as:

$$\Delta v_{EoL} = v_{EoL} - \sqrt{JC_{EoL} - JC_{L2} + v^2_{EoL}} \tag{4.17}$$

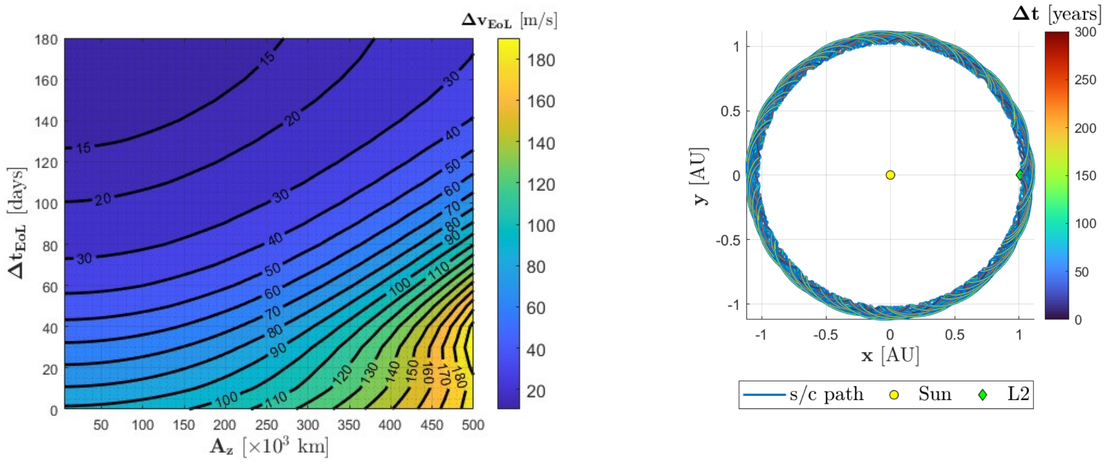

(a) (b)

Figure 4.23: EoL Design. In **[4.23a]** the time versus budget trade-off: on the y-axis the time Δt_{EoL} between the end of the science phase and the performing of the EoL manoeuvrre; on the x-axis the halo amplitude A_z; on colorbar the required EoL budget Δv_{EoL} of the impulsive manoeuvre to close the access to Sun Earth L2. In **[4.23a]** solar sailing application at EoL design in SRP+BR3BP model: the s/c motion is propagated for a time span of 300 years to prove that it doesn't return in the Earth domain.

In Fig. **[4.23a]** it is provided a trade-off analysis between the time in frozen mode Δt_{EoL} and the EoL budget Δv_{EoL} versus the halo amplitude A_z. For instance, an immediate performance requires 0.090 to 0.190 km/s, after two months the EoL budget is between 0.040 and 0.150 km/s, while after 4 months the same result is achived with 0.015 up to 0.050 km/s. In conclusion, the selection is linked to on-board performances. It is remarkable that the budget drops rapidly to 0.050 km/s, then it continues to decrease but much slowly. It could therefore be a design choice to perform the manoeuvre at 0.050 km/s and adjust the requirements of the on-board systems accordingly.

- **Disposal Mode**: All end-of-life activities on board and on ground have been carried out and the mission ends.

4.5.2. BR4BP-SRP EoL Design

Halos are unstable orbits at the edge of interplanetary space subject to environmental perturbations: Solar Radiation Pressure (SRP); Gravity Gradient (GG); Magnetic Field

(MF). Between them, the literature is unanimous in highlight the preeminent role of the SRP in deep space. Studies on the effects of solar radiation on small bodies date back to the early 1900s (Poynting [1904]). In Schuerman [1980] the SRP effect is embedded in the CR3BP equation of motion, and Elipe [1992] computes the three collinear Lagrangian points taking account of SRP. The applications of SRP to mission design are detailed in McInnes [2004].

On bodies smaller than 1 mm the SRP effect results in a loss of angular momentum, and consequently in a spiral motion towards the own star (Poynting-Robertson effect). For larger bodies, according to cannonball model (Soldini [2016]) the SRP consists of a continuous outgoing action inversely proportional to the quadratic Sun distance r_S and directly proportional to the area-to-mass ratio A_S/m.

$$\dot{\mathbf{v}}_{\mathbf{SRP}} = \frac{P_{1AU}}{||\mathbf{r_S}||^3} c_R \frac{A_S}{m} \mathbf{r_S} \qquad\qquad P_{1AU} = 4.57 \cdot 10^{-3} \frac{\text{kg}}{\text{km s}^2}$$

$$c_R = 2$$

For illustrative purposes it is carried out a simulation in BR4BP with area-to-mass ratio 3 dm^2/kg. The spacecraft motion is propagated for 300 years from halo A_z 280,000 km. As shown in Fig. **[4.23b]** the s/c leaves the halo orbit for the exterior domain and in the time span doesn't return to the Earth domain. Note that the disposal orbit is very close to a zero velocity curve, with an average velocity of 2.95 km/s.

4.6. Conclusions

In Tab. **[4.4]** is roughly sketched a preliminary budget baseline under the assumption of CR3BP. Given the preliminary design phase, it is assumed a +25% design factor. Hence, the total preliminary budget $\Delta v_{TOT}^{0.25}$ is:

$$\Delta v_{TOT}^{0.25} = 1.25\ \Delta v_{TOT} \geq 1.25\ \Delta v_{TTI} \tag{4.18}$$

A_z	Δv_i	Δv_ω	Δv_{TTI}	Δv^0_{EoL}	Δv_{EoL}	Δv_{TOT}	$\Delta v^{0.25\%}_{TOT}$
Small	≤ 0.06	≤ 0.06	≤ 0.82	≤ 0.01	≤ 0.10	≤ 1.05	≤ 1.31
Medium	≤ 0.06	≤ 0.06	≤ 1.33	≤ 0.01	≤ 0.12	≤ 1.58	≤ 1.98
Large	≤ 0.06	≤ 0.06	≤ 0.82	≤ 0.01	≤ 0.19	≤ 1.14	≤ 1.43

NOTEs:
Velocities are given in km/s.
Small halo for $+A_z \leq 110{,}000$ km.
Medium halo for $120{,}000 \leq +A_z \leq 260{,}000$ km.
Large halo for $270{,}000 \leq +A_z \leq 500{,}000$ km.
All velocities in km/s.
Δv_i assumed GTO correction $\delta i_z \leq 3.0$ deg.
Δv_ω assumed GTO correction $\delta\omega \leq 3.0$ deg.
$\Delta v_h \approx 0.00$ km/s for GTO pericenter altitude correction $\delta h \leq 10$ km.
$\Delta v_{HOI} \approx 0.00$ km/s.
GTO rephasing, transfer corrections, station keeping and halo-to-halo service transfer are not accounted.
The total preliminary budget $\Delta v^{0.25}_{TOT}$ is the total budget Δv_{TOT} increased by a 25% factor due to preliminary phase of design.

Table 4.4: GTO Budget Baseline

The minimum insertion budget is 0.8 km/s and any other cost is a Δv_{TTI} fraction, hence by Eq.**[4.18]**:

$$\min\left(\Delta v^{0.25}_{TOT}\right) \geq 1.00 \quad \text{km/s} \tag{4.19}$$

Efficient low-cost transfer trajectories targeting small and large amplitude halos are both possible. Low-cost transfers to medium amplitude halos are still available, but not efficient.

For $20,000 \leq A_z \leq 110,000$ halos have better performance in terms of inclination angle $\Delta\iota_z$ and Earth distance r_E. However, the transfer path shows multiple Earth passage, longer transfer time, and excluded zone permanence.

For $270,000 \leq A_z \leq 500,000$ the transfer trajectory is robustness and almost eclipse/excluded zone free.

The research activity is mainly dedicated to the transfer from Earth, but an end-of-life phase strategy is also profiled, which is the second contribution in terms of budget. A further analysis of the transfers presented would be interesting, however the next main investigation opportunity would concern trade-offs between different disposal strategies, and between halo-to-halo service transfers and station keeping.

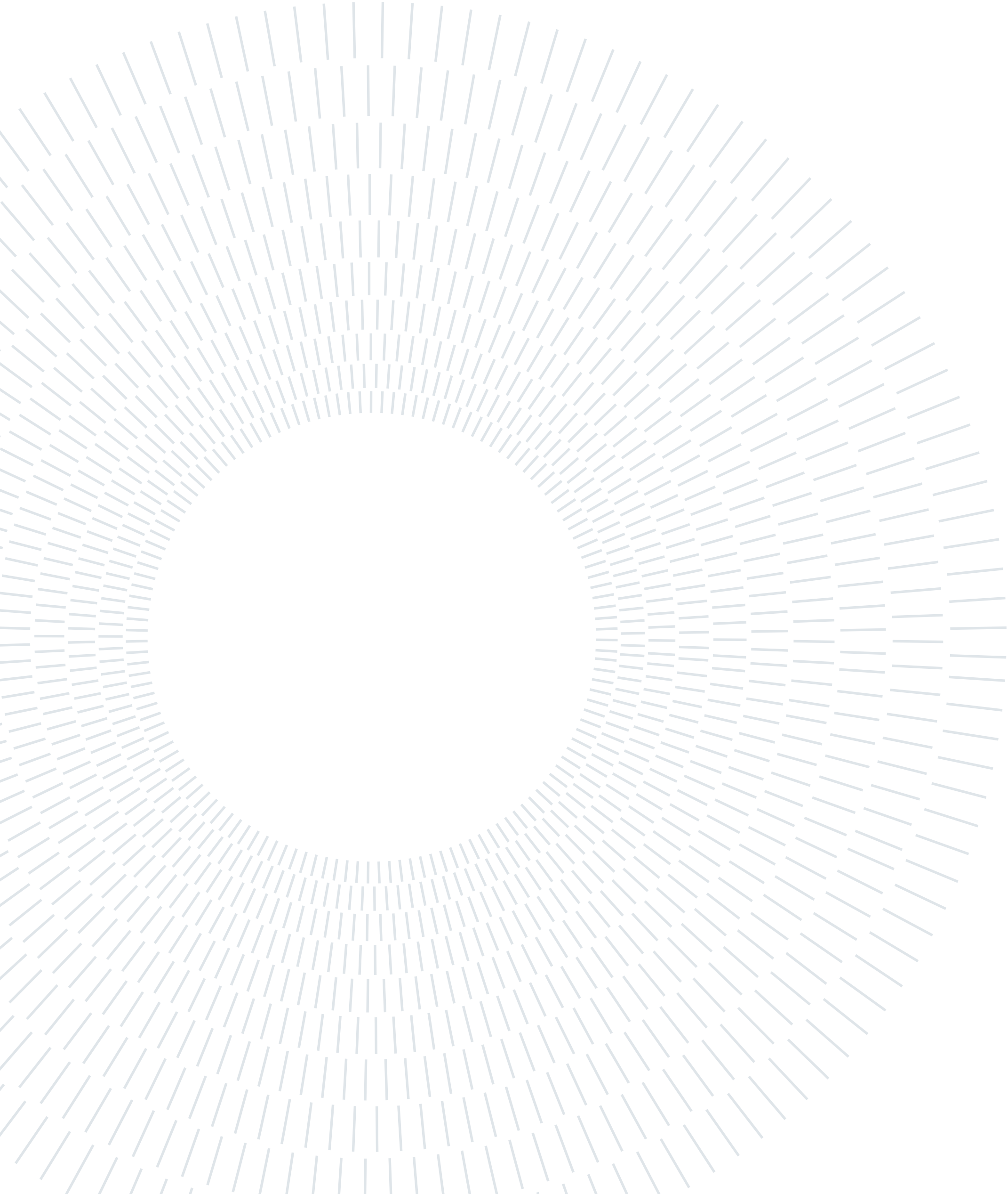

5 | Conclusions

The thesis produces a parametric study to design both the operational orbit and the transfer trajectory in a large family of possible orbits considering Δv cost, coverage, visibility constraints.

The parametric analysis supports the preliminary design of a SEL2-halo space mission. The investigation is conducted in the CR3BP, which offers a conservative approach and timeline independence. The parametric analysis is based on multiple Libration orbit amplitude which would offer a tool for fast mission analysis considerations.

Given a commercial, hence non-dedicated launch, the pericentre of the parking orbit in ecliptic coordinates is constrained. Starting from this data, a parametric approach based on the use of the Poincaré section is explored. The driver of a baseline budget is the manifold insertion cost. Several transferring strategy to SEL2 halo are proposed. The description plays with different parking orbits (LEO, GTO) and insertion design to obtain a budget baseline versus altitude.

Having a launch that leads to a dedicated GTO, selected according to the nominal halo orbit, that satisfies well-defined payload requirements. In such a case, the analysis begins with a trade-off analysis between halo performance in terms of reliability and operability. Once a number of profiles have been defined and their trade-offs established, one has a good guess for the optimisation algorithms.

The research activity is mainly dedicated to the transfer from Earth, but an end-of-life phase strategy is also profiled, which is the second contribution in terms of budget. A further analysis of the transfers presented would be interesting, however the next main investigation opportunity would concern trade-offs between different disposal strategies, and between halo-to-halo service transfers and station keeping.

List of Figures

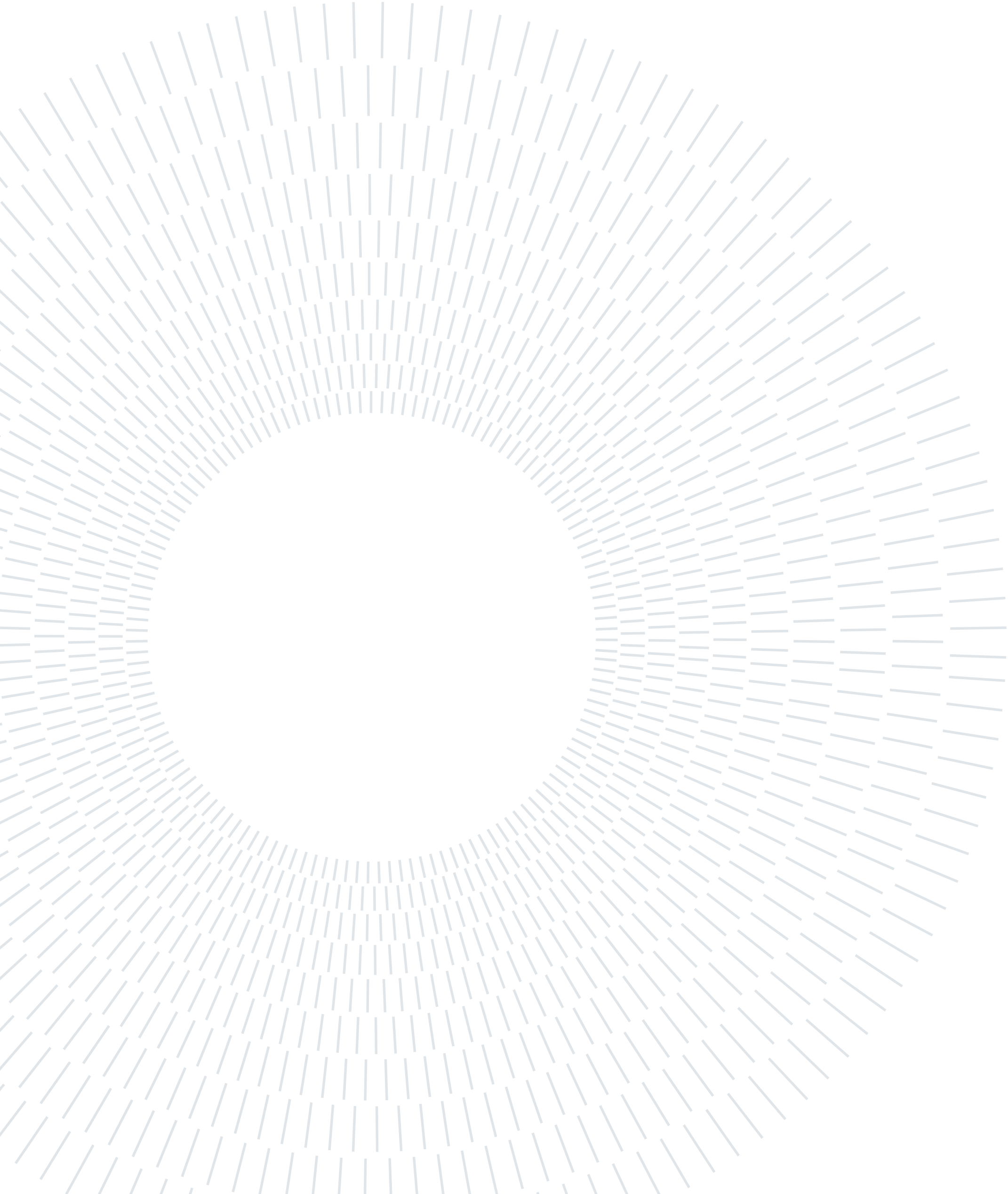

List of Tables

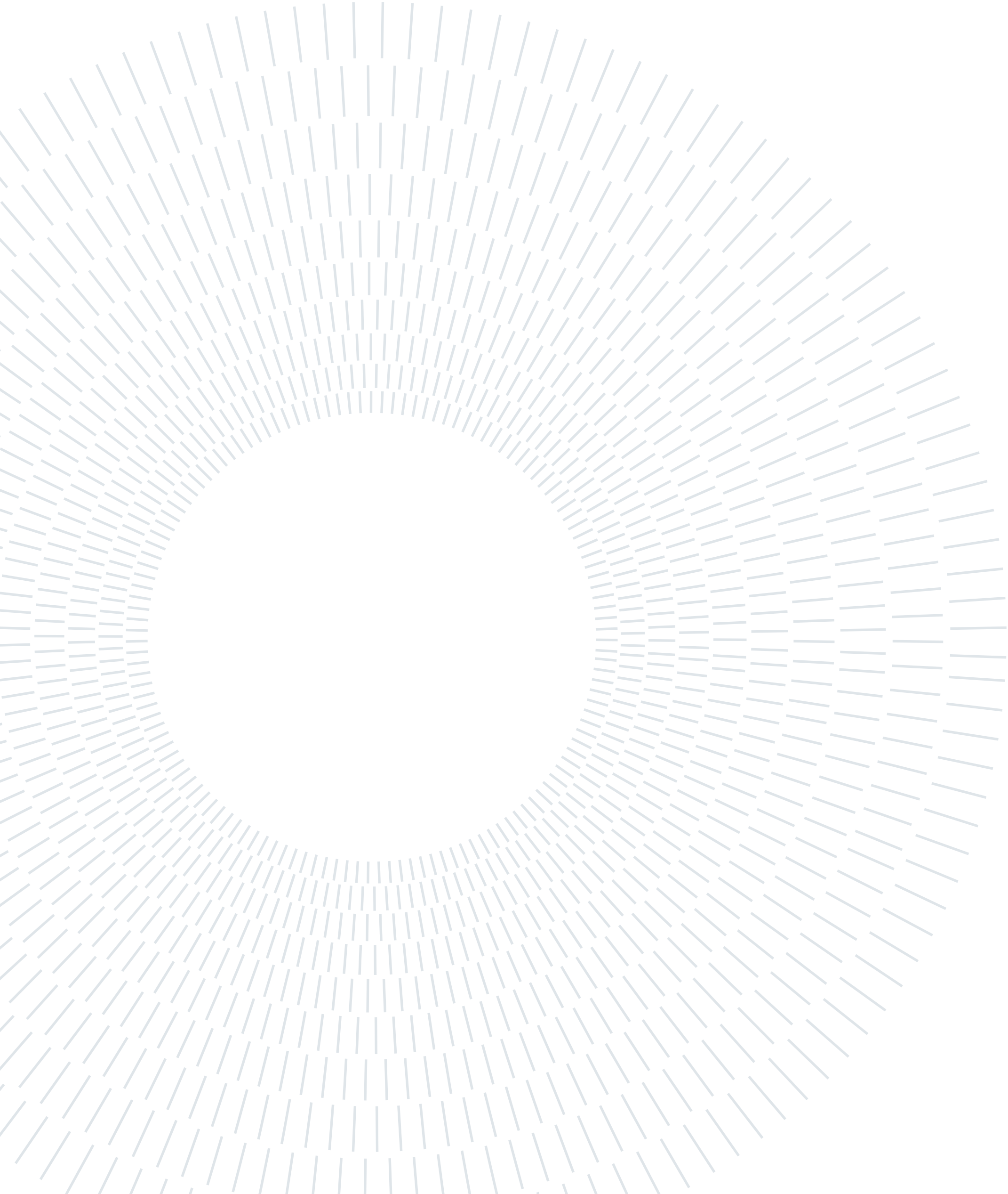

Bibliography

A. Aguilar, R. Filgas, C. Colombo, E. M. Alessi, M. Lo Iacono, E. Arikan, and M. e. a. Bolis. The remec mission: Mission concept and architecture feasibility assessment. *D2.6, European Space Agency contract*, 04/2023.

E. M. Alessi. The reentry to earth as a valuable option at the end-of-life of libration point orbit missions. *Advances in Space Research*, 55(12):2914–2930, 2015.

J. E. Allnutt. Satellite-to-ground radiowave propagation-theory, practice and system impact at frequencies above 1 ghz. *Stevenage Herts England Peter Peregrinus Ltd IEE Electromagnetic Waves Series*, 29, 1989.

R. L. Anderson and M. W. Lo. Role of invariant manifolds in low-thrust trajectory design. *Journal of guidance, control, and dynamics*, 32(6):1921–1930, 2009.

B. T. Barden. Using stable manifolds to generate transfers in the circular restricted problem of three bodies. *Master degree thesis. West Lafayette: School of Aeronautics and Astronautics, Purdue University*, 1994.

R. Bate, D. Mueller, J. White, and W. Saylor. *Fundamentals of Astrodynamics*. Dover Publications, 2020.

F. Bernelli, F. Topputo, and M. Massari. Assessment of mission design including utilization of libration points and weak stability boundaries. *ESA ACT Report*, 2004.

J. T. Betts. Survey of numerical methods for trajectory optimization. *Journal of guidance, control, and dynamics*, 21(2):193–207, 1998.

J. T. Betts. *Practical methods for optimal control and estimation using nonlinear programming*. SIAM, 2010.

D. Canales, K. Howell, and E. Fantino. Using finite-time lyapunov exponent maps for planetary moon-tour design. In *AAS 21-625, 2021 AAS/AIAA Astrodynamics Specialist Conference, Big Sky (Virtual)*, 2021.

E. Canalias, G. Gomez, M. Marcote, and J. Masdemont. Assessment of mission design including utilization of libration points and weak stability boundaries. *ESA Advanced Concept Team*, 2004.

E. Canalias Vila. *Contributions to libration orbit mission design using hyperbolic invariant manifolds*. Universitat Politècnica de Catalunya, 2007.

C. Colombo, F. Letizia, S. Soldini, H. Lewis, E. M. Alessi, A. Rossi, M. Vasile, M. Vetrisano, and V. der Weg W. End-of-life disposal concepts for lagrange-point and highly elliptical orbit missions. version 2.0 – 22 december. *Final Report, ESA/ESOC contract No. 4000107624/13/F/MOS*, 2014.

C. Conley. Low energy transit orbits in the restricted three-body problems. *SIAM Journal on Applied Mathematics*, 16(4):732–746, 1968.

K. Connor Howell. Three-dimensional, periodic,'halo'orbits. *Celestial mechanics*, 32(1): 53–71, 1984.

H. D. Curtis. *Orbital Mechanics for Engineering Students*. Elsevier Butterworth Heinemann, 2005.

D. Davis, S. Bhatt, K. Howell, J.-W. Jang, R. Whitley, F. Clark, D. Guzzetti, E. Zimovan, and G. Barton. Orbit maintenance and navigation of human spacecraft at cislunar near rectilinear halo orbits. In *AAS/AIAA Space Flight Mechanics Meeting*, number JSC-CN-38626, 2017.

A. Deprit and J. Henrard. Natural families of periodic orbits. Technical report, BOEING

SCIENTIFIC RESEARCH LABS SEATTLE WA MATHEMATICS RESEARCH LAB, 1966.

A. Deprit and J. Price. The computation of characteristic exponents in the planar restricted problem of three bodies. Technical report, BOEING SCIENTIFIC RESEARCH LABS SEATTLE WA MATHEMATICS RESEARCH LAB, 1965.

D. J. Dichmann, R. Lebois, and J. P. Carrico. Dynamics of orbits near 3: 1 resonance in the earth-moon system. *The Journal of the Astronautical Sciences*, 60:51–86, 2013.

E. J. Doedel, V. A. Romanov, R. C. Paffenroth, H. B. Keller, D. J. Dichmann, J. Galán-Vioque, and A. Vanderbauwhede. Elemental periodic orbits associated with the libration points in the circular restricted 3-body problem. *International Journal of Bifurcation and Chaos*, 17(08):2625–2677, 2007.

A. Elipe. On the restricted three-body problem with generalized forces. *Astrophysics and space science*, 188:257–269, 1992.

L. Euler. De moto rectilineo trium corporum se mutuo attrahentium. *Novo Comm. Acad. Sci. Imp. Petrop.*, 11:144–151, 1767.

R. W. Farquhar. Station-keeping in the vicinity of collinear libration points with an application to a lunar communications problem. Technical report, 1966.

R. W. Farquhar. Utilization of multi-body trajectories in the sun-earth-moon system. Technical report, 1980.

R. W. Farquhar and A. A. Kamel. Quasi-periodic orbits about the translunar libration point. *Celestial mechanics*, 7(4):458–473, 1973.

A. Farres, C. Webster, and D. Folta. High fidelity modeling of srp and its effect on the relative motion of starshade and wfirst. In *2018 Space Flight Mechanics Meeting*, page 2227, 2018.

G. Gómez. *Dynamics and mission design near libration points*. World Scientific, 2001.

D. Grebow. Generating periodic orbits in the circular restricted three-body problem with applications to lunar south pole coverage. *MSAA Thesis, School of Aeronautics and Astronautics, Purdue University*, pages 1–165, 2006.

M. Hazumi, P. A. Ade, A. Adler, E. Allys, K. Arnold, D. Auguste, J. Aumont, R. Aurlien, J. Austermann, C. Baccigalupi, et al. Litebird satellite: Jaxa's new strategic l-class mission for all-sky surveys of cosmic microwave background polarization. In *Space Telescopes and Instrumentation 2020: Optical, Infrared, and Millimeter Wave*, volume 11443, pages 431–450. SPIE, 2020.

M. Hénon. Exploration numérique du problème restreint. ii. masses égales, stabilité des orbites périodiques. In *Annales d'Astrophysique*, volume 28, page 992, 1965.

M. Hénon. Families of periodic orbits in the three-body problem. *Celestial Mechanics*, 10 (3):375–388, 1974.

M. Hénon. *Generating families in the restricted three-body problem*, volume I. Springer Science & Business Media, 1997.

M. Henon. New families of periodic orbits in hill's problem of three bodies. *Celestial Mechanics and Dynamical Astronomy*, 85(3):223–246, 2003.

M. Henon and F. Lutze. Generating families in the restricted three-body problem, ii: Quantitative study of bifurcations. lecture notes in physics, vol ii. *Appl. Mech. Rev.*, 55(6):B107–B107, 2002.

E. Herrera-Sucarrat, P. Palmer, and R. Roberts. Asteroid observation and landing trajectories using invariant manifolds. *Journal of Guidance, Control, and Dynamics*, 37 (3):907–920, 2014.

G. W. Hill. *On the Part of the Motion of Lunar Perigee Which is a Function of the Mean Motions of the Sum and Moon.* John Wilson Son, Cambridge, MA, 1877.

H.-W. Hsu, F. Crary, J. Parker, I. de Pater, G. Holsclaw, J. Pitman, K. Sayanagi, N. Altobelli, F. Bagenal, T. M. Becker, et al. Jupiter system observatory at sun-jupiter lagrangian point one. *Bulletin of the American Astronomical Society*, 53(4):358, 2021.

J. C. Jacobi. Sur l'elimination des noeuds dans le probl´eme des trois corps. *Journal fur die Reine und Angewandte Mathematik*, 26:115–131, 1843.

W. Koon, M. Lo, J. Marsden, and S. Ross. *Dynamical Systems, the Three-Body Problem, and Space Mission Design.* 2011.

L. Lagrange. Essai sur le probléme des trois corps. *Euvres*, 6:229–331, 1772.

C. R. McInnes. *Solar sailing: technology, dynamics and mission applications.* Springer Science & Business Media, 2004.

J. K. Miller and E. A. Belbruno. A method for the construction of a lunar transfer trajectory using ballistic capture. *Spaceflight mechanics 1991*, pages 97–109, 1991.

G. Mingotti, F. Topputo, and F. Bernelli-Zazzera. Optimal low-thrust invariant manifold trajectories via attainable sets. *Journal of guidance, control, and dynamics*, 34(6): 1644–1656, 2011.

Z. Musielak and B. Quarles. The three-body problem. *Reports on Progress in Physics*, 77, 2014.

I. Newton. *Philosophiœ naturalis principia mathematica.* Royal Soc. Press, London, 1687.

J. Ojeda Romero and K. C. Howell. Transfers from geosynchronous transfer orbits to sun-earth libration point trajectories. *The Journal of the Astronautical Sciences*, 69(2): 251–283, 2022.

T. S. Parker and L. Chua. *Practical numerical algorithms for chaotic systems.* Springer Science & Business Media, 2012.

T. A. Pavlak. *Mission design applications in the earth-moon system: Transfer trajectories and station keeping.* PhD thesis, Purdue University, 2010.

E. Perdios, C. Zagouras, and O. Ragos. Three-dimensional bifurcations of periodic solutions around the triangular equilibrium points of the restricted three-body problem. *Celestial Mechanics and Dynamical Astronomy*, 51(4):349–362, 1991.

P. Pergola and E. Alessi. Libration point orbit characterization in the earth–moon system. *Monthly Notices of the Royal Astronomical Society*, 426(2):1212–1222, 2012.

H. Poincaré. *Les méthodes nouvelles de la mécanique céleste.* Gauthier-Villars, 1892, 1893, 1899.

J. H. Poynting. Xii. radiation in the solar system: its effect on temperature and its pressure on small bodies. *Philosophical Transactions of the Royal Society of London. Series A, Containing Papers of a Mathematical or Physical Character*, 202(346-358): 525–552, 1904.

L. Puig, G. Pilbratt, A. Heske, I. Escudero, P.-E. Crouzet, B. de Vogeleer, K. Symonds, R. Kohley, P. Drossart, P. Eccleston, et al. The phase a study of the esa m4 mission candidate ariel. *Experimental Astronomy*, 46(1):211–239, 2018.

R. R. Rausch. Earth to halo orbit transfer trajectories. *Master of Science Thesis, Purdue University, Indiana*, 2005.

D. Richardson. Analytical construction of unstable periodic orbits about the collinear points. *Instabilities in Dynamical Systems. Applications to Celestial Mechanics*, 47: 302, 1979.

J. P. Sanchez and D. G. Yárnoz. Asteroid retrieval missions enabled by invariant manifold dynamics. *Acta Astronautica*, 127:667–677, 2016.

D. W. Schuerman. The restricted three-body problem including radiation pressure. *The Astrophysical Journal*, 238:337–342, 1980.

S. Soldini. *Design and control of solar radiation pressure assisted missions in the sun-earth restricted three-body problem.* PhD thesis, University of Southampton, 2016.

E. Strömgren. Connaissance actuelle des orbites dans le problème des trois corps', publications and minor communications of copenhagen observatory, publications 100. *Copenhagen University, Astronomical Observatory, Denmark*, 1935.

V. Szebehely. *Theory of Orbits: The Restricted Problem of Three Bodies*. Academic Press, New York, 1967.

X. Tang and A. Boozer. Finite time lyapunov exponent and advection-diffusion equation. *Physica D: Nonlinear Phenomena*, 95(3):283–305, 1996. ISSN 0167-2789. doi: https://doi.org/10.1016/0167-2789(96)00064-4. URL `https://www.sciencedirect.com/science/article/pii/0167278996000644`.

F. Topputo. On optimal two-impulse earth–moon transfers in a four-body model. *Celestial Mechanics and Dynamical Astronomy*, 117:279–313, 2013.

E. M. Zimovan-Spreen, K. C. Howell, and D. C. Davis. Near rectilinear halo orbits and nearby higher-period dynamical structures: orbital stability and resonance properties. *Celestial Mechanics and Dynamical Astronomy*, 132(5):28, 2020.

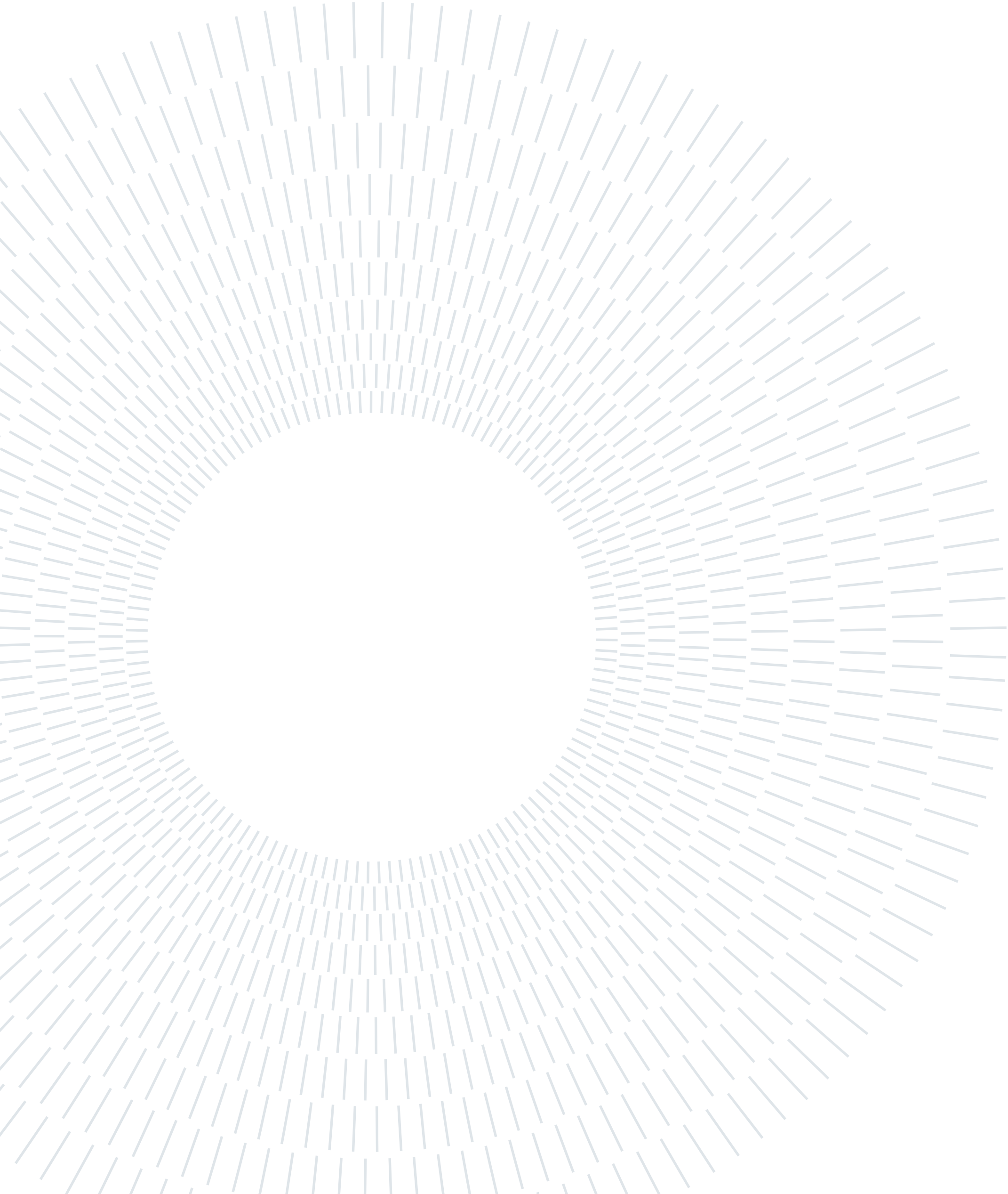

Credits

I would like to acknowledge my supervisor Prof. Colombo, whose ideas and insights guided me and helped to give this paper an original touch. Through this process, I have acquired a working method that I will certainly replicate in the future.

I wish also to send my gratitude to my correlator Dr. Alessi for promptly suggesting relevant material for development and precise and detailed corrections to the elaboration.

I extend my appreciation to all the researchers of the REMEC mission, for their hospitality and for the expertise I have developed in the project.

Finally, for their unwavering support, my heartfelt thanks go to my parents Alfredo and Caterina, and my siblings Alberto, Chiara, Delia, Eva and Sergio.